

DISSECTING THE SURFACE BRIGHTNESS OF GALAXIES

A DISSERTATION SUBMITTED TO THE GRADUATE DIVISION OF THE
UNIVERSITY OF HAWAII AT MĀNOA IN PARTIAL FULFILLMENT OF THE
REQUIREMENTS FOR THE DEGREE OF

DOCTOR OF PHILOSOPHY

IN

ASTRONOMY

August 2016

By

Po-Feng Wu (吳柏鋒)

Dissertation Committee:

R. Brent Tully, Chairperson
Rolf-Peter Kudritzki
Joshua E. Barnes
Roy R. Gal
John G. Learned

© Copyright 2016
by
Po-Feng Wu (吳柏鋒)
All Rights Reserved

Abstract

Mass and angular momentum are two fundamental quantities governing the evolution of galaxies. Nevertheless, because measuring the angular momentum of galaxies is difficult and requires significant resource, the effect of angular momentum on galaxy evolution remains poorly understood in observations. This dissertation research uses the surface brightness of galaxy disks as a proxy for the angular momentum and studies its effect on galaxy evolution. I have measured the surface brightness profiles from multi-wavelength photometry of 501 nearby late-type galaxies selected from the ALFALFA survey. With this homogeneous data set, I can investigate the surface brightness dependence on galaxy properties at fixed stellar mass. I have concluded that at fixed stellar mass, lower surface brightness galaxies contains more hydrogen gas, are less efficient in forming stars and consist of stars of lower abundance of heavy elements. However, the average ages of galaxies do not appear to depend on the surface brightness. Combining analytical chemical evolution models, I have constrained the gas inflow and outflow rates relative to the star-formation rate. At fixed mass, lower surface brightness galaxies experienced higher accretion rates. The surface brightness dependence is stronger in low mass galaxies. The model is not able to put meaningful constraints on the properties of gas outflow. Lastly, I have investigated the intriguing bimodal distribution of surface brightness found in the literature. I show that the bar-driven secular evolution redistributes the matter angular momentum, therefore, alters the surface brightness distribution.

Table of Contents

Abstract	iii
List of Tables	vi
List of Figures	vii
Chapter 1: Introduction	1
1.1 The Angular momentum of a disk galaxy	1
1.2 The surface brightness of galaxies	4
1.2.1 Definition of surface brightness	4
1.2.2 The surface brightness dependence on galaxy properties	6
1.2.3 The distribution of surface brightness	7
1.3 Overview of this dissertation	9
Chapter 2: The surface brightness dependence on physical properties	15
2.1 Introduction	15
2.2 Data	17
2.2.1 Sample Selection	17
2.2.2 Surface photometry	18
2.2.3 Deriving the central surface brightness	19
2.2.4 Stellar Mass, Gas Mass, and Star-formation Rate	20
2.3 Results	21
2.3.1 Galaxy properties as a function of surface brightness	21
2.3.2 Surface brightness dependence	23

2.4	Discussion	27
2.4.1	Colors	27
2.4.2	Star formation rates	30
2.4.3	Remarks on Surface Brightness	31
2.4.4	Conclusion	32
Chapter 3: The influence of surface brightness on the mass-metallicity relation . . .		37
3.1	Introduction	37
3.2	Data and Analysis	39
3.2.1	Samples	39
3.2.2	Photometry, surface brightness profile, and masses	41
3.3	The Surface Brightness Dependence on Metallicity	41
3.3.1	Gas-phase Metallicity from Spectroscopy	42
3.3.2	Stellar Metallicity from Broadband Colors	46
3.4	Theoretical Considerations	48
3.5	Discussion	53
3.5.1	Implications from the Mass and Surface Brightness Dependence on Λ	53
3.5.2	Possible Systematics	57
3.6	Summary	59
Chapter 4: Bimodal Surface Brightness Distribution of Galaxy Disks: Observational Evidence for Angular Momentum Transfer by Stellar Bars		68
4.1	Introduction	68
4.2	Data	71
4.2.1	The S4G sample	72
4.2.2	The WISE-ALFALFA sample	73
4.3	Result	76
4.3.1	The Distribution of Central Surface Brightness of Disks	76
4.3.2	The structural dependence on the surface brightness	78
4.4	Discussion	82

4.4.1	Bar formation transfers angular momentum	82
4.4.2	The Surface Brightness Distribution	84
4.5	Summary	87
Chapter 5:	Summary and future outlook	95
5.1	Dissertation Summary	95
5.1.1	The SB dependence on galaxy properties	96
5.1.2	The influence of surface brightness on the mass-metallicity relation .	96
5.1.3	The bimodal surface brightness distribution	97
5.2	Future Prospect	98
5.2.1	Complete the low surface brightness end of the distribution	98
5.2.2	SB dependence on galaxy properties from Spectroscopy	100
5.2.3	Constraining the gas flow properties of galaxies	101
Appendix:	Structural properties and photometry of the WISE galaxy sample	105

List of Tables

2.1	Spearman rank correlation coefficients	22
4.1	Structural Classification	72
A.1	Geometry of the WISE galaxy sample	106
A.2	Photometry of the WISE galaxy sample	127

List of Figures

1.1	Image and surface brightness profile of Malin 1	5
1.2	Bimodality of μ_0	9
2.1	Surface brightness dependence on galaxies properties	22
2.2	Stellar mass dependence on galaxies properties	23
2.3	Galaxy properties as a function of stellar mass, colored by SB	24
2.4	Surface brightness dependence on HI gas mass, optical color, NIR color . .	25
2.5	Surface brightness dependence on SFR	26
2.6	Model grids of stellar population synthesis models	28
3.1	Distributions of galaxy properties of the spectroscopic sample and the photometric sample	40
3.2	Metallicity as a function of stellar mass for the spectroscopic sample	43
3.3	The surface brightness dependence on the metallicity of the spectroscopic sample	44
3.4	The surface brightness dependence on the $z' - W1$ color of the photometric sample	47
3.5	An example of the model fit to the observed metallicity profile	51
3.6	Best-fit η and Λ as a function of mass and surface brightness.	61
3.7	Test of the systematical effect from the zero point of metallicity scale on model parameters	62

4.1	Comparison of surface brightness measured by different methods	74
4.2	Exponential disk fitting of galaxy NGC 4535	76
4.3	Physical properties of the S ⁴ G and the WISE-ALFALFA sample	77
4.4	The stellar mass and μ_0 distribution of the S ⁴ G sample, separated by galaxy structures	79
4.5	The μ_0 and h of the S ⁴ G sample as a function of stellar mass, separated by galaxy structures	80
4.6	The μ_0 and h of the S ⁴ G sample as a function of stellar mass, separated by bar length	89
4.7	Galaxies of different bar lengths	90

Chapter 1

Introduction

1.1 The Angular momentum of a disk galaxy

Disk galaxies show remarkable regularities. Observationally, disk galaxies follow scaling relations among their circular velocities, luminosities, and sizes. One of the most firmly established empirical scaling relations is the Tully-Fisher relation (Tully & Fisher 1977); a tight correlation between the total luminosity and the rotation speed of a disk galaxy, holding across many magnitudes in luminosity (Verheijen 2001; Masters et al. 2006; Pizagno et al. 2007). Also, there is a tight correlation between the luminosity and the size of the galaxy disk (Dalcanton et al. 1997; de Jong & Lacey 2000; Graham 2002; Shen et al. 2003; Courteau et al. 2007). These scaling relations suggest that galaxy evolution is well regulated, and the current properties of galaxies are tied to the primordial properties of dark halos and proto-galaxies, namely the mass and angular momentum. Understanding the effect of mass and angular momentum on galaxy evolution is fundamental in describing the evolution of the Universe.

Dark matter halos form from primordial density perturbations. High-density peaks collapse faster and form high mass halos. Baryonic matter in dark halos subsequently cools down, further collapses and forms galaxies. Apparently, the mass of the halos governs the evolution of galaxies. The effect of mass on galaxy evolution has been extensively studied observationally. Many galaxy properties are strongly correlated with the stellar and halo

mass, e.g., the average stellar age (Gallazzi et al. 2005, 2014), the metal content in the interstellar medium and the stars (ISM, Tremonti et al. 2004; Gallazzi et al. 2005; Savaglio et al. 2005; Lee et al. 2006), and the star-formation rate (Noeske et al. 2007; Daddi et al. 2007; Dutton et al. 2010; Sparre et al. 2015).

On the other hand, the halo acquires angular momentum during formation as a consequence of the tidal field of surrounding environment and merger events (Warren et al. 1992; Catelan & Theuns 1996a,b; Cole & Lacy 1996; Lemson & Kauffmann 1999; Steinmetz & Navarro 1999; Navarro & Steinmetz 2000). The angular momentum prevents baryons from collapsing isotropically but causes them to settle in a rotationally support disk. Thus, the angular momentum determines the disk size, the surface density, and likely the Hubble morphological type of the disk. Baryons in high angular momentum halos will distribute wider because of the stronger rotational support.

In practice, the spin parameter λ (Peebles 1969) is often used to quantify the angular momentum of a halo. The λ is defined as:

$$\lambda = \frac{J|E|^{1/2}}{GM^{5/2}}, \quad (1.1)$$

where G , J , E , and M are Newton's gravitational constant, the total angular momentum, total energy, and total mass of the halo, respectively (Mo et al. 1998). The parameter λ has been a crucial element for modeling important physical quantities of disk galaxies such as the disk size, star-formation rate, morphology, and rotational velocity (Dalcanton et al. 1997; Dutton et al. 2007; Dutton 2009).

Nevertheless, given the importance of the spin parameter from a theoretical aspect, there are only a handful of galaxies with well measured λ (Romanowsky & Fall 2012; Obreschkow & Glazerbrook 2014). Unlike the mass, it is much more difficult to measure the angular momentum. To measure the mass, it only requires the integrated light from either stars or gaseous component to calculate the baryon content. The total mass can be estimated from the circular velocity, assuming the galaxy is rotationally-supported. On

the contrary, measuring the angular momentum requires not only the integrated value, but also the spatially-resolve mass distribution and velocity profile. The expensive cost in observational resource makes it impractical to measure the λ for a large number of galaxies. Moreover, such measurement only accounts for the angular momentum of baryonic matter. The velocity of dark matter is not measurable thus the angular momentum. These difficulties hinder the comparison between theoretical predictions and observations.

To circumvent this fundamental difficulty, Hernandez & Cervantes-Sodi (2006) demonstrated that to first order, the spin parameter of disk galaxies can be approximated using the disk scale length of the stellar disk and the rotational velocity measured from the integrated spectrum. This approach reduces the observational resource required for studying the angular momentum content of galaxies, thus, can be applied to a large number of galaxies to with results from cosmological simulations (Cervantes-Sodi et al. 2008), even beyond the local universe (Cervantes-Sodi et al. 2012).

The most simple and easiest proxy is perhaps the surface brightness of galaxies. Assuming the baryon disk and the halo have the same specific angular momentum, galaxies in high angular momentum halos form extended, low surface brightness disks because of stronger rotational support. Although the surface brightness of the disk, in fact, depends not only on the angular momentum but also other factors such as the mass and the concentration of the halo (Dalcanton et al. 1997; Mo et al. 1998; Dutton et al. 2007), the anti-correlation between the angular momentum and the surface brightness generally holds. Because the surface brightness is a quantity that is easy to measure, it has been extensively used as a fundamental property of galaxies. I will review studies on the surface brightness of galaxy disks in the next section.

1.2 The surface brightness of galaxies

1.2.1 Definition of surface brightness

In the literature, the word "surface brightness" has various definitions. Although sharing the same name, these "surface brightness" can be very different from each other in quantity.

A commonly used quantity is the effective surface brightness, r_{eff} , the average surface brightness within the radius enclosing 50% of the galaxy light. Also, the surface brightness can be defined as the average surface brightness within an isophot measured at given surface brightness, for example, 25 mag arcsec⁻².

The surface brightness adopted in this study is the central surface brightness of the disk. The azimuthal-averaged light profile of galaxy disks can be parameterized by an exponential as a function of distance to the galaxy center:

$$\mu(r) = \mu_0 + 1.0857 \times \exp(r/h), \quad (1.2)$$

where h is the scale length, the distance that the surface brightness falls to $1/e$ of its maximum value and μ_0 is the central surface brightness of the disk, the value of the exponential at $r = 0$. We should note that the μ_0 does not represent the actual surface brightness of the galaxy at the center. Many galaxies consist of structural components other than an exponential disk, such as stellar bar or bulge, therefore, the surface brightness at galaxy center is different from μ_0 . The μ_0 is a characteristic value describing the property of the disk component of the galaxy. Practically, to derive the μ_0 and h of a disk, structural components at the inner part of the galaxy like the bar and the bulge are either modeled with other mathematical forms or are masked from the modeling.

The difference among different surface brightness measurements and the effect of galaxy structure is illustrated in Figure 1.1. Figure 1.1a is the image of Malin 1, a massive bulged-galaxy with faint and extended disk (Bothun et al. 1987). Figure 1.1b shows the azimuthally-averaged 1-D surface brightness profile of Malin 1. Arrows in Figure 1.1b indicates the

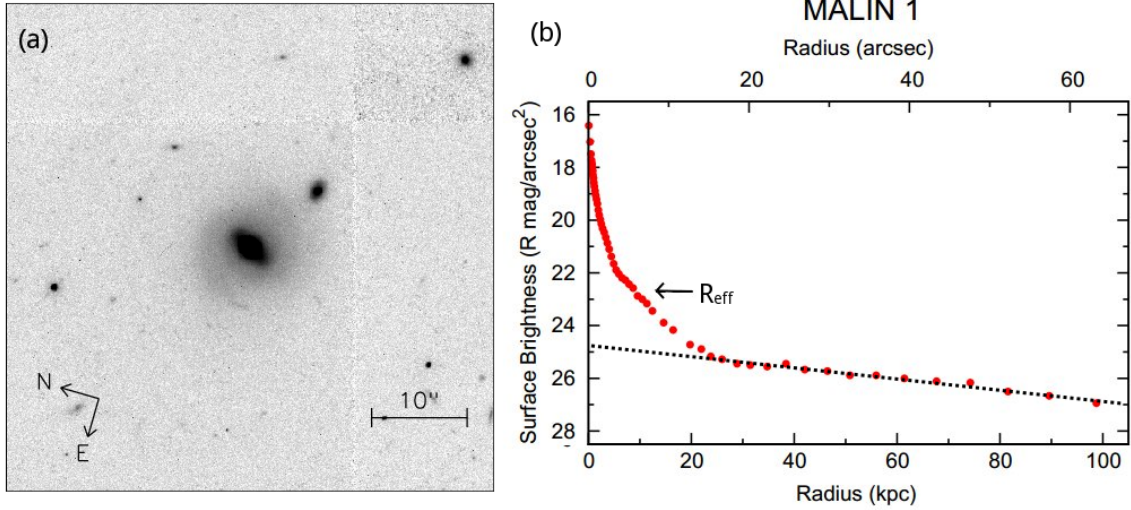


Figure 1.1 (a): *HST* WFPC2 F814W image of Malin 1 (Barth 2007). The faint disk of Malin 1 extends to at least 100 kpc ($\sim 70''$) from the galaxy center, but it is barely visible with this scaling. (b): R-band surface brightness profile of Malin 1 (Lelli et al. 2010). The effective radius (R_{eff}) is indicated by the arrow. The effective surface brightness (μ_{eff}), the average surface brightness within R_{eff} , is indicated by the horizontal dotted line. The slant dashed line represents the exponential disk fit and the central surface brightness of the disk (μ_0).

effective surface brightness. The dashed line represents the exponential fit to the disk and the central surface brightness (μ_0). The two measures differ $\sim 4 \text{ mag arcsec}^{-2}$ in surface brightnesses. For Malin 1, the effective surface brightness measures mostly the property of the bulge. Also, the surface brightness at the center of Malin 1 is not the same as the μ_0 , because the center of Malin 1 is dominated by the prominent bulge, but μ_0 only measures the disk component.

The principal focus of this study is the angular momentum content of galaxies and galaxy disk, therefore, I adopt μ_0 as the surface brightness measure as it represents the property of the disk better. Unless otherwise mentioned, the word "surface brightness (SB)" in this study refers to μ_0 .

1.2.2 The surface brightness dependence on galaxy properties

The majority of early explorations on the effect of surface brightness took a simple approach; defining a sample of galaxies with fainter than a value as low surface brightness (LSB) galaxies, then comparing their physical properties to "normal", or higher surface brightness (HSB) galaxies.

Early perception of LSB galaxies is that they are low mass, fairly blue systems with relatively high gas content and low metallicities (de Blok et al. 1995; McGaugh & de Blok 1997; Bell et al. 1999; Gerritsen & de Blok 1999; Galaz et al. 2002; Boissier et al. 2003). From these results, LSB galaxies are usually described as dormant galaxies which started forming stars later and in an inefficient manner so that they have a higher fraction of younger stars and exhibits bluer colors, low SFRs, and large gas reservoirs.

However, later observations show that LSB galaxies have remarkably diverse properties. (1) Very red LSB galaxies have been found in optical surveys (Burkholder et al. 2001). (2) LSB galaxies with near-solar abundance also exist (Bell & de Blok 2000). (3) In spite that LSB galaxies on average have higher gas abundance, extremely gas-poor LSB galaxies have been found (Burkholder et al. 2001). The spread in color, metallicity, and gas content show that they may actually have traveled along diverse evolutionary paths.

Part of these scatter in physical properties should be expected because the LSB galaxies in fact constitute a heterogeneous sample. An LSB galaxy can be a massive galaxy with extended distribution of stars, or a low mass galaxy so that it is faint. On the other hand, a compact, low mass galaxy may not be defined as an LSB galaxy. It is not clear which factor contributes more to the properties of LSB galaxies. In other words, we cannot tell whether mass and angular momentum is the main driver. It is necessary to decouple the effect of the angular momentum from the effect of mass.

However, we were confined by the relatively small number of LSB galaxies and their physical properties. Finding galaxies with low surface brightness is naturally difficult, not to mention the requirement to obtain extra information such as gas content or metallicity.

Our understanding toward the low surface brightness end of the distribution is limited by their faint nature.

But the game starts to change. Nowadays, large-scale surveys have released a prodigious amount of data in a broad wavelength range. Investigating physical properties of galaxies in a wide range of parameter space at the same time becomes possible. For example, the Sloan Digital Sky Survey (York et al. 2000) has provided optical images and structure parameters for more than a million galaxies (Simard et al. 2011). At other wavelengths, blind surveys such as the Galaxy Evolution Explorer (GALEX; Martin et al. 2003) and the Wide-Field Infrared Explorer (WISE; Wright et al. 2010) image the ultra-violet and near-IR sky. The Arecibo Legacy Fast ALFA Survey (ALFALFA; Haynes et al. 2011) measures HI gas content of galaxies. These data provide information on gas content, star-formation rate, stellar populations, and structures of stellar components. The synergy among these public surveys can potentially lead to a statical view of the effects of mass and angular momentum on galaxy formation and evolution.

1.2.3 The distribution of surface brightness

Obtaining the intrinsic distribution of the surface brightness of galaxies is difficult because the visibility of galaxies is biased by natural observing conditions. The night sky brightness limits our ability to find diffuse objects. Below a certain percentage of the night sky brightness, no galaxy would be seen. For a galaxy, only those part brighter than this threshold can be detected. Therefore, the observed galaxy population is altered from the true population by the night sky brightness (Impey & Bothun 1997).

Freeman (1970) made an early attempt at quantifying the surface brightness distribution of spiral galaxy disks. Freeman (1970) found that most disks have similar B -band surface brightness $\mu_{0,B} \simeq 21.65 \text{ mag arcsec}^{-2}$. This value was considered as a characteristic property of all galaxy disks. However, later observations with deeper images found a large number of galaxies with surface brightness much lower than the Freeman value (Davies

1990; Sprayberry 1994; O’Neil et al. 1999). The Freeman value is the only the property of the input galaxy catalog rather than the general galaxy population.

For a galaxy disk with surface brightness close to the night sky brightness, it appears much smaller and fainter because most part of the disk is blended with the night sky emission thus not seen (O’Neil et al. 2000). The galaxy appears smaller and fainter than its intrinsic properties. Therefore, a magnitude-limit or a size-limit sample selects against low SB galaxies, and this effect is a strong function of distance (see Tully 2015, for an example).

To better recover the intrinsic distribution of galaxy surface brightness, a volume-limited sample is essential to mitigate the incompleteness at the low surface brightness end. An intriguing distribution of surface brightness was revealed in the nearby Ursa Major complex ($D = 18 \text{ Mpc}$). Tully & Verheijen (1997) found a double-peaked distribution of surface brightness among 62 Ursa Major member galaxies. The mean surface brightness of the two peaks differ by $\sim 2 \text{ mag arcsec}^{-2}$ (Figure 1.2). The bimodal distribution is contradictory to the theoretical prescription, which predicts a single-peak distribution (Dalcanton et al. 1997).

The bimodality was later observed in the Virgo cluster. From a sample of 286 Virgo cluster galaxies, McDonald et al. (2009) also found a $\sim 2 \text{ mag arcsec}^{-2}$ difference between the two peaks of the distribution. Furthermore, the peak μ_0 magnitudes of the Virgo cluster are consistent with the peak magnitudes of the Ursa Major galaxies.

However, the work of Tully & Verheijen (1997) and McDonald et al. (2009) both include only a small portion of the sky and it is still questionable if the bimodality is a general property. Later, Sorce et al. (2013) analyzed μ_0 at $3.6\mu\text{m}$ for 438 galaxies with distances $D < 20 \text{ Mpc}$ selected from the Spitzer Survey of Stellar Structure in Galaxies (S⁴G; Sheth et al. 2010). This sample consists of galaxies from a large area of the sky ($|b| > 30 \text{ deg}$) and contains galaxies in both the field and clusters. Similar to what was found in the Ursa Major complex and the Virgo cluster, the bimodality of μ_0 is also presented in a sample

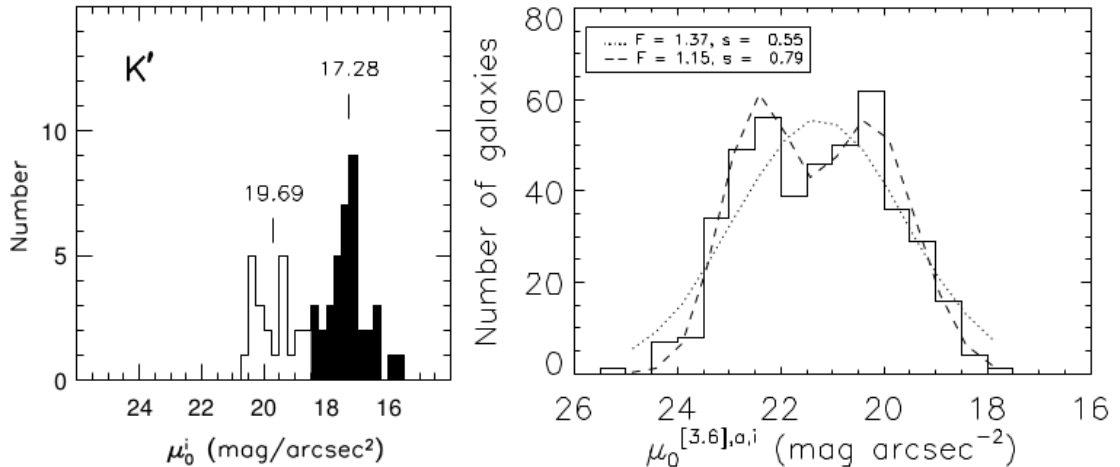


Figure 1.2 The surface brightness bimodality found in the literature. *Left:* The K' -band surface brightness distribution of 62 Ursa Major members, modified from Tully & Verheijen (1997). Galaxies appear to avoid the regime of surface brightness $\mu_{0,K'} \sim 18.5$. *Right:* The $3.6\mu\text{m}$ surface brightness distribution of 438 galaxies selected from the S⁴G survey, modified from Sorce et al. (2013). A deficit of galaxy at $\mu_{0,3.6} \sim 21.5$ is found. The distribution is better fit by two Gaussian profiles than one Gaussian profile.

dominated by field galaxies, suggesting that the bimodal distribution may be prevalent in all environments.

This peculiar bimodal distribution of μ_0 poses a challenge to current theories of galaxy formation. So far, no theoretical work has ever directly predicted such a distribution. On the observational side, some possible explanations have been briefly mentioned (Tully & Verheijen 1997; McDonald et al. 2009), but there is a lack of observational evidence to either support or reject these speculations. We will have to explain the bimodal surface brightness distribution before claiming that we understand galaxy formation and evolution.

1.3 Overview of this dissertation

This dissertation research is designed to investigate the effect of angular momentum on galaxy evolution, using surface brightness as a proxy. With the synergy of archival surveys, we are able to access multi-dimensional information for a large number of galaxies.

Therefore, we can have a more complete view from an ensemble of galaxies, on that suffers less from variations among individuals.

Using public data from several large surveys, I investigate the surface brightness dependence on galaxy properties in Chapter 2. With multi-wavelength data and a sufficiently large sample, I am able to isolate the effect of surface brightness from galaxy mass. In Chapter 3, I investigate the surface brightness dependence on the chemical abundance of galaxies. I use chemical evolution models to constrain the properties of the gas flow of galaxies and provide a theoretical explanation for the surface brightness dependence on the metallicity. In Chapter 4, I investigate the effect of internal structure formation in the disk on the surface brightness and provide an explanation for the intriguing bimodal surface brightness distribution of disks. Chapter 5 summarizes the major conclusions and outlines possible future directions of related work.

References

- Barth, A. J. 2007, AJ, 133, 1085
- Bell, E. F., Bower, R. g., de Jong, R. S., et al. 1999, MNRAS, 302, 55
- Bell, E. F., de Blok, W. J. G. 2000, MNRAS, 311, 668
- Bergmann, M. P., Jørgensen, I., Hill, G. J. 2003, AJ, 125, 116
- Boissier, S., Monnier Ragaigne, D., Prantzos, N., et al. 2003, MNRAS, 343, 653
- Bothun, G. D., Impey, C. D., Malin, D. F., Mould, J. R. 1987, AJ, 94, 23
- Bothun, G. D., Impey, C., McGaugh, S. 1997, PASP, 109, 745
- Burkholder, V., Impey, C., Sprayberry, D. 2001, AJ, 122, 2318
- Catelan, P., Theun, T. 1996a, MNRAS, 282, 436
- Catelan, P., Theun, T. 1996b, MNRAS, 282, 455
- Cervantes-Sodi, B., Hernandez, X., Park, C., Kim, J. 2008, MNRAS, 388, 863
- Cervantes-Sodi, B., Hernandez, X., Hwang, H. S., Park, C., & Le Borgn, D. 2012, MNRAS, 426, 1606
- Cole, S., Lacey, C. 1996, MNRAS, 281, 716
- Courteau, S., Dutton, A. A., van den Bosch, F. C., et al. 2007, ApJ, 671, 203

Daddi, E., Dickinson, M., Morrison, G., 2007, ApJ, 670, 156

Dalcanton, J. J., Spergel, D. N., & Summers, F. J. 1997, ApJ, 482, 659

Davies, J. I. 1990, MNRAS, 245, 350

de Blok, W. J. G., van der Hulst, J. M., Bothun, G. D. 1995, MNRAS, 274, 235

de Jong, R. S., Lacy, C. 2000, ApJ, 545, 781

Disney, M. J. 1976, Nature, 263, 573

Dutton, A. A. 2009, MNRAS, 396, 121

Dutton, A. A., van den Bosch, F. C., Dekel, A. 2010, MNRAS, 405, 1690

Dutton, A. A., van den Bosch, F. C., Dekel, A., & Courteau, S. 2007, ApJ, 654, 27

Freeman, K. C. 1970, ApJ, 161, 802

Galaz, G., Dalcanton, J. J., Infante, L., & Treister, E. 2002, AJ, 124, 1360

Gallazzi, A., Bell, E. F., Zibetti, S., et al. 2014, ApJ, 788, 72

Gallazzi, A., Charlot, S., Brinchmann, J., While, S. D. M., Tremonti, C. A. 2005, MNRAS, 362, 41

Gerritsen, J. P. E., deBlok, W. J. G. 1999, A&A, 342, 655

Graham, A. W. 2002, MNRAS, 334, 721

Haynes, M. P., Giovanelli, R., Martin, A., et al. 2011, AJ, 142, 170

Hernandez, X. & Cervantes-Sodi, B. 2006, MNRAS, 368, 351

Impey, C., Bothun, G. 1997, ARA&A, 35, 267

Lee, H., Skillman, E. D., Cannon, J. M., et al. 2006, ApJ, 647, 970

Lelli, F., Fraternali, F., Sancisi, R. 2010, A&A, 516, 11

Lemson, G., Kauffmann, G. 1999, MNRAS, 302, 111

Masters, K. L., Spingob, C. M., Haynes, M. P., Giovanelli, R. 2006, ApJ, 653, 861

McDonald, M., Courteau, S., & Tully, R. B. 2009, MNRAS, 394, 2022

McGaugh, S. S., & de Blok, W. J. G. 1997, ApJ, 481, 689

Martin, C., Barlow, T., Barnhart, W., et al. 2003, SPIE, 4854, 336

Mo, H. J., Mao, S., & White, S. D. M. 1998, MNRAS, 319, 336

Navarro, J. F., Steinmetz, M. 2000, ApJ, 538, 477

Noeske, K. G., Weiner, B. J., Faber, S. M. 2007, ApJ, 660, 43

Obreschkow, D. & Glazerbrook, K. 2014, ApJ, 784, 26

O’Neil, K., bothun, G. D., Impey, C. D. 1999, AJ, 118, 1618

O’Neil, K., Bothun, G. D., Schombert, J. 2000, AJ, 119, 136

Peebles, P. J. E. 1969, ApJ, 155, 393

Pizagno, J., Prada, F. Weinberg, D. H., et al. 2007, AJ, 134, 945

Romanowsky, A. J., & Fall, S. M. 2012, ApJS, 203, 17

Salpeter, E. E., Hoffman, G. L. 1996, ApJ, 465, 595

Savaglio, S., Glazebrook, K., Le Borgne, D., et al. 2005, ApJ, 635, 260

Shen, S., Mo, H. J., White, S. D. M., et al. 2003, MNRAS, 343, 978

Sheth, K., Regan, M., Hinz, J. L., et al. 2010, PASP, 122, 1397

Simard, L., Mendel, J., Trevor, P., et al. 2011, ApJS, 196, 11

Sorce, J. G., Coutois, H. M., Sheth, K., Tully, R. B. 2013, MNRAS, 433, 751

Sparre, M., Hayward, C. C., Springel, V., et al. 2015, MNRAS, 447, 3548

Sprayberry, D. 1994, PhDT

Steinmetz, M., Navarro, J. F. 1999, ApJ, 513, 555

Tremonti, C. A., Heckman, T. M., Kauffmann, G., et al. 2004, ApJ, 613, 898

Tully, R. B. 2015, AJ, 149, 171

Tully, R. B., Fisher, J. R. 1977, A&A, 54, 661

Tully, R. B., Verheijen, M. A. W. 1997, ApJ, 484, 145

Verheijen, M. A. W. 2001, ApJ, 563, 694

Warren, M. S., Quinn, P. J., Salmon, J. K., Zurek, W. H. 1992, ApJ, 399, 405

Wright, E., Eisenhardt, P. R. M., Mainzer, A. K. et al. 2010, AJ, 140, 1868

York, D. G., Adelman, J. Anderson, J. E. Jr., et al. 2000, AJ, 120, 1579

Chapter 2

The surface brightness dependence on physical properties

2.1 Introduction

In the current cosmological paradigm, cosmic structures grow hierarchically. Matter associated with peaks in the primordial density field gravitationally collapses and forms dark matter halos. Baryons cool and condense near the centers of the halos and form galaxies (White & Rees 1978; White & Frenk 1991). Theoretical and numerical calculations suggest dark matter halos should form with a wide range of mass and angular momenta. Galaxies forming in these halos, therefore, distribute across a wide range of mass and surface brightness (hereafter, SB). Baryons in high-mass or low-spin halos collapse to form high SB galaxies, while baryons in low-mass or high-spin halos cannot collapse all the way due to stronger rotational support and form lower SB galaxies (Dalcanton et al. 1997; Mo et al. 1998; Dutton et al. 2007). A clear picture of galaxy formation and evolution requires the exploration of the full range of galaxy characteristics in both mass and the SB to obtain an unbiased view.

Observational work is biased against the low luminosity and the low surface brightness end of the distribution due to their faint nature. Especially for galaxies with low SB, the outskirts of low SB galaxies are embedded in the night sky background, thus cannot be detected. Therefore, low SB galaxies look smaller and are visible out to a smaller

distance than galaxies with the same luminosity but higher surface brightness (Disney 1976; Bothun et al. 1997). Knowing this intrinsic observational bias, a series of efforts has been devoted to constructing samples of low surface brightness (LSB) galaxies for further detailed investigation (Schombert et al. 1992; Impey et al. 1996; O’Neil et al. 2000).

Numerous studies have characterized the physical properties of galaxies at the faint end of the SB distribution. First, the star-formation rate (SFR), derived from either UV or H α emission, of LSB galaxies is low (Schombert et al. 2001). Second, LSB galaxies have bluer optical and NIR colors (Galaz et al. 2002; Schombert & McGaugh 2014), although larger scatter in optical colors are also identified (Boissier et al. 2003). Third, LSB galaxies on average have higher ratios of gas to stellar masses (McGaugh & de Blok 1997). The last, LSB galaxies contain less heavy elements in both their interstellar medium (ISM) and their stellar components (Ellison et al. 2009; Wu et al. 2015).

Given these general properties, LSB galaxies are actually heterogeneous. The LSB class contains galaxies from a wide range of size, luminosity, and morphology from dwarf irregulars to giant disk galaxies. A galaxy can be classified as LSB because of either low stellar mass content or extended matter distribution. Although LSB galaxies share similar physical properties, it is difficult to link these properties back to fundamental physical parameters: the mass and the angular momentum. Simply from the observed properties of LSB galaxies, we do not know which factor is the main driver. It is already well known that the properties of galaxies are strongly correlated with stellar mass, where low mass galaxies are generally bluer, with lower SFR, more gas-rich, and metal-poor (Tremonti et al. 2004; Gallazzi et al. 2005; Noeske et al. 2007; Huang et al. 2012). Therefore, at least part of the physical properties of LSB galaxies can be attributed to their less massive nature. Whether and how much the compactness, or the angular momentum, affects galaxy evolution still remains obscured.

To understand how galaxy evolution is controlled by mass and the angular momentum, it is necessary to separate the mass dependence from the SB dependence. However, there have been only limited efforts in doing so (e.g., Ellison et al. 2009). The main purpose of

this study is to establish the baseline measurements of galaxy properties as a function of both the SB and stellar mass. We will use multi-wavelength data from public large surveys to derive the galaxy colors, SFR, and gas content of galaxies across a wide range of SB and stellar mass. We will compare galaxies with different SBs at fixed mass, in order to isolate the dependence of mass from that of the SB. We describe the sample selection and derivation of galaxy properties in Section 2. The SB dependence is presented in Section 3. Section 4 contains the discussion of the implications of the SB dependence seen from our results.

2.2 Data

2.2.1 Sample Selection

One of the goals of this study is to investigate the SB dependence on the physical properties of galaxies down to a low SB regime poorly sampled by previous studies. To properly sample the low SB regime, we do not use optically-identified catalogs because they are intrinsically biased towards high mass, high SB galaxies (Bothun et al. 1997; Dalcanton et al. 1997). Instead, we select our galaxy sample from the H I sources detected by the Arecibo Legacy Fast ALFA Survey (ALFALFA; Haynes et al. 2011), then measure their structural parameters using images from the Wide-Field Infrared Explorer (WISE; Wright et al. 2010). By using an H I-based mother sample, we mitigate the bias against low SB galaxies. We note that this sample is biased against gas poor, red low SB galaxies, which are intrinsically difficult to be detected in both optical wavelength and H I 21 cm.

All our galaxy have H I flux from the ALFALFA survey, therefore, we can derive their atomic gas content. Combined with the stellar mass and the star-formation rate (SFR, see Section 2.2.4), we can discuss the star-formation properties. Moreover, the ALFALFA field overlaps with the SDSS field. The multi-wavelength broadband photometry will give further hints regarding the ages and metallicities of galaxies.

From the ALFALFA survey, we select sources with heliocentric velocities $V_{hel} \leq 3000$ km s⁻¹. The velocity, or equivalently, rough distance limit is chosen as a compromise between sample size and completeness. At larger distances, only H I massive galaxies will be detected by ALFALFA. Also, the angular resolution of the WISE images prevents us from measuring the structure parameters of stellar disks for fainter or less extended galaxies, thus causing potential bias. Including galaxies at large distances will not obtain more galaxies at the low SB regime, which is our interest.

We select galaxies with $m_{W1} \leq 16$, $b \geq 0.8'$, and axis ratios $b/a \geq 0.35$. The m_{W1} is the apparent magnitude measured in the WISE W1 3.4 μ m band. The a and b are the major and minor axes measured at $\mu_{W1} = 25$ mag arcsec⁻². We consider measurements from galaxies fainter or smaller than these limits to be not reliable. The limit on the axis ratio removes edge-on galaxies, where correction of the geometric effect of the inclination is less certain. We will describe how we measure the magnitude and surface brightness in the following sections. In total, we select 501 galaxies from the ALFALFA survey.

2.2.2 Surface photometry

For this study, we perform surface photometry on the SDSS u' , g' , r' , i' , z' , WISE W1 3.4 μ m, W2 4.5 μ m, W3 12 μ m, W4 22 μ m, and GALEX FUV and NUV images of each galaxy, using elliptical apertures with fixed centers, orientations and shapes with varying major axes in step of 3". Our structure parameters are measured from the W1 images, which has a spatial resolution of $\sim 6''$, thus justifying the 3" step to sample the radial profiles of galaxies.

We determine ellipses for surface photometry from W1 images as following. We use the shape from the RC3, or SDSS r' -band when needed, to measure the sky level for the first pass. We then fit an ellipse to the isophot at 25 mag arcsec⁻² of the sky-subtracted image. If the shape and the orientation of the output ellipses are consistent with those of input ellipses, we use these parameters as our input for surface photometry. If the shapes of input and output ellipses are inconsistent (Δ P.A. > 20 deg or $\Delta b/a > 0.2$), we choose the better one based on visual inspection. The chosen orientation and shape are then applied for surface

photometry at all bands. We correct the Galactic extinction based on the extinction map of Schombert et al. (2001) and estimate the internal extinction following the prescription of Tully et al. (1998) based on the HI line width and the inclination of galaxies, where we have the information for all galaxies. Throughout this paper, we convert extinction among different filters using the conversion factors provided by Yuan et al. (2013).

For GALEX bands, we adopt a different prescription for internal extinction because the Tully et al. (1998) calibration does not cover UV wavelengths. Instead, we estimate the internal extinction from the observed UV colors of galaxies. We follow the calibration of Hao et al. (2011):

$$A_{FUV} = 3.83 \times [(FUV - NUV)_{obs} - 0.022], \quad (2.1)$$

We will use GALEX UV band to derive the SFR (Section 2.2.4). Some galaxies do not have both FUV and NUV measurements. We will exclude them from the sample when we discuss the SFR.

2.2.3 Deriving the central surface brightness

We measure the SB from the $3.4\mu\text{m}$ W1 band in this study. The $3.4\mu\text{m}$ W1 band is nearly free from concern for internal extinction. We fit the annuli-averaged surface brightness profile in W1 using a form of

$$\mu(r) = \mu_0 + 1.0857 \times \exp(r/h), \quad (2.2)$$

where μ_0 is the central surface brightness of the disk and h is the scale length. To exclude the effect of the bulge, we adopt a fiducial fitting range between effective radius, r_e , and the radius of isophot of $25.5 \text{ mag arcsec}^{-2}$, $r_{25.5}$. In some cases, the surface brightness at r_e is still affected by the bulge or bar. We then manually adjust the inner fitting range to avoid the effect of structures in the inner part of the galaxy. Adjusting the fitting range affects the result. To access the effect from the fitting range, we perform the same fitting procedure,

but change the inner limit from r_e to $0.9r_e$ and $1.1r_e$. We find that, as long as the bulge is not included in the fit, for most galaxies, the uncertainty in SBs is $< 0.3 \text{ mag arcsec}^{-2}$.

The central surface brightness is then corrected for the geometric effect of the inclination as follow (Tully et al. 1996):

$$\mu_{0,i} = \mu_0 - 2.5 \log(b/a), \quad (2.3)$$

where a and b are the major and minor axis of the galaxy, respectively. The inclination-corrected central surface brightness, $\mu_{0,i}$, is the SB we use in this study.

2.2.4 Stellar Mass, Gas Mass, and Star-formation Rate

For stellar masses, we adopt the color-dependent stellar mass-to-light ratio from $W1$ and $W2$ magnitudes (Cluver et al. 2014):

$$\log \Upsilon = -1.93(W1_{Vega} - W2_{Vega}) - 0.04, \quad (2.4)$$

where $W1_{Vega} = W1_{AB} - 2.699$, $W2_{Vega} = W2_{AB} - 3.339$, and Υ is the mass-to-light ratio at $W1$ band. Υ is calculated for every annulus until the largest annulus with reliable $W2$ photometry and then fixed for larger radius. Our sample galaxies have typical mass-to-light ratio $\Upsilon = 0.57$ in the $W1$ band.

The H I mass is calculated as $M_{HI} = 2.356 \times 10^5 \times D^2 \times F$, where D is distance in Mpc and F is H I flux from the ALFALFA survey in Jy. We adopt $M_{atom} = 1.4 \times M_{HI}$ to include the contribution from helium and metals.

The SFR is derived from the extinction-corrected FUV luminosities. Besides FUV luminosity, the WISE W3 and W4 bands can also be used to estimate the SFR. The W3 $12\mu\text{m}$ covers the $11.3\mu\text{m}$ Polycyclic Aromatic Hydrocarbon (PAH) emission associated with star-forming regions and the W4 $22\mu\text{m}$ traces the thermal emission warm dust heated by new-born stars. However, the W3 and W4 bands are much shallower than the GALEX FUV band. Only 47% (22%) of our sample is detected in W3 (W4), and they are exclusively high mass, high SB galaxies. On the other hand, 88% of the sample is detected in both NUV

and FUV. Therefore, we adopt only the GALEX FUV flux as the star-formation indicators in the study. We convert the extinction-corrected FUV luminosity to SFR according to Kennicutt (1998):

$$SFR(M_{\odot} \text{ yr}^{-1}) = 1.4 \times 10^{-28} L_v \text{ (erg s}^{-1}\text{Hz}^{-1}) \quad (2.5)$$

For distances, we use the Extragalactic Distance Database¹ (EDD; Tully et al. 2009) as the main source. We adopt the group distance, D_{gp} , in the ‘‘Cosmicflows-2 Distances’’ section of EDD as our primary distance. For distances not available in EDD, we take distances from the ALFALFA survey and converted to $H_0 = 75 \text{ km s}^{-1}\text{Mpc}^{-1}$ in order to be consistent with EDD distances.

2.3 Results

2.3.1 Galaxy properties as a function of surface brightness

Figure 2.1 shows galaxy properties as a function of SB. Figure 2.1(a) and Figure 2.1(b) plot baryon components, the stellar mass and HI mass. Figure 2.1(c) and Figure 2.1(d) show the optical and the NIR colors. Figure 2.1(e) and Figure 2.1(f) plot the WISE W3 $12\mu\text{m}$ and the extinction-corrected GALEX FUV magnitudes, two tracers for star-formation rates.

The SBs of galaxies show weak to medium correlations with all physical properties examined. In general, galaxies with higher SBs are more massive, redder in both optical and NIR colors, and have more active star-formation activities. These statements appear to be in broad agreement with the majority of previous studies.

Nevertheless, the gas mass, the color, and the star-formation rate are all known to have strong dependences on stellar mass; higher mass galaxies are redder, on average contain more gas and have higher SFR (Huang et al. 2012; Noeske et al. 2007). Figure 2.2 plots the galaxy properties as a function of M_{\star} . Figure 2.1 and Figure 2.2 together show that the overall M_{\star} and μ_0 dependence on galaxy properties are similar. This is expected from the positive correlation between M_{\star} and μ_0 (Figure 2.1a).

¹<http://edd.ifa.hawaii.edu/>

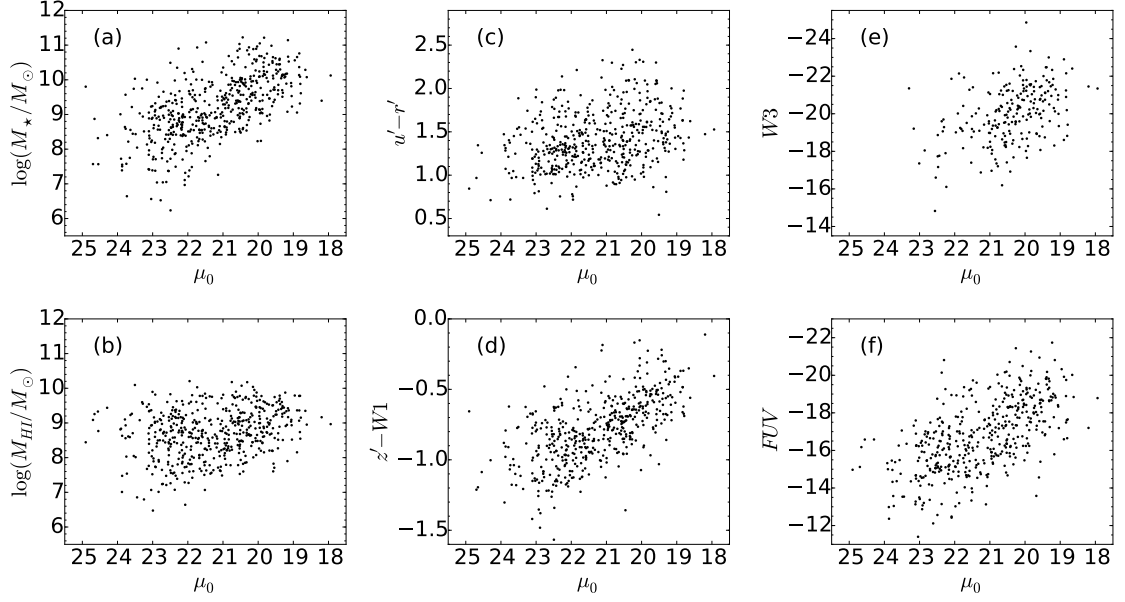


Figure 2.1 Galaxies properties as a function of surface brightness. (a): stellar mass, (b): HI gas mass, (c): $u' - r'$ color, (d): $z' - W1$ color, (e): absolute W3 magnitude, and (f): absolute FUV magnitude.

Table 2.1 Spearman rank correlation coefficients

	M_{HI}	$u' - r'$	$z' - W1$	W3	FUV
μ_0	-0.26	-0.30	-0.64	0.67	0.61
M_\star	0.54	0.43	0.67	-0.86	-0.85

$(\mu_0, M_s) = -0.62$

Visually inspection on Figure 2.1 and Figure 2.2 finds that the physical properties in general exhibit tighter correlations with M_\star than with μ_0 . Table 2.1 lists the Spearman correlation rank coefficients between M_\star , μ_0 , and other galaxy properties. The Spearman rank correlation coefficients suggest the same conclusion that M_\star better correlates with all galaxy properties. These simple observations suggest that the dependence on the SB is mainly driven by the dependence on the stellar mass. The SB has a relatively minor effect, if any. Therefore, in order to access the effect from the SB, it is necessary to take away the effect of stellar mass. In the next section, we will investigate the effect of SB by comparing galaxies properties at fixed stellar mass.

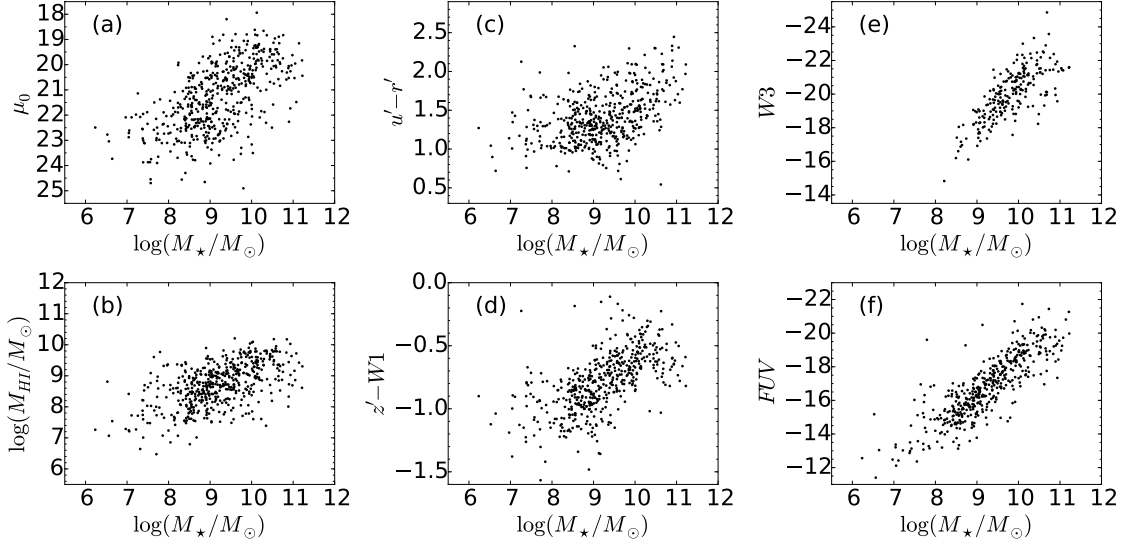


Figure 2.2 Galaxies properties as a function of stellar mass. (a): stellar mass, (b): H I gas mass, (c): $u' - r'$ color, (d): $z' - W1$ color, (e): absolute W3 magnitude, and (f): absolute FUV magnitude.

2.3.2 Surface brightness dependence

Figure 2.3 plots the galaxy properties as a function of stellar mass, with galaxies colored by their SBs. Instead of plotting the FUV magnitudes, we convert it to the SFR. Figure 2.3 also plot the specific SFR (SSFR), the SFR divided by stellar mass and the star-formation efficiency (SFE), the SFR divided by gas mass. If the SB has strong effects on galaxy properties at fixed mass, data points of different colors should separate from each other in the vertical direction. On the contrary, we find in Figure 2.3 that at fixed stellar mass, galaxies of given SB spread widely in the vertical axis and overlap with galaxies of different SBs.

To better examine the SB dependence, we calculate the median properties of galaxies in each 0.5 dex stellar mass bin and each 1 mag arcsec⁻² bin. Figure 2.4 shows the median gas mass and colors and their uncertainties calculated from the bootstrap resampling. We show data points calculated from at least 15 galaxies in a stellar-mass-SB bin to avoid large bias from outliers. The SB range discussed here is mainly $23 > \mu_{0,[3.4]} > 19$, which corresponds

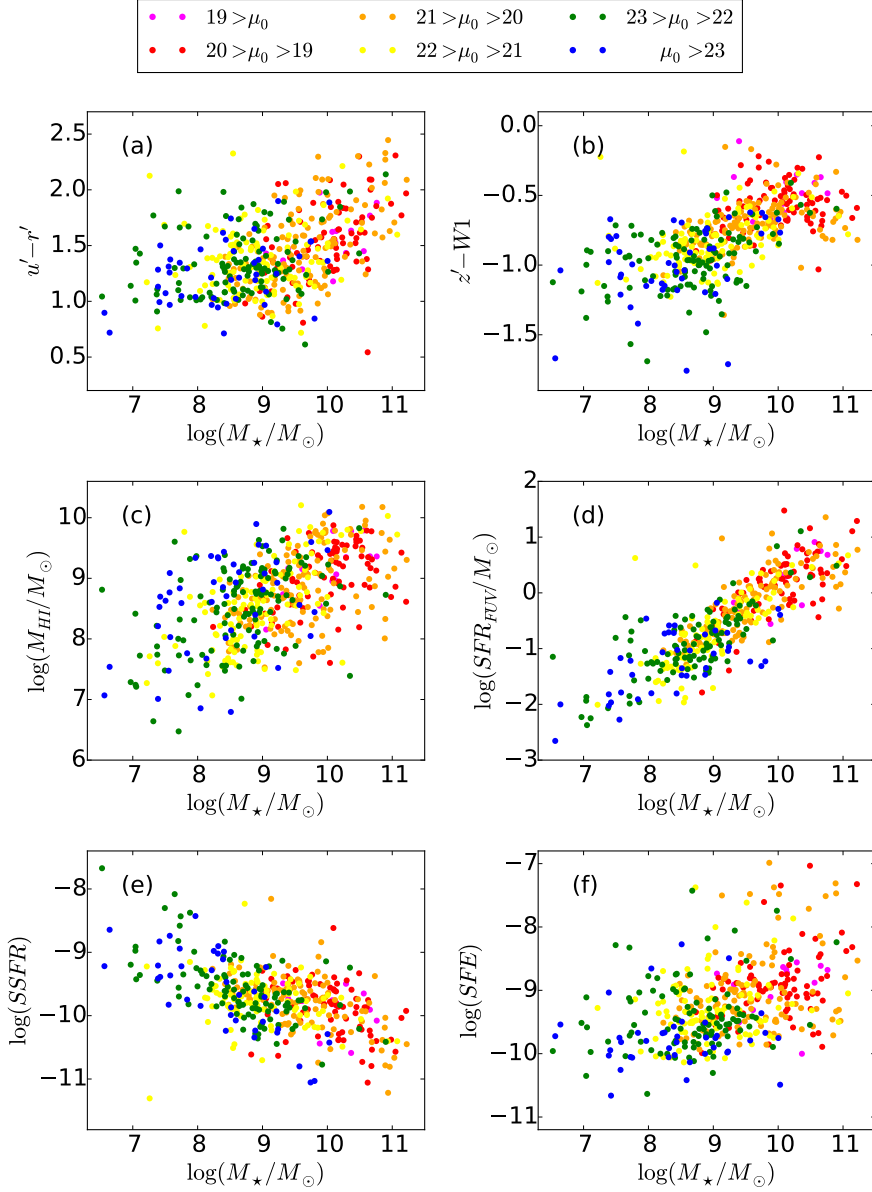


Figure 2.3 Galaxy properties as a function of stellar mass. (a) $u' - r'$ color, (b) $z' - W1$ color, (c) H I gas mass, (d) SFR, (e) SSFR, and (f) SFE. Each galaxy is colored by the surface brightness. Between $23 < \mu_0 < 19$, galaxies in the same 1 mag arcsec $^{-2}$ bin are represented by the same color (green, yellow, orange, and red). Galaxies with $\mu_0 > 23$ or $\mu_0 < 19$ are plotted in blue and magenta, respectively.

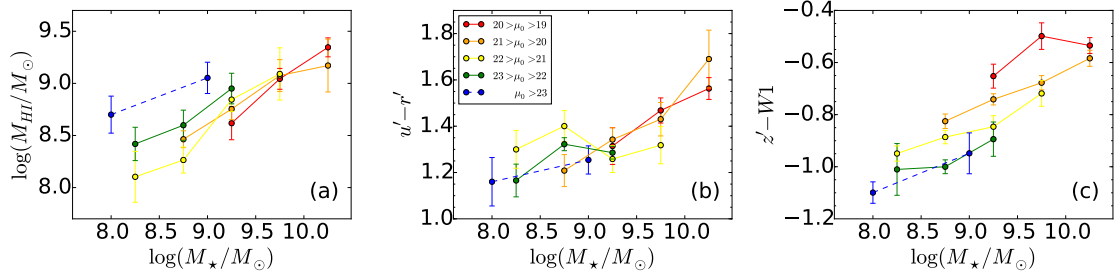


Figure 2.4 The median galaxy properties as a function of stellar mass. (a) H I gas mass, (b) $u' - r'$ color, (c) $z' - W1$ color. We group galaxies in 0.5 dex stellar mass and 1 mag arcsec⁻² SB bins and calculate the median and errors from bootstrap resampling. We only show data derived from at least 15 galaxies in each M_* -SB bin to avoid large bias from outliers. For galaxies with $\mu_0 > 23$, we use a larger 1 dex stellar mass bin and plot them using dashed lines. Colors represent the SBs. Red represents the highest SB bin and blue the lowest.

to $30 M_\odot \text{ pc}^{-2} \lesssim \mu_0 \lesssim 1,200 M_\odot \text{ pc}^{-2}$. We also plot galaxies with $\mu_{0,[3.4]} > 23$, the low SB regime which is poorly covered by previous studies. However, there are fewer galaxies with such low SBs in our sample. Therefore, we use a larger 1 dex stellar mass bin for these low SB galaxies and plot them with dashed lines to distinguish it from other subsamples.

We see in Figure 2.4a that there is a correlation between the SB and the gas mass. At fixed stellar mass, low SB galaxies are systematically more gas-rich. However, at the high-mass end, the SB dependence weakens. Figure 2.4b and Figure 2.4c show the optical and the NIR colors. For the $u' - r'$ color, there is only at most a slight SB dependence. The correlation between the SB and the $u' - r'$ color mainly reflects that high mass galaxies are redder, and they also have high SB. On the contrary, the $z' - W1$ color is driven by both the stellar mass and the SB. At fixed stellar mass, the $z' - W1$ color increases ~ 0.08 when the SB increases 1 mag arcsec⁻² between $23 > \mu_0 > 19$. We will discuss the implication of the SB dependence on colors in Section 4.

Next, we examine the SB dependence on the SFR. Figure 2.5 plots the SFR as a function of stellar mass, separate by the SB. We see in Figure 2.1f and Figure 2.2f that the FUV magnitude strongly correlates with the SB and the stellar mass. Figure 2.5a shows that the

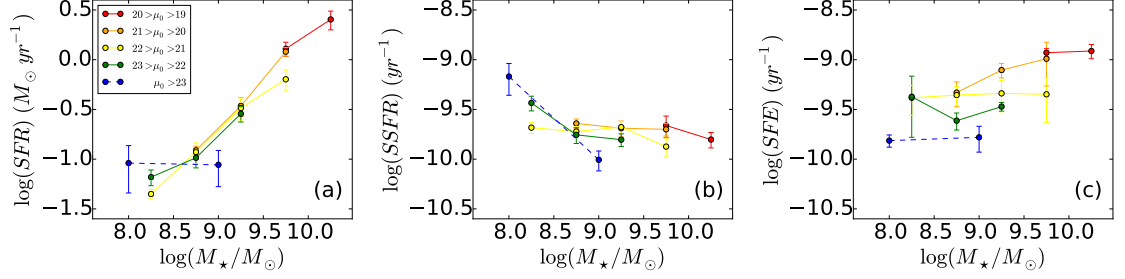


Figure 2.5 The median SFR as a function of stellar mass. (a) SFR, (b) SSFR, and (c) SFE. The median and the uncertainty are calculated as describe in Figure 2.4. The SFR are derived from FUV luminosities. The SFR and SSFR of galaxies do not depend on the SB, but the SFE does.

correlation is mainly driven by the stellar mass but not the SB. At fixed stellar mass, the SB dependence is nearly negligible comparing to the stellar mass dependence.

Figure 2.5b plots the specific SFR (SSFR), the SFR divided by the stellar mass, as a function of stellar mass. This is similar to Figure 2.5a, but the SB dependence is better presented after being normalized by the stellar mass. At fixed stellar mass, the SFR changes by $\lesssim 0.1$ dex level while the SB changes by $2 \text{ mags arcsec}^{-2}$. There is a tentative inverse of the SB dependence at $\log(M_*/M_\odot) < 8.5$, where low SB galaxies have higher SFR at fixed stellar mass. However, we do not have a reliable measurement at this lowest mass, low SFR bin. We see in Figure 2.1 that only sources with $M_{FUV} \lesssim -14$ are detected. At $\mu_0 > 23$, only the brightest population will have SFR measurements, therefore, the median SFR for the lower SB bins are likely over-estimated due to incompleteness at lower SFR.

We show the SFE in Figure 2.5c. First, the SFE is stellar-mass-dependent. High-mass galaxies on average have higher SFE. This is consistent with previous results from galaxies with $\log(M_*/M_\odot) \gtrsim 9$ (Boselli et al. 2014). Besides the stellar mass dependence, the SFE shows a strong SB dependence. High SB galaxies have higher SFE at fixed stellar mass. We will discuss the implication on the star-formation history in Section 4.

2.4 Discussion

In Section 3, we have examined the influence of SB on several physical properties of galaxies. We have decoupled the dependence between the stellar mass and the SB and are able to investigate the effect of each parameter separately. We interpret the result in this section.

2.4.1 Colors

In this study, we present the SB dependence on the optical $u' - r'$ and the NIR $z' - W1$ colors. Combining the broad band optical and NIR colors provides a proxy for investigating the stellar ages and metallicities of a large sample of galaxies. Figure 2.6 is the color-color diagram of stellar population synthesis model grids from Conroy et al. (2009) and Conroy & Gunn (2010). We connect models with the same star-formation histories by solid lines and models with the same stellar metallicities by dashed lines. The $u' - r'$ color is sensitive to star-formation histories and relatively insensitive to stellar metallicity. The $z' - W1$ color, on the other hand, is nearly independent of the star-formation history for galaxies with optical color $u' - r' \gtrsim 1.0$.

The underlying physics is that the optical colors at shorter wavelength probe the main sequence turn-off, which is age-sensitive. On the other hand, for galaxies with intermediate-age stellar populations, the NIR flux is dominated by the red giant branch (RGB) and the thermal pulsing asymptotic giant branch (TP-AGB) stars, whose colors are metallicity-sensitive. We see in Figure 2.4 that most of our data points have $u' - r' \gtrsim 1.0$. The $z' - W1$ color is qualitatively a good proxy for the stellar metallicities in our case.

NIR color

The strong influence of the stellar mass and the SB on the $z' - W1$ color can be interpreted in terms of the stellar mass and the SB dependences on the stellar metallicity. The stellar mass dependence had been reported in previous spectroscopic studies (Gallazzi et al. 2005; Panter et al. 2008; González Delgado et al. 2014).

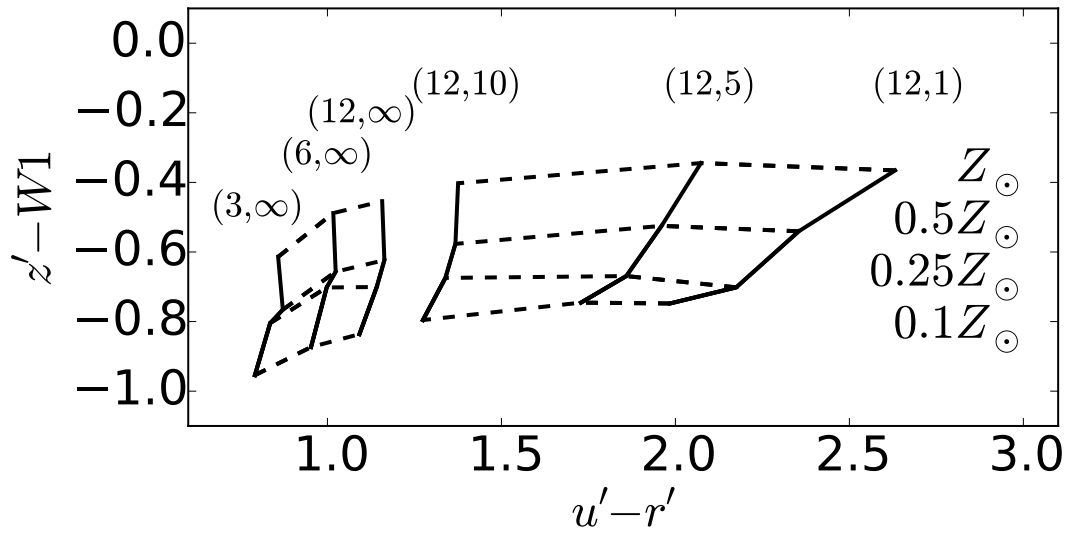


Figure 2.6 Grids of stellar population synthesis models FSPS (Conroy et al. 2009; Conroy & Gunn 2010) for different star formation histories and metallicities. The numbers in the parenthesis (t_f, τ) represent for the decay time scale of exponential SFH and the time when star formation started. $\tau = \text{inf}$ indicates constant star formation rate. The model shows that the $z' - W1$ color is sensitive to metallicity but insensitive to age except for the youngest galaxies. The $u' - r'$ color is on the other hand sensitive to stellar ages but insensitive to metallicity.

The SB dependence on stellar metallicity is expected from the SB dependence on the gas-phase metallicity. Ellison et al. (2009) showed that high SB galaxies on average have higher gas-phase metallicity at fixed stellar mass. Because stars form out of the ISM, to first order, we expect that the stellar metallicity should follow the same dependence as that of gas-phase metallicity.

Although the positive SB dependence is an expectation, the strength of the effect is remarkable. At fixed stellar mass, we find that the $z' - W1$ changes ~ 0.2 mag across the SB range we probe (2–3 mags arcsec⁻²), which roughly corresponds to a ~ 0.5 dex change in metallicity according to the models (see Figure 2.6).

Gallazzi et al. (2005) have shown that there is a significant scatter between the stellar mass and the metallicity, especially for lower mass galaxies. The scatter at fixed mass at $\log(M_*/M_\odot) < 10$ is about 0.5 dex. We note that our study and the one of Gallazzi et al. (2005) use galaxy samples based on different selection criteria, so it is not proper to compare the numbers directly. In addition, metallicity inferred from broadband colors is model-dependent (Conroy & Gunn 2010). Here we simply demonstrate that qualitatively, the SB can potentially account for a significant part of the scatter in the stellar mass-metallicity relation. The surface density may play an important role in the chemical evolution of galaxies.

Optical color

Some early studies reported that low SB galaxies have on average bluer optical colors (de Blok et al. 1995; Gerristen & de Blok 1999; Burkholder et al. 2001; Zhong et al. 2008), but red low SB galaxies also exist (O’Neil et al. 2000; Boissier et al. 2003). The blue optical color is often interpreted as young and metal-poor stellar population. Boissier et al. (2003) further argued that low SB galaxies should have sporadic star-formation histories in order to explain the existence of red low SB galaxies. In this view, red low SB galaxies are those galaxies between two active star-formation periods.

We have seen in Figure 2.4 that unlike the NIR color, the optical $u' - r'$ color does not show a strong SB dependence. The positive correlation between the SB and $u' - r'$ color is mainly driven by the stellar mass. Although there is a tentative SB dependence that high SB galaxies are redder, at fixed stellar mass, the SB affects the $u' - r'$ color by at most ~ 0.1 mag across the SB range probed. We note that our sample selection is biased against gas-depleted galaxies, which is expected to have redder $u' - r'$ colors. Therefore, at low-mass end, the median $u' - r'$ color measured from our sample may be bluer than the underlying population.

The SB dependence found in previous studies and in Figure 2.1 is likely mostly the dependence on stellar mass. Low SB galaxies have bluer optical color because they are on average less massive. At fixed stellar mass, low SB galaxies are not necessarily younger.

2.4.2 Star formation rates

Early studies often described low SB galaxies as dormant galaxies which possess immense gas reservoir but do not actively form stars (Gerristen & de Blok 1999). This property is a direct expectation from their low surface density. Because of the weaker self-gravitation, low surface density disks are stable against both global and local growth of instability (Dalcanton et al. 1997; Mihos et al. 1997; Mayer & Wadsley et al. 2004; Ghosh & Jog 2014). Gas clouds in low SB disks thus experience less cloud compression and collision, which can trigger star formation.

We see in Figure 2.5a and Figure 2.5b that the SFR is nearly independent of the SB at fixed stellar mass. It appears to be in tension with theoretical expectations. Nevertheless, Figure 2.5c shows that the SFE is SB dependent. At fixed stellar mass, lower SB galaxies possess more gas (Figure 2.4c), but are inefficient in turning the gas reservoir into stars. The null dependence of SB on SFR is the combined effect of the gas mass and SFE. Low SB galaxies are forming stars slowly from their immense gas reservoir.

2.4.3 Remarks on Surface Brightness

The surface brightness is extensively used to measure the effect of internal structure and local density on galaxy evolution. The implicit assumption in using surface brightness is that it is a good proxy for surface density. This assumption works better when the surface brightness is measured at a near-IR wavelength, where the stellar mass-to-light ratio is less dependent on properties of galaxies. However, it is worth noting that the surface brightness is only a proxy for the stellar component of galaxies. The gaseous component is ignored. Therefore, the "surface density" inferred from the surface brightness is essentially the "stellar surface density" but not the "baryonic surface density".

Using HI 21 cm line measurements from the ALFALFA survey and photometry from the SDSS, Huang et al. (2012) investigated the global scaling relations between the stellar and the gas mass of a sample of $\sim 10,000$ galaxies. From the scaling relation presented by Huang et al. (2012), galaxies with $M_\star \lesssim 10^{9.7} M_\odot$ are gas-dominant ($M_{HI} > M_\star$). Thus, for small galaxies, the gaseous component can be non-negligible if the baryonic content is the concern.

In addition to being used as a proxy for surface density, the SB is also taken as a proxy for the specific angular momentum of their parent halos. Low SB galaxies are considered as forming from halos of high specific angular momenta (Dalcanton et al. 1997; Boissier et al. 2003). As we have emphasized in this manuscript, the SB is strongly correlated with the stellar mass. Low SB galaxies can simply be less-massive galaxies. Using the SB as a proxy for angular momentum will only be meaningful while comparing galaxies of the same masses.

Moreover, secular evolution induced by internal structures such as stellar bars and spirals can redistribute angular momentum and matter within the galaxy disk, thus altering the SB (Hohl 1971; Lynden-Bell & Kalnajs 1972; Debattista et al. 2006; Minchev et al. 2011, 2012). Secular evolution can induce ~ 0.5 mag arcsec $^{-2}$ change in SB (Wu et al. 2016, in prep; see Chapter 4), a noticeable amount comparing to the intrinsic dispersion of SB at

fixed mass (~ 3 mag, Figure 2.2). The SB observed today may not be representative for the property of the host halos.

Because of the issues mentioned above, we should be careful interpreting results on the SB effect reported in the literature. The majority of studies defined “low surface brightness (LSB)” galaxy samples by selecting galaxies with surface brightness fainter than a certain value, then compared the properties of the LSB sample to other “normal”, or high surface brightness (HSB) galaxies. However, this simple definition yields a heterogeneous sample. An LSB galaxies may be a massive galaxy with an extended distribution of stars, a less massive galaxy, or a galaxy massive in baryons but gas-rich. These samples do not represent either high angular momentum galaxies, low surface density galaxies, or low mass galaxies. All conclusions made from “LSB” samples have to be interpreted with extra care.

2.4.4 Conclusion

We have re-examined the SB dependence on various galaxy properties at fixed stellar mass. This is the first step toward understanding the effect of angular momentum on galaxy evolution. We find some previous perceptions of the effect of SB should be reconsidered. Lower SB galaxies are inefficient in forming stars, but they are not necessarily quiescent due to their large gas reservoir. At fixed stellar mass, there is little evidence that the optical color of galaxies changes along with the SB. It is questionable whether LSB galaxies build up their mass with a different star-formation history as some studies suggested (e.g., Boissier et al. 2003). However, the integrated broadband color is a crude proxy for star-formation history, therefore, we cannot draw a firm conclusion. Spatially resolved spectroscopy will help derive the stellar age profiles of galaxy disks. We will understand better whether galaxies with different SBs build up through the same star-formation history or not. In the near future, large IFU galaxy surveys such as MANGA (Bundy et al. 2015) and SAMI (Bryant et al. 2015) will observe galaxies with stellar masses $\log(M_*/M_\odot) \gtrsim$ out to $\sim 2.5R_e$, provide samples with wider ranges of stellar masses and surface densities, allowing more detailed

investigation. We find that the metallicity strongly depends SB and we will investigate the origin of the effect in the next chapter.

References

- Boissier, S., Monnier Ragaigine D., Prantzos, N., et al. 2003, MNRAS, 343, 653
- Boselli, A., Cortese, L., Boquien, M., et al. 2014, A&A, 564, 66
- Bothun, G., Impey, C., McGaugh, S. 1997, PASP, 109, 745
- Bryant, J. J., Owers, M. S., Robotham, A. S. G., et al. 2015, MNRAS, 447, 2857
- Burkholder, V., Impey, C., Sparyberry, D. 2011, AJ, 122, 2318
- Bundy, K., Bershad, M. A., Law, D. R., et al. 2015, ApJ, 798, 7
- Cluver, M. E., Jarrett, T. H., Hopkins, A. M., et al. 2014, ApJ, 782, 90
- Conroy, C., Gunn, J. E., White, M., et al. 2009, ApJ, 699, 486
- Conroy, C., & Gunn, J. E. 2010, ApJ, 712, 833
- Dalcanton, J. J., Spergel, D. N. m Summers, F. J. et al. 1997, ApJ, 482, 659
- Debattista, V. P., Mayer, L., Carollo, C. M., et al. 645, 209
- de Blok, W. J. G., van der Hulst, J. M., Bothun, G. D. 1995, MNRAS, 274, 234
- Disney, M. J. 1976, Nature, 263, 573
- Dutton, A. A., van den Bosch, F. C., Dekel, A., & Courteau, S. 2007, ApJ, 654, 27
- Ellison, S. L., Patton, D. R., Simard, L., et al. 2009, ApJ, 672, 107

Galaz, G., Dalcanton, J. J., Infante, L., & Treister, E. 2002, *AJ*, 124, 1360

Gallazzi, A., Charlot, S., Brinchmann, J., et al. 2005, *MNRAS*, 362, 41

Gerristen, J. P. E., de Blok, W. J. G. 1999, *A&A*, 342, 655

Ghosh, S., & Jog, C. J. 2014, *MNRAS*, 439, 929

González Delgado, R. M., Cid Fernandez, R., García-Benito, R., et al. 2014, *ApJ*, 791, 16

Hao, C., Kennicutt, R. C., Johnson, B. D. et al. 2011, *ApJ*, 741, 124

Haynes, M. P., Giovanelli, R., Martin, A., et al. 2011, *AJ*, 142, 170

Hohl, F. 1971, *ApJ*, 168, 343

Huang, S., Haynes, M. P., Giovanelli, R., & Brinchmann, J. 2012, *ApJ*, 756, 113

Impey, C. D., Sprayberry, D., Irwin, M. J., & Bothun, G. D. 1996, *ApJS*, 105, 209

Kennicutt, R. C., Jr. 1998, *ARA&A*, 36, 189

Lynden-Bell, D. & Kalnajs, A. J. 1972, *MNRAS*, 157, 1

Mayer, L. & Wadsley, J. 2004, *MNRAS*, 347, 277

McGaugh, S. S., & de Blok, W. J. G. 1997, *ApJ*, 481, 689

Mihos, J. C., McGaugh, S. S., & de Blok, W. J. G. 1997, *ApJ*, 477, 79

Minchev, I., Famaey, B., Combes, F., et al. 2011, *A&A*, 527, 147

Minchev, I., Famaey, B., Quillen, A. C., et al. 2012, *A&A*, 548, 126

Mo, H. J., Mao, S., White, S. D. M. 1998, *MNRAS*, 295, 319

Noeske, K., Weiner, B. J., Faber, S. M., et al. 2007, *ApJ*, 660, 43

O'Neil, K., Bothun, G. D., Schombert, J. 2000, *AJ*, 119, 136

Panter, B., Jimenez, R., Heavens, A. F., Charlot, S. 2008, MNRAS, 391, 1117

Schlafly, E. F. & Finkbeiner, D. P. 2011, ApJ, 737, 103

Schombert, J. M., Dothun, G. D., Schneider, S. E., McGaugh, S. S. 1992, AJ, 103, 1107

Schombert, J. M., Maciel, T., McGaugh, S. 2011, AdAst, 2011, 12

Schombert, J. M., & McGaugh, S. 2014, PASA, 31, e011

Tremonti, C. A., Heckman, T. M., Kauffmann, G., et al. 2004, ApJ, 613, 898

Tully, R. B., Pierce, M. J., Huang, J., et al. 1998, AJ, 115, 2264

Tully, R. B., Rizzi, I., Shaya, E. J., et al. 2009, AJ, 138, 323

Tully, R. B., Verheijen, M. A. W., Pierce, M. J., Huang, J., & Wainscoat, R. J. 1996, AJ, 112, 6

White, S. D. M., & Frenk, C. S. 1991, ApJ, 379, 52

White, S. D. M., & Rees, M. J. 1978, MNRAS, 183, 341

Wright, E., Eisenhardt, P. R. M., Mainzer, A. K. et al. 2010, AJ, 140, 1868

Wu, P.-F., Kudritzki, R., Tully, R. B., Neill, J. D. 2015, ApJ, 810, 151

Yuan, H. B., Liu, X. W., & Xiang, M. S. 2013, MNRAS, 430, 2188

Zhong, G. H., Liang, Y. C., Liu, F. S., et al. 2008, MNRAS, 391, 986

Chapter 3

The influence of surface brightness on the mass-metallicity relation

3.1 Introduction

Chemical enrichment is one of the keys to understand the evolution of galaxies. Heavy elements, or metals, are synthesized in stars then released into the interstellar medium (ISM) by stellar winds or supernova explosions. The metal-enriched ISM subsequently acts as the raw material for the next generation of new-born stars. Tight relations between the stellar mass and both gas-phase and stellar metallicities were discovered, such that galaxies with larger stellar masses on average have higher metallicities (Tremonti et al. 2004; Gallazzi et al. 2005; Savaglio et al. 2005; Lee et al. 2006).

To first order, the origin of the mass-metallicity relation can be understood as a simple process of recycling of metals in the ISM. Galaxies with larger stellar mass have synthesized and released more heavy element throughout their lives, therefore, higher metallicity is naturally expected. Nevertheless, this simple picture does not tell the whole story. As pointed out by Tremonti et al. (2004), the dispersion in the mass-metallicity relation cannot be explained simply by measurement uncertainties of metallicity. There must be other factors affecting the metallicity.

Several studies have been searching for parameters beyond stellar mass that affect metallicity. An anti-correlation between gas-phase metallicity and star formation rate (SFR)

has been found both locally and at high redshifts, where at fixed stellar mass, galaxies with higher SFR have lower metallicity (Ellison et al. 2008; Mannucci et al. 2010; Lara-López et al. 2010; Yabe et al. 2015). A similar anti-correlation seems also to be present between the gas content and metallicity, where gas-rich galaxies have on average lower metallicity (Bothwell et al. 2013; Hughes et al. 2013). There is also a dependency on galaxy structure, such that larger, or lower surface brightness, galaxies tend to have lower metallicity for their stellar mass (Ellison et al. 2008; Liang et al. 2010; Salim et al. 2014).

Most of these results are obtained with data from SDSS fiber spectra. Although the sample size is large and provides good statistics, data from fiber spectra have fundamental issues. The spectroscopic information, including SFR and metallicity, comes from only the center of the galaxy while stellar mass, gas mass, and galaxy structure are derived from imaging with different apertures. Moreover, the coverage varies among galaxies, depending on the size, structure and distance of galaxies. Therefore, some of the dependencies on a second parameter could come from aperture effects (Ellison et al. 2008; Hughes et al. 2013; Sánchez et al. 2013). This calls for an approach that uses spatially resolved information regarding metallicity.

In the interpretation of the observed relationship between integrated metallicity and stellar mass, it has become clear that a simple closed box chemical evolution model with no exchange of material between the galaxies and their outside environment (Searle & Sargent 1972; Pagel & Patchett 1975) is insufficient. In reality, galaxies experience gas inflows from mergers and accretion and outflows caused by feedback from supernovae, starburst or AGN and, thus the close-box assumption does not hold. Exchanging material between galaxies and the environment modifies the metallicity of galaxies. By introducing inflow and outflow activities, theoretical models are able to reproduce quantitatively the observed integrated mass-metallicity relation (Spitoni et al. 2010; Peeples & Shankar 2011; Zahid et al. 2012; Lilly et al. 2013; Zahid et al. 2014).

With spatially resolved observations, to overcome the uncertainties mentioned above a modified theoretical approach is also required, which utilizes the additional information

coming from the measurement of radially resolved metallicity profiles. Recently, a variety of such models has been presented (Pilkington et al. 2012; Mott et al. 2013; Kudritzki et al. 2015). This allows the imposition of constraints on the inflow and outflow properties of individual galaxies by chemical evolution models (Ascasibar et al. 2015; Kudritzki et al. 2015), and then the investigation of whether there is any dependence on other physical properties of galaxies.

In this paper, we focus on the effect of surface brightness on the mass-metallicity relation. The surface brightness, or surface density, of a galaxy depends on the angular momentum of a galaxy for a given mass (Dalcanton et al. 1997; Mo et al. 1998), which is affected by the mass loss and accretion history of a galaxy (Dutton & van den Bosch 2012). We will examine the interplay among surface brightness, metallicity, and properties of inflow and outflow of gas from nearby galaxies, where the spatially-resolved information is available. In Section 2, we describe the data sets used in the analysis. Section 3 presents the dependence of metallicity on surface brightness inferred from both spectroscopy and broadband color in two independent samples. We use chemical evolution models to constrain the inflow and outflow of galaxies in Section 4, and discuss possible implications and systematics in Section 5. The summary is given in Section 6. We use AB magnitudes in this paper unless noted.

3.2 Data and Analysis

3.2.1 Samples

In this paper, we present two samples of galaxies with metallicities estimated from spectra of H II regions and broadband colors respectively. We use data from surveys including the WISE, the SDSS, and the ALFALFA. The synergy among these large surveys allows us study a large number of galaxies with homogeneous observations. The distribution of the stellar mass, gas mass, gas fraction, and surface brightness of the sample is presented in Figure 3.1.

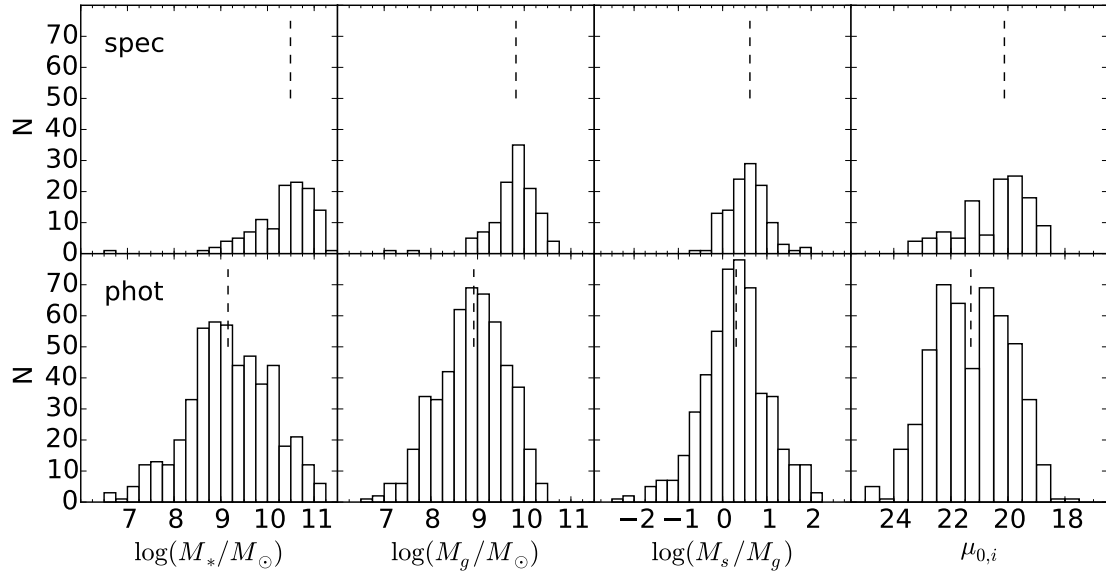


Figure 3.1 Distributions of stellar mass, gas mass, stellar-to-gas mass ratio and surface brightness with the spectroscopic sample (top) and the photometric sample (bottom). The vertical dashed line is the median value of each quantity.

Spectroscopic Sample

The first sample consists of 118 galaxies with gas-phase metallicities measured from H II regions in Pilyugin et al. (2014). This paper compiled published spectra of H II regions in 130 nearby galaxies and determined the gas-phase metallicity of each H II region in a uniform way. For each galaxy, Pilyugin et al. (2014) reported the central metallicity and metallicity gradient as a function of radius. This set of galaxies provides a homogenized sample with spatially resolved information. We select galaxies whose H I flux is available for further discussion and refer this sample as the spectroscopic sample

The top row of Figure 3.1 shows the properties of the spectroscopic sample. The majority of galaxies in this sample have stellar mass $M_* \gtrsim 10^{10} M_\odot$ and relatively high surface brightness while the distributions have tails towards lower masses and lower surface brightnesses. This sample covers a specific range of stellar-to-gas mass ratio, $0 \lesssim \log(M_*/M_g) \lesssim 1$, i.e., $0.1M_* \lesssim M_g \lesssim 1M_*$. Few galaxies are located beyond this range.

Photometric Sample

The second sample is the galaxy sample used in Chapter 2. This sample covers wider ranges of stellar mass, gas mass, stellar-to-gas mass ratio, and surface brightness than the spectroscopic sample, especially for the low mass, low surface brightness and gas-rich end of the distribution (Figure 3.1). We refer to this sample as the photometric sample.

3.2.2 Photometry, surface brightness profile, and masses

We perform surface photometry and derive the mass of the spectroscopic sample using the same procedure for the photometric sample, which has been described in Chapter 2.

In this chapter, we also consider the molecular gas content of galaxies for the spectroscopic sample for the chemical evolution model (see section 3.4). However, we do not have direct observations of the molecular gas towards our galaxies. To estimate the molecular gas content, we refer to the result of Bothwell et al. (2014), who measured CO gas content towards ~ 100 galaxies. Bothwell et al. (2014) found that the molecular-to-atomic gas mass ratio (M_{H_2}/M_{HI}) has a positive correlation with the stellar mass of galaxies with some scatter. From figure 2 of Bothwell et al. (2014), we estimate the molecular-to-atomic gas mass ratio:

$$\log(M_{H_2}/M_{HI}) = 0.66 \times \log(M_*/M_\odot) - 7.392 \quad (3.1)$$

Therefore, the molecular mass is estimated from the combination of stellar and H I mass. Throughout this chapter, "gas mass" refers to the total gas mass, $M_{atom} + M_{H_2}$. We will discuss the uncertainties and possible systematics in Section 3.5.2.

3.3 The Surface Brightness Dependence on Metallicity

In this section, we present the correlation between metallicity and surface brightness from two methods in two independent samples. Going one step farther than existing studies, our analysis considers both the stellar mass and gas mass and shows that the surface brightness

dependence does not come from correlations between surface brightness and stellar mass or gas mass alone.

3.3.1 Gas-phase Metallicity from Spectroscopy

All galaxies in our spectroscopic sample have central metallicities and metallicity gradient reported in Pilyugin et al. (2014). The first step is to verify whether the result in previous studies, that the higher surface brightness galaxies have higher metallicities at given stellar mass, still holds if we take the average metallicity of the whole galaxy instead of the central metallicity as measured from fiber spectra. However, without knowing the spatial distribution of the gas, we cannot directly convert this information into average metallicity over the whole galaxy. Here we estimate the average metallicity by assuming an exponential gas disk, whose scale length scales with the size of the optical disk (R_{25}) (Bigiel & Blitz 2012):

$$\Sigma_{gas} \propto e^{(-1.65 \times r/R_{25})}, \quad (3.2)$$

We calculate the average metallicity out to R_{25} :

$$\langle Z \rangle = \frac{\int_0^{R_{25}} \Sigma_{gas} (Z_0 + dZ/dr \times r) 2\pi r dr}{\int_0^{R_{25}} \Sigma_{gas} 2\pi r dr}, \quad (3.3)$$

where $\langle Z \rangle$, Z_0 , and dZ/dr are the average metallicity, the central metallicity and the metallicity gradient, respectively.

Figure 3.2a shows the central metallicity as a function of the stellar mass of the spectroscopic sample. The sample is divided into two subsamples by surface brightness. First of all, the central metallicity shows the mass-metallicity relation as expected. Overall, higher surface brightness galaxies are more metal-rich, mainly due to their more massive nature. But it is also clear that at $M_* \lesssim 10^{10.5} M_\odot$, most higher surface brightness galaxies have the highest metallicity for given mass, while no obvious distinction exists between the two subsamples at higher mass. This finding is qualitatively in agreement with previous studies by SDSS fiber spectra (Ellison et al. 2008; Liang et al. 2010; Salim et al. 2014), where

for a given mass, high surface brightness, or compact, galaxies have higher metallicities, and the distinction is larger at the low mass end.

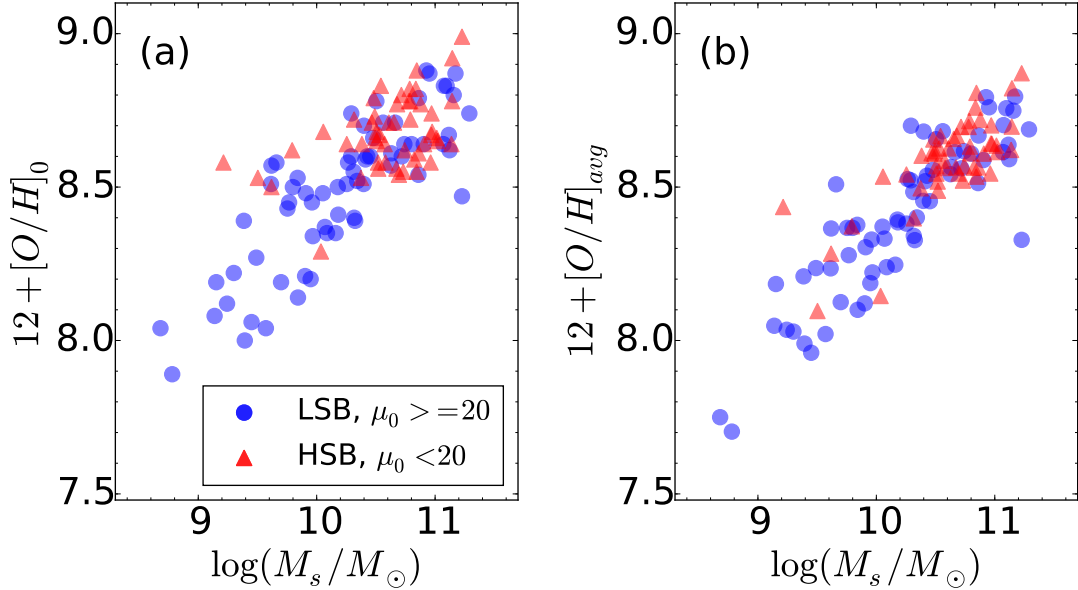


Figure 3.2 *Left:* Central metallicity as a function of stellar mass, color-coded by surface brightness. The higher and lower surface brightness galaxies are red triangles and blue circles, respectively. The surface brightness dependence is more prominent at the low mass end. *Right:* Average metallicity as a function of stellar mass. The metallicity is averaged out to R_{25} . At high stellar mass ($M_* > 10^{10.5}M_\odot$), no surface brightness dependence is seen. At low stellar mass, higher surface brightness galaxies are mostly located above the mean at fixed stellar mass, but the difference is not as prominent as seen in the left panel. Previous measurements from the SDSS fiber spectra are potentially biased due to the aperture effect.

Next, we show the average metallicity in Figure 3.2b. Here, at $M_* \lesssim 10^{10.5}M_\odot$, the distinction between two samples is not as clear as in Figure 3.2a. We only find a tentative trend that higher surface brightness subsample locates at the top half of the mass-metallicity relation. We have computed the average metallicity with a few different assumptions of gas profiles (see Section 3.4 for profiles used) and the results are similar.

A size dependence on the mass-metallicity relation has been found in the SDSS spectra, such that galaxies with larger effective radii on average have lower metallicity (Ellison et al. 2008), effective the same as we find here in terms of surface brightness. However, the

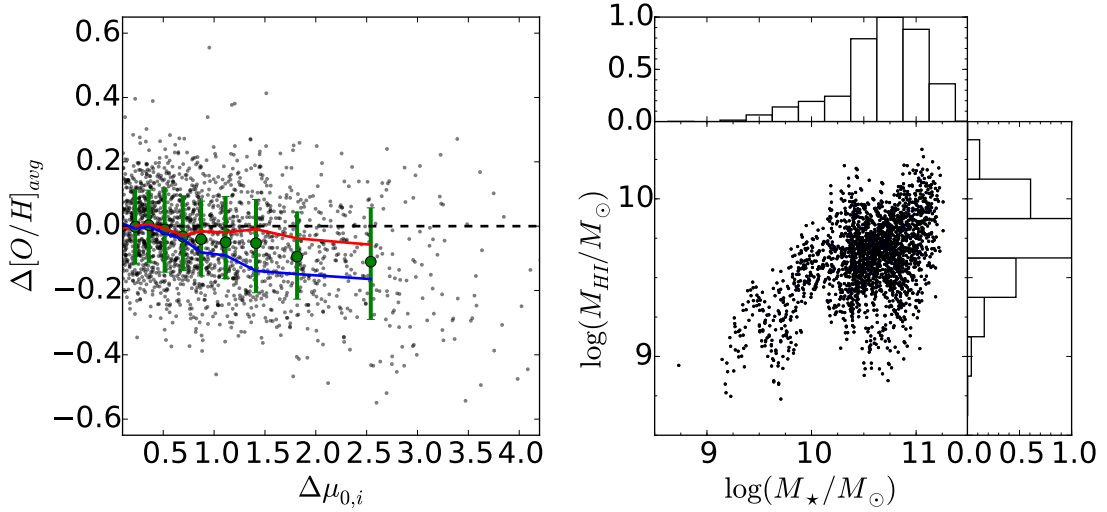


Figure 3.3 *Left*: Comparisons between galaxies with similar stellar and gas mass. Each data point comes from two galaxies with $\Delta \log(M_*) < 0.3$ and $\Delta \log(M_g) < 0.3$. The horizontal axis is the difference in surface brightness, calculated from the lower surface brightness one (larger $\mu_{0,i}$) minus the higher one (smaller $\mu_{0,i}$). The vertical axis is the difference in average metallicity. We divide the whole data set into 10 equal-size $\Delta\mu_{0,i}$ bins. The median and 16th and 84th percentile of the distribution in each bin are shown as the green error bar. There is a clear trend that, after taking both stellar and gas mass into consideration, lower surface brightness galaxies are on average more metal-poor. We further split the sample into 2 stellar mass bins, and plot the median of each subsample for each $\Delta\mu_{0,i}$ bins in red ($M_* > 10^{10.5} M_\odot$) and blue ($M_* \leq 10^{10.5} M_\odot$), respectively. The surface brightness effect is larger at low mass than in high mass. *Right*: The stellar and gas mass distribution of the data points in the left panel. The masses are calculated as the average mass of the two galaxies in consideration.

metallicity derived from SDSS spectra potentially suffers from systematic aperture effect. Only part of the galaxy light is enclosed by the aperture, and the covering fraction depends on the size of the galaxy. Ellison et al. (2008) was aware of this issue and argued that the effect is small and cannot create the size dependence found in the SDSS sample. Using spatially-resolved spectra, Pilyugin et al. (2014) examined the relation between the disk surface brightness and the metallicity at the center and R_{25} . They found that either at the center or R_{25} , galaxies with higher surface brightness on average have higher metallicities. Here we further calculate the averaged metallicity and confirm that the surface brightness dependence exists.

The gas-phase metallicity is the ratio between metals and hydrogen. The numerator, the metal content, is related to the stellar mass while the denominator is the total gas content of the galaxy. In observations, metallicity has been found to be tightly correlated with both the gas mass and stellar-to-gas mass ratio (Bothwell et al. 2013; Hughes et al. 2013; Zahid et al. 2014). If lower surface brightness galaxies are on average more gas-rich, it would provide a direct explanation of the observed surface brightness dependence. A proper comparison will be between galaxies with both the same stellar and gas masses but difference surface brightnesses.

To make such a comparison, we pick out pairs of galaxies with similar stellar and gas masses ($dM < 0.3$ dex) from the sample and compute the difference in surface brightness ($\Delta\mu_{0,i}$) and metallicity ($\Delta[O/H]_{avg}$) between the two galaxies. Figure 3.3 shows the metallicity deficiency of a lower surface brightness galaxy compared to a higher surface brightness galaxy with similar mass. Each data point represents a comparison between two galaxies. A galaxy can appear more than once in the figure because there can be multiple galaxies with similar stellar and gas mass. We divide the data points into 10 equal-size $\Delta\mu_{0,i}$ bins and show the median and the 16th and 84th percentile of the distribution in each bin.

The difference, $\Delta[O/H]$, starts from 0 at $\Delta\mu_{0,i} = 0$, and gradually becomes more negative as $\Delta\mu_{0,i}$ increases (lower surface brightness). This result indicates that at the same stellar *and* gas mass, the metallicity depends on the surface brightness of galaxies. The difference between low and high surface brightness galaxies seen in Figure 3.2 cannot be entirely attributed to their gas content. We further split the sample into two stellar mass bins. The surface brightness dependence is more prominent in the lower mass bin. The surface brightness effect is presented only at $\Delta\mu_{0,i} \gtrsim 2$ in the higher mass bin, therefore it is not identified in Figure 3.2.

3.3.2 Stellar Metallicity from Broadband Colors

We have seen that the average gas-phase metallicity of a galaxy depends on its surface brightness, and the effect is more prominent at lower masses. Also, in Chapter 2, we have used the broadband color as a proxy for stellar metallicity and found the same surface brightness dependence at fixed stellar mass. We then compare the stellar metallicity of galaxies at fixed stellar and gas masses in this section.

Similar to Figure 3.3, Figure 3.4 compares the $z' - W1$ colors of two galaxies with similar stellar and gas masses. For galaxies with $u' - g' \leq 1.0$, we further require $\Delta(u' - g') \leq 0.05$ in addition to the mass limit in order to mitigate the age effect. We divide the data into 15 equal-size $\Delta\mu_{0,i}$ bins and plot the median, 16th and 84th percentile of the distribution. Again, the difference in color starts from 0 at $\Delta\mu_{0,i} = 0$ and becomes more negative at larger $\Delta\mu_{0,i}$, indicating that lower surface brightness galaxies have systematically lower stellar metallicities for a given stellar *and* gas mass.

We have estimated the internal extinction following the prescription of Tully et al. (1998) based on the H I line width and the inclination of galaxies, for which we have information for all sample galaxies. However, this prescription does not consider the surface brightness of galaxies. If the metallicity of galaxies depends on the surface brightness, the internal extinction would depend on the surface brightness as well. Thus, the prescription of Tully et al. (1998) could systematically overestimate the internal extinction of low surface brightness galaxies if they are metal-poorer as suggested in previous studies. An arguably better method is to estimate from the flux ratio between total infrared (TIR) and UV luminosities (Kong et al. 2004; Buat et al. 2005; Gil de Paz et al. 2007). The TIR flux represents the continuum light absorbed then re-emitted by dust while the UV flux is the radiation from young stars unblocked by dust. Therefore, the flux ratio between TIR and UV is a proxy of the ratio between attenuated and unattenuated light. However, only $\sim 20\%$ of our galaxies are detected in the W4 band, so this method cannot be applied in our case. When IR data are not available, a common alternative is using UV spectral slope or UV color to infer the TIR-UV flux ratio (Cortese et al. 2006; Salim et al. 2007) because there is a positive

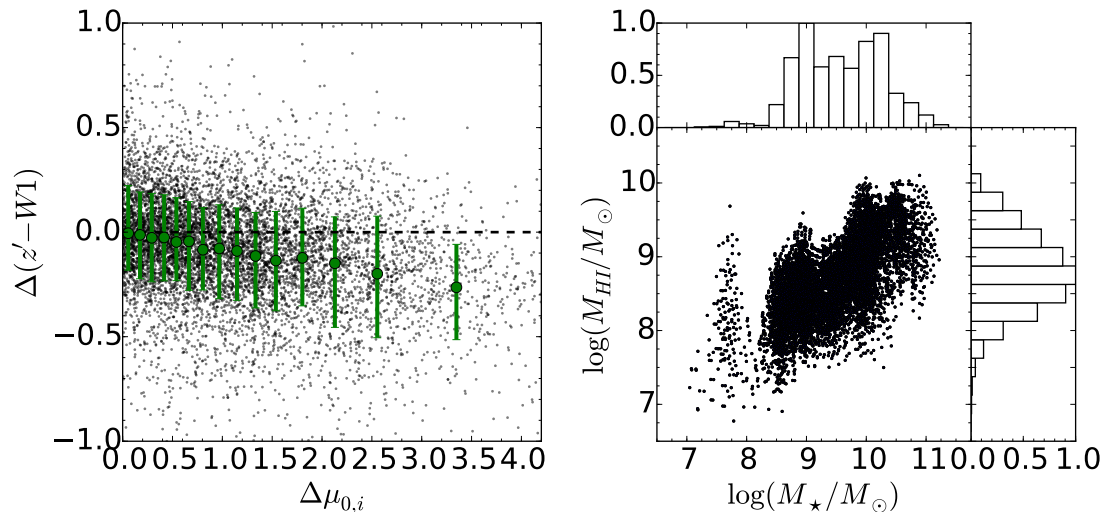


Figure 3.4 *Left*: The comparison between galaxies with similar stellar and gas masses. Each data point comes from a pair of galaxies with $\Delta \log(M_*) < 0.3$ and $\Delta \log(M_g) < 0.3$. For galaxies with $u' - r' < 1.0$, we further require $\Delta(u' - r') < 0.05$. The data set is divided into 15 equal-size $\mu_{0,i}$ bins and the median and 16th and 84th percentile in each bin is shown by the green error bar. At the same stellar and gas masses, lower surface brightness galaxies have smaller $z' - W1$ colors, indicating lower stellar metallicities. *Right*: The stellar and gas mass distributions of the data points in the left panel. The masses are calculated as the average mass of the two galaxies in consideration.

correlation between the TIR-UV flux ratio and the slope of the UV spectrum (the $IRX - \beta$ relation; Kong et al. 2004; Gil de Paz et al. 2007), although dependence on age and dust property may exist (Kong et al. 2004; Cortese et al. 2006; Gil de Paz et al. 2007).

To make sure our results are not inherited from the potential systematics of the Verheijen & Sancisi (2001) prescription, we also carry out the analysis with internal extinction estimated from the observed UV colors for galaxies with both GALEX FUV and NUV imaging ($\sim 90\%$ of our samples). We follow the calibration of Hao et al. (2011):

$$A_{FUV} = 3.83 \times [(FUV - NUV)_{obs} - 0.022], \quad (3.4)$$

and find that both prescriptions for internal extinction give qualitatively similar results.

We would like to point out that, in both our samples, the surface brightness dependence is only moderate compared to variations from individual galaxies. The individual variations may dominate in galaxy samples that are too small in size or do not cover a wide enough range of surface brightnesses. Therefore, the surface brightness effect may not be detected. It will be possible in the near future to draw a cleaner picture with upcoming integral field unit (IFU) surveys such as MANGA (Bundy et al. 2015) or SAMI (Bryant et al. 2015), that can provide spatially resolved metallicity maps of a large number of galaxies over wide ranges of mass and surface brightness.

Also, we note that under the exponential disk assumption our result on the surface brightness dependence could be interpreted as a scale length (h) dependence because galaxies at the same stellar mass with higher central disk surface brightnesses have smaller scale lengths. In general, galaxies are not perfect exponential disks, and the relation between μ_0 and h will depend on the structure of galaxies. For our cases, we have repeated a similar analysis as shown in Figure 3.3 and Figure 3.4, but as a function of Δh , and find similar results.

3.4 Theoretical Considerations

A large number of studies have modeled the observed mass-metallicity relation with different approaches and formulations. It is widely agreed that the close-box assumption yields too high metallicity. Outflows removing metal-enriched ISM and/or inflows of pristine gas diluting ISM are required to quantitatively match the observed mass-metallicity relation (Spitoni et al. 2010; Peeples & Shankar 2011; Zahid et al. 2012; Lilly et al. 2013; Zahid et al. 2014).

While in these works, the spatially integrated mean relation is successfully reproduced, there is little work addressing the scatter around the mean. We have shown in Section 3.3 that, for a given mass, the metallicity is correlated with the surface brightness. It is

intriguing to investigate how the spatially resolved surface brightness and metallicity profiles are affected by the inflow and outflow properties.

For this purpose, we apply the chemical evolution model of Kudritzki et al. (2015), which addresses the relation among inflow, outflow, metallicity and stellar-to-mass ratio in the spatially resolved case. The inflow and outflow of a galaxy are parameterized by two factors:

$$\Lambda = \frac{\dot{M}_{accr}}{\psi} \quad (3.5)$$

and

$$\eta = \frac{\dot{M}_{loss}}{\psi} \quad (3.6)$$

where \dot{M}_{loss} and \dot{M}_{accr} are the mass-loss and mass-accretion rates, and ψ is the SFR.

This model makes a few assumptions. First, η and Λ are assumed to be constant in time. This assumption constrains only the ratio between the SFR and inflow and outflow rate, therefore, all three quantities can be time variable. Second, the inflow gas is free of metals, and the outflow gas has the same metallicity as the ISM at the time launched. Third, the nucleosynthetic yield (y) and the stellar mass return fraction (R) are both constant. Under these assumptions, the metallicity can be analytically expressed as

$$Z(t) = \frac{y}{\Lambda} \left\{ 1 - \left[1 + \left(1 + \frac{\eta - \Lambda}{1 - R} \right) \frac{M_*(t)}{M_g(t)} \right]^{-\frac{\Lambda}{(1-R)(1+\frac{\eta-\Lambda}{1-R})}} \right\}. \quad (3.7)$$

Therefore, the metallicity is determined by η , Λ , and the stellar-to-gas mass fraction at a given time. If a galaxy has spatially resolved information on stellar mass, gas mass, and metallicity, the three constraints can be used to find the best-fit η and Λ of the galaxy. We refer readers to Kudritzki et al. (2015) for a detailed derivation and discussion of the model.

We apply the model only to the spectroscopic sample but not the photometric sample. The stellar metallicity inferred from broadband colors can depend on stellar population synthesis models and is less certain for quantitative work (Lee et al. 2007; Eminian et al. 2008).

For each galaxy in the spectroscopic sample, we have both the metallicity and stellar mass profiles from observations. For the gas distribution, we follow the form in Equation 3.2, and assume a pure exponential gas disk with a slope scaled with R_{25} . This assumption is supported by observations between 0.2 and 1.0 R_{25} but is not valid for radii outside this range (Bigiel & Blitz 2012). Therefore, our nominal range for analysis is limited between 0.2 R_{25} and 1.0 R_{25} . For the amount of gas within this range, we do the analysis under two separate assumptions. The first one involves distributing the observed amount of gas exponentially from the galaxy center to infinity. Therefore, the gas surface density is determined by both R_{25} and the integrated observed gas content. But the validity of this assumption is potentially affected by the gas profile beyond R_{25} . Thus, we assume as an alternative a gas surface density profile, which is only constrained by R_{25} (Bigiel & Blitz 2012):

$$\Sigma_{gas} = 28 \times \exp(-1.65 \times r/R_{25}). \quad (3.8)$$

Although the second assumption, determining gas density profile purely from the size of stellar disk, may seem to be less convincing, it is in fact supported by observations (Bigiel & Blitz 2012). Comparing the two assumptions with the 19 galaxies studied in Kudritzki et al. (2015), which have resolved gas distribution, we find that the first (second) assumption on average yields ~ 0.17 dex (~ 0.11 dex) lower gas surface density than measured values within the nominal radius range. As we will find out later, this range of uncertainty is not a concern for our discussion.

For each galaxy, we have now the photometrically derived stellar mass column density profiles and gas column density profiles described by Equation 3.8. We now calculate model metallicity profiles from the stellar-to-gas mass ratio profile and pairs of η and Λ between 0 and 3 for every hundredth interval. We adopt $R = 0.4$ and $y = 0.00313$ as calibrated in Kudritzki et al. (2015). A 0.15 dex is added to the H II-region metallicity measured by Pilyugin et al. (2014) to match the metallicity zero-point obtained by Kudritzki et al. (2015) as the result of stellar spectroscopy in spiral galaxies. We then compare the

model metallicity profile with the observed metallicity profile and compute the χ^2 from the difference between two profiles and the uncertainties for every 0.05 R_{25} from 0.2 R_{25} to 1.0 R_{25} or the last reliable measurement of surface brightness for adopted pairs of η and Λ . The pair of η and Λ with the minimum χ^2 is then defined as the best fit model. Figure 3.5 shows an example of our comparison between the model and the observation. We note that the assumption on the gas profile is valid only in a statistical sense. There is $\sim 60\%$ scatter among individual galaxies. Therefore, we will only discuss the average properties from the model.

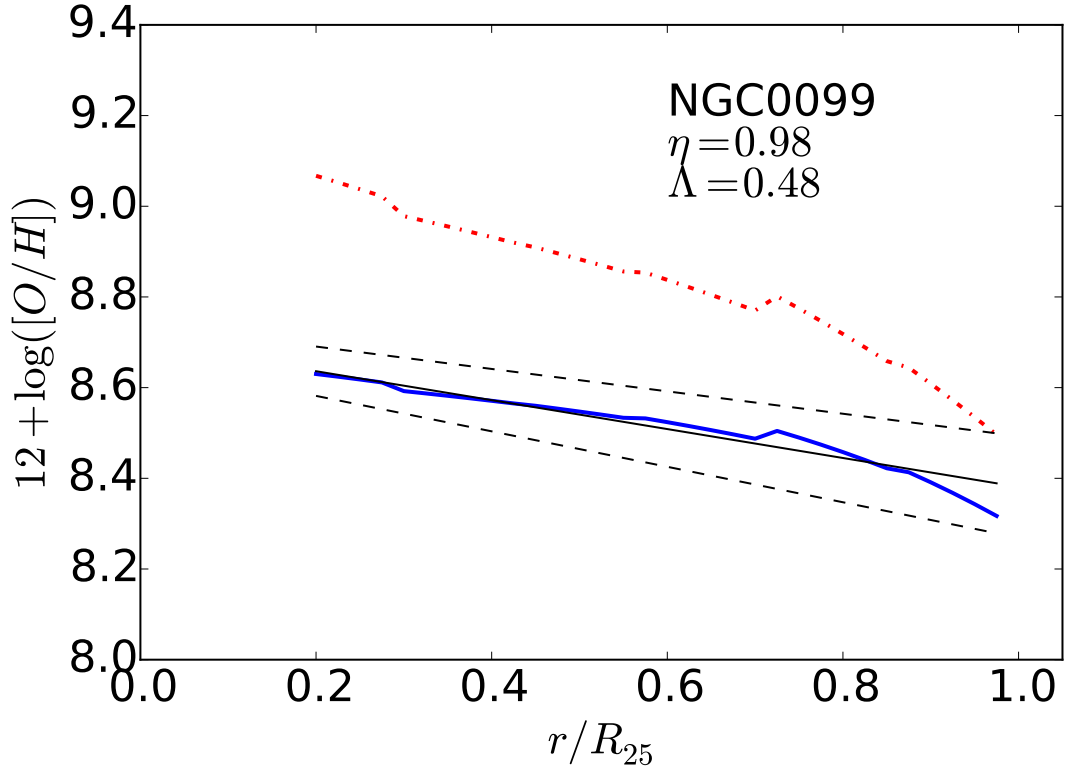


Figure 3.5 An example of the model fit. The black line represents the observed radial metallicity profile, with the 1σ uncertainty indicated by the dashed lines. The best-fit model metallicity profile is plotted as the blue line. The close-box model ($\eta = 0, \Lambda = 0$) is shown by the red dash-dotted line as a reference.

Our result with two different gas profiles is presented in Figure 3.6. Galaxies are first sorted into 3 bins in baryonic (Figure 3.6a and c) or stellar mass (Figure 3.6b and d). In each mass bin, galaxies are further separated into two equal-size bins by their surface brightness. Each bin contains ~ 20 galaxies. We show the median and the 16 and 84 percentile of the distributions of η and Λ in each sub-sample. The difference between the median surface brightnesses of the two sub-sample is ~ 1 mag for the high and mid-mass bins, and ~ 2 mags for the low-mass bin. As a comparison, we also plot the best-fit η and Λ from the 19 galaxies with measured stellar-to-gas mass profiles studied by Kudritzki et al. (2015).

To investigate the uncertainty resulting from the parameterized gas profile, we considered four more different gas profiles. Following the 1σ scatter of the slope of the universal gas profile given in Bigiel & Blitz (2012), we first consider two cases where the gradient of the gas distribution is -1.78 or -1.49, instead of the canonical value of -1.65. For the other two cases, we fix the gradient, but double or half the amount of gas in order to access the uncertainty from the assumed amount of gas and the effect from possible systematics (see Section 3.5.2 for more discussion). For all four cases, the median η and Λ of each sub-sample is calculated and plotted in the lower panels of Figure 3.6. Variation in slope is shown by light filled symbols and variation in gas amount is shown by open symbols.

Generally, both η and Λ depend on the mass of galaxies, where higher mass galaxies have on average lower η and Λ . However, η depends strongly on the gas amount assumed. Without knowing the amount of gas, η is essentially not constrained in the lowest mass and lower surface brightness bin. In all subsamples, the difference in η between high and low surface brightness bins could come from systematically different assumed gas amounts, if there is any. On the other hand, Λ is more robust against variations in gas profiles. In the two low mass bins, lower surface brightness galaxies have larger Λ regardless of gas profile assumed.

The same result also can be seen in galaxies with observed stellar-to-gas mass profiles (open diamonds). Only Λ in the low mass bin shows a surface brightness dependence, while

η , and Λ in the high mass bin does not seem to depend on surface brightness. However we note that this result comes from a small sample of only 5 galaxies in each bin.

3.5 Discussion

3.5.1 Implications from the Mass and Surface Brightness Dependence on Λ

A chemical evolution model suggests that, for given mass, lower surface brightness galaxies tend to have larger Λ . In this section, we discuss possible explanations for the correlation between Λ and the surface brightness of a galaxy.

Star Formation Efficiency

The parameter Λ is the gas accretion rate divided by star-formation rate. It can be understood as the reciprocal of star formation efficiency; while gas is falling onto the galaxy, Λ monitors how much of it is turned into stars. A larger Λ indicates inefficient star formation.

Our model suggests that lower surface brightness galaxies are less efficient in turning gas into stars, which is in agreement with the prevalent idea. Observations of giant low surface brightness galaxies ($M_* \gtrsim 10^{10} M_\odot$) showed that they have copious amounts of H I gas that is comparable to their stellar components (Matthews et al. 2001; O’Neil et al. 2004). Their gas-to-stellar mass ratio is higher than their high surface brightness counterparts (Burkholder et al. 2001; O’Neil et al. 2007). By comparing star formation rate and H I mass, Boissier et al. (2007) found that low surface brightness galaxies have lower SFR compared to high surface brightness galaxies with similar H I mass, evidence that low surface brightness galaxies are inefficient in star formation.

The low star formation efficiency in low surface brightness galaxies is also suggested by theories that low surface brightness galaxies are stable against the growth of instability (Dalcanton et al. 1997; Mihos et al. 1997; Mayer & Wadsley et al. 2004; Ghosh & Jog 2014).

The instability can be measured by the Toomre Q parameter (Toomre 1964):

$$Q \equiv \frac{\sigma \kappa}{3.36 G \Sigma_d}, \quad (3.9)$$

where σ is the radial velocity dispersion, G is Newtonian gravitational constant, Σ_d is the disk surface density. κ is the epicyclic frequency given by

$$\kappa \equiv \sqrt{\frac{2\Omega}{R} \frac{d}{dR}(R^2\Omega)}, \quad (3.10)$$

where R is the radial coordinate and Ω is the angular velocity. σ , Σ_d , Ω , and κ are all functions of R . Toomre (1964) showed that if Q drops to ~ 1 , the disk is unstable to radial perturbations.

Stability analysis of individual low surface brightness galaxies demonstrated that they have high Toomre Q parameter (Mihos et al. 1997; Ghosh & Jog 2014). Structures like spiral arms and bars are also harder to form due to a lack of global instability (Mihos et al. 1997). Gas clouds in low surface brightness disks experience fewer cloud collisions and compression, which can trigger star formation. This proposition is also supported by the fact that fewer bars are seen in low surface brightness galaxies (Impey et al. 1996). The larger Λ inferred from our model, thus, agrees with the majority of previous studies in terms of star formation efficiency.

Environmental Effect

Since Λ is the ratio between mass accretion rate and star formation rate, for two galaxies with the same stellar mass, the one with higher Λ , found to correlate with lower surface brightness, should have had more inflow material over time. This may imply that there is a surface brightness dependence with the environment of galaxies. At fixed mass, lower surface brightness galaxies tend to form in regions receiving more accretion flows.

Kereš et al. (2009) investigated the accretion rate of galaxies with cosmological hydrodynamical simulation and found a significant difference between the accretion rates

of central and satellite galaxies, such that central galaxies have on average higher accretion rates. Our result may imply that at fixed mass, low surface brightness galaxies tend to be central galaxies. In observation, Weimann et al. (2009) investigated the environmental effect on sizes and surface brightness profiles of galaxies in terms of centrals and satellites. For SDSS galaxies with $M_* > 10^{9.75} M_\odot$, Weimann et al. (2009) found that at fixed stellar mass, late type central galaxies have larger radii and are less concentrated than late type satellite galaxies, which is qualitatively consistent with our result.

On the other hand, it is still in debate whether the surface brightness of galaxies depends on local density. Several studies found that low surface brightness galaxies have fewer neighboring galaxies on scales of $\lesssim 1$ Mpc to several Mpc (Bothun et al. 1993; Rosenbaum et al. 2009; Galaz et al. 2011). However, the "low surface brightness galaxies" in these studies refers to galaxies whose surface brightness are fainter than a certain value. We have discussed in Chapter 2 that this definition yields a heterogeneous sample. A galaxy with low surface brightness could be a result of an extended distribution of baryons, its less massive nature, or being massive but in a gas-rich (star-poor) condition. Each type of galaxies may have its own environmental dependence, and it is difficult to distinguish among the contribution from each type.

Rosenbaum et al. (2009) found that low surface brightness galaxies reside in underdense regions at scales $\gtrsim 2$ Mpc from SDSS DR 4 sample. In the same study, they further split the sample into two redshift bins and showed that this environmental dependence is more prominent in the low- z bin than in the high- z bin. As shown in Rosenbaum et al. (2009), their low- z low surface brightness sample consists mainly of dwarf galaxies, and the high- z low surface brightness sample is dominated by regular spirals. The behavior in two redshift bins may suggest that at least part of the apparent environmental effect is inherited from the luminosity, or mass, of the galaxy. On the contrary, Blanton et al. (2005) studied the relationship between environment and optical properties of galaxies in the SDSS and found a tentative trend that lower surface brightness galaxies are in the denser region for a given

luminosity. It is not clear whether the local density affects surface brightness from direct observations.

Assembly History

The discussion so far is under the assumption of constant Λ . This assumption has the physical motivation that inflow increases a gas reservoir, therefore, the capability of forming stars, but it is hard to verify observationally. Some observations of high-redshift massive galaxies ($1 < z < 3$) suggested $\Lambda > 1$ (Tacconi et al. 2010, 2013; Yabe et al. 2015), which is larger than what we derive for local galaxies ($\Lambda < 1$) therefore constitutes a challenge to our assumption of constant Λ . Nevertheless, it is not clear whether galaxies in different studies can be directly compared, i.e., our sample is not necessarily the descendant of galaxies in previous studies. Moreover, in spite of possible flaws in the assumption, this model has been shown to be able to reproduce the distribution of metallicity gradients of local galaxies (Ho et al. 2015). Practically, the metallicity is not sensitive to inflow and outflow in the gas-rich regime. Because metallicity is the content of metals normalized by the amount of gas, inflow and outflow would not drastically change it when the galaxy still possess a vast gas reservoir. Therefore, the model parameters, η and Λ , reflect the more recent accretion activities and less the early phase of galaxy formation. Although the assumption of constant η and Λ may not necessarily hold, we consider our fitting parameters should at least reflect the inflow and outflow properties at recent times.

If we assume that Λ is decreasing over time, as hinted by observations, the dependences on surface brightness we see from local galaxies are qualitatively consistent with the canonical view of halo formation. More compact galaxies are considered to reside in compact halos with lower spin which form relatively early (Jimenez et al. 1998; Mo et al. 1998). For baryons, hydrodynamic simulations showed that most baryons in low spin halos collapse into the center of the galaxies within the first ~ 1.5 Gyrs (Kim & Lee 2013), therefore implying low accretion at the present day.

Overall, galaxies with higher surface brightness have likely passed their peak accretion phase, while low mass, lower surface brightness galaxies are still assembling their baryons. The low Λ observed in the high mass bin could also result from the virial shocks developing in halos with $M_{halo} \gtrsim 10^{12} M_{\odot}$, which suppress cold material falling onto the galaxies (Kereš et al. 2005, 2009; Brooks et al. 2009). In this case, the mass is the dominant factor, and the surface brightness effect is relatively small and, therefore, not observed. Both factors could lower the accretion rate, \dot{M}_{accr} in high mass, high surface brightness galaxies.

3.5.2 Possible Systematics

Molecular gas content

In Section 3.3, we compare galaxies with the same stellar and gas mass, where molecular mass is estimated from a stellar-mass-dependent $M(H_2)/M(HI)$ fraction from Bothwell et al. (2014). Under this assumption, galaxies with the same stellar and HI mass will have the same amount of molecular gas. However, one could naturally expect that lower surface brightness galaxies have a deficit in molecular gas due to their lower metallicity so that the neutral gas will not be able to cool enough to form H_2 .

Detections of molecular gas in low surface brightness galaxies suggested that they have low $M(H_2)/M(HI)$ fraction compared to galaxies with higher surface brightness (O’Neil et al. 2003, 2004; Matthews et al. 2005; Das et al. 2006). As a result, our estimate could lead to systematic overestimate of total gas content in lower surface brightness galaxies.

Based on the result of Bothwell et al. (2014), the scatter of the $M(H_2)/M(HI)$ fraction around the mean value is ~ 0.4 dex for a given stellar mass. Some of the scatter are possibly inherited from the correlation with metallicity and surface brightness. According to Equation 3.1, the H_2 mass is less than 10% of HI at $M_* \lesssim 10^{10} M_{\odot}$. The 0.4 dex scatter corresponds to $\lesssim 25\%$, or $\lesssim 0.1$ dex, of total gas mass, and is negligible.

Of more concern is the high mass end, where $M_* \simeq 10^{11} M_{\odot}$. At this stellar mass, the average H_2 mass is comparable to HI mass, and the scatter in total gas mass is ~ 0.25 dex. To account for this possible systematic effect, we have allowed a 0.3 dex difference in mass

for galaxies to be considered as "the same mass" in Section 3.3. Moreover, for our chemical evolution model, we have run the test cases of different gas content in Section 3.4 and shown the result in Figure 3.6. Our discussion on Λ is not affected by changing the gas content within the nominal range. Especially at low mass, where the surface brightness effect is more prominent, the molecular gas content is essentially negligible.

Metallicity scale

In Section 3.4, we add a correction of 0.15 dex to the metallicities measured by Pilyugin et al. (2014). This correction has been found by Kudritzki et al. (2015) and is the result of a comparison of metallicities obtained from detailed quantitative spectroscopy of blue supergiant stars versus H II-region metallicities measured by Pilyugin et al. (2014). The yield ($y = 0.00313$) used in our chemical evolution model of section 4 has been empirically determined by Kudritzki et al. (2015) from the metallicity and metallicity gradient in the Milky Way disk as observed from Cepheids and B-stars. The yield and the metallicity scale used in Section 3.4 are, thus, consistently based on quantitative stellar spectroscopy.

The inflow and outflow strength determined in our model could be affected by systematic uncertainties of the metallicity scale used. To access this uncertainty we apply a similar procedure as Kudritzki et al. (2015) We repeat the analysis of Section 3.4, but this time replacing the 0.15 metallicity correction to Pilyugin et al. (2014) with metallicity corrections of 0.10, 0.05, and 0.00 dex, respectively. Figure 3.7 shows the effects from changes of the zero point. While the zero point is important in a quantitative sense (decreasing the metallicity leads to larger values of η and Λ), it does not affect our major conclusion. Lower surface brightness galaxies have higher Λ values than higher surface brightness galaxies of similar mass. In Figure 3.7 we only show the results for one type of gas profiles and only binned by baryonic mass corresponding to the case in Figure 3.6a. Application of the zero point shifts to the other cases lead to a similar conclusion.

We note that changing the zero-point of the metallicity scale is equivalent to changing the yield in the chemical evolution model, as can be seen in Equation 3.7. The result discussed here can also be seen as a test of the influence due to the uncertainty of the yield.

3.6 Summary

In this paper, we investigate whether the metallicity of galaxies depends on their surface brightnesses and discuss the possible origin of the dependence.

1. Previous studies found that, at given stellar mass, low surface brightness galaxies are more metal-poor. These studies used SDSS fiber spectra, where it is difficult to account for the aperture effect. We show that the result remains valid when the average metallicity of the whole galaxy is considered.
2. The surface brightness dependence still exists if the gas mass is also taken into account. For galaxies with similar stellar and gas masses, lower surface brightness systems tend to have lower metallicity.
3. We use chemical evolution models to constrain the inflow and outflow properties of galaxies. The ratio between accretion rate and star formation rate (Λ) is larger in low mass, lower surface brightness galaxies. The surface brightness effect is more prominent in low mass galaxies. On the other hand, the outflow property is not well constrained.
4. The high Λ in lower surface brightness galaxies can be directly interpreted as low star formation efficiency. This interpretation is consistent with the prevalent idea.
5. For galaxies with the same stellar mass, lower surface brightness galaxies should have more inflow material over time because of higher Λ , which is the ratio between mass accretion rate and star formation rate. This result indirectly suggests that lower surface brightness galaxies are more likely the central galaxy in a halo, therefore they have more inflow material.

6. If Λ is not constant in time as assumed in the model, the surface brightness dependence on Λ may be an indication of different accretion histories, where low mass, lower surface brightness galaxies are currently at their major accretion phase, while this phase in higher surface brightness galaxies has passed.

In the near future, large IFU surveys will provide maps of metallicity, and perhaps measurements of inflow and outflow activities, in a large number of galaxies spanning wide ranges of galaxy properties. We will understand better how galaxy structure affects the evolution of galaxies with the aid of IFU data.

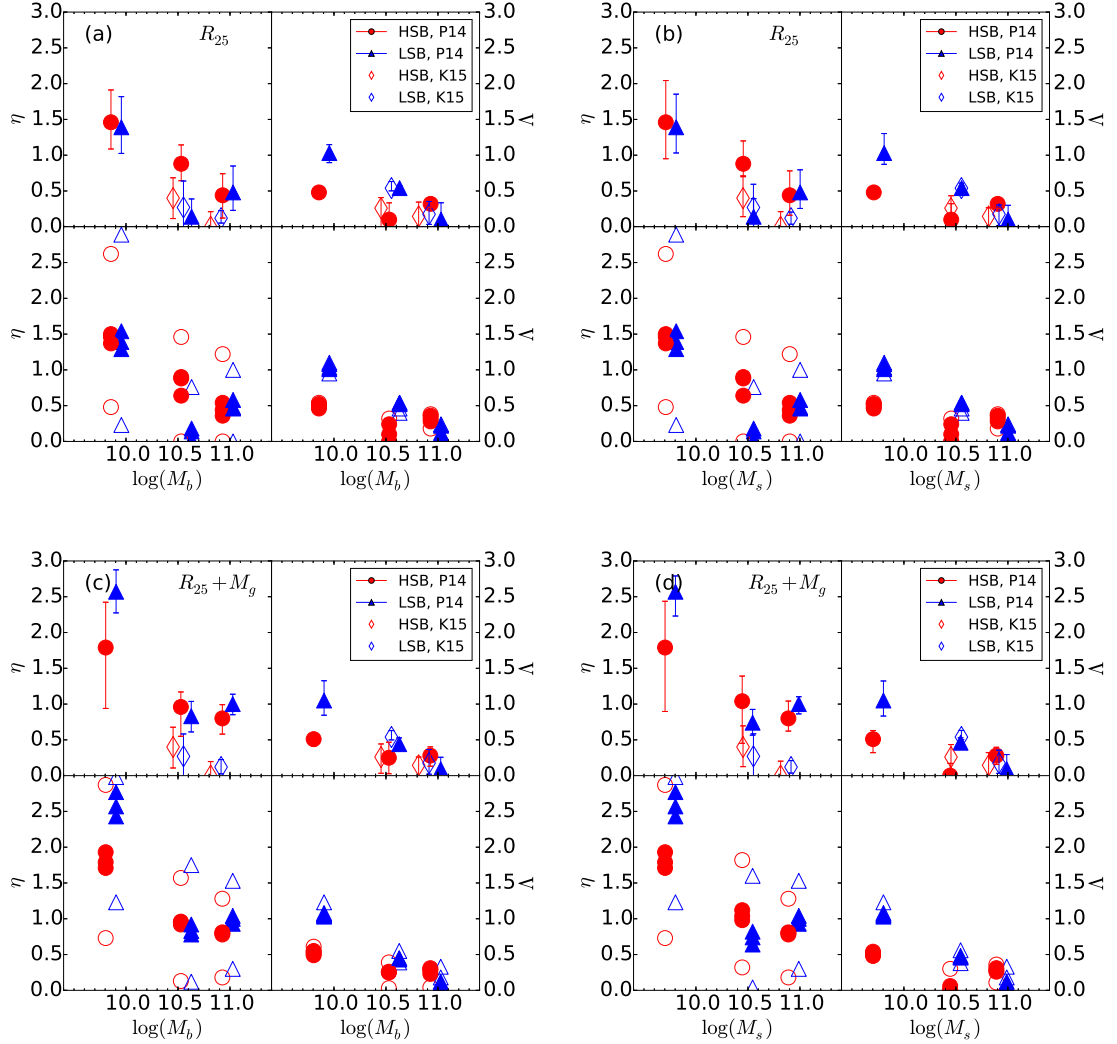


Figure 3.6 Best-fit η and Λ as a function of mass and surface brightness. (a): gas amount scaled by R_{25} , binned by baryonic mass. (b): gas amount scaled by R_{25} , binned by stellar mass. (c): gas amount scaled by R_{25} and measured gas mass, binned by baryonic mass. (d): gas amount scaled by R_{25} and measured gas mass, binned by stellar mass. Galaxies in the spectroscopic sample are first sorted into 3 mass bins then two surface brightness bins in each mass bin. Higher surface brightness galaxies are in red and lower surface brightness galaxies are in blue. In the upper panel of each subplot, the error bars represent for the 16th and 84th percentile of the distribution of η and Λ in each subsample. The filled symbols in the lower panel of each subplot show the uncertainties from varying the slope of surface density of gas. Open symbols illustrate the uncertainties from varying the gas amount (see Section 3.4). The 19 galaxies studied by Kudritzki et al. (2015) are also plotted as a comparison.

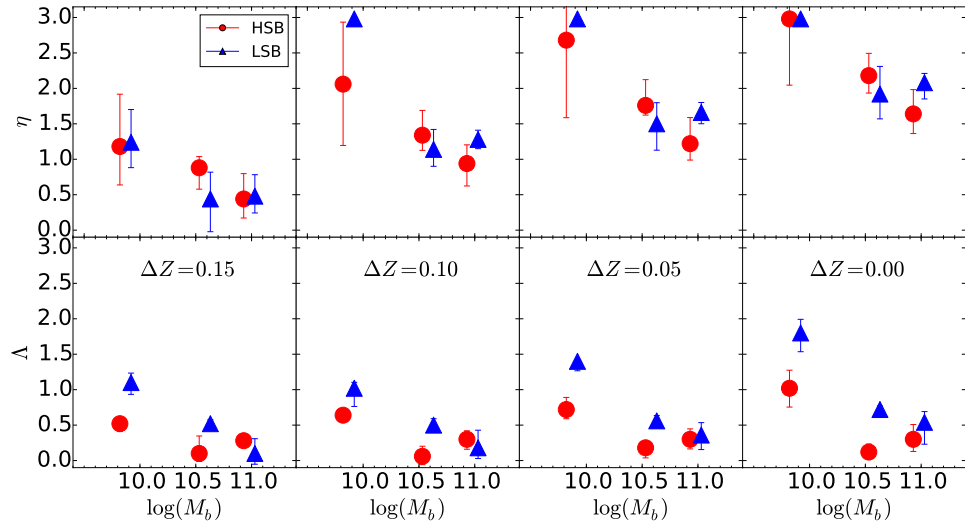


Figure 3.7 Test of the systematical effect from the zero point of metallicity scale on η and Λ . We adopt 4 different metallicity scales, adding 0.15 dex (the scale adopted for this work), 0.10, 0.05, and 0.00 dex to the metallicities of Pilyugin et al. (2014). Gas profiles are scaled by R_{25} as in Figure 3.6a. The zero point affects η and Λ in a quantitative sense, but not our conclusion, where lower surface brightness galaxies have higher Λ values than higher surface brightness galaxies of similar masses.

References

- Ascasibar, Y., Gavilán, M., Pinto, N., et al. 2015, MNRAS, 448, 2126
- Bigiel, F. & Blitz, L. 2012, ApJ, 756, 183
- Blanton, M. R., Eisenstein, D., Hogg, D. W., Schlegel, D. J., & Brinkmann, J. 2005, ApJ, 629, 143
- Boissier, S., Gil de Paz, A., Boselli, A., et al. 2007, ApJ, 681, 244
- Boselli, A., Cortese, L., Boquien, M., et al. 2014, A&A, 564, 66
- Bothwell, M. S., Maiolino, R., Kennicutt, R., et al. 2013, MNRAS, 433, 1425
- Bothwell, M. S., Wagg, J., Cicone, C., et al. 2014, MNRAS, 445, 2599
- Bothun, G. D., Schombert, J. M., Impey, C. D., Sprayberry, D., McGaugh, S. S. 1993, AJ, 106, 503
- Brooks, A. M., Governato, F., Quinn, T., Brook, C. B., & Wadsley, J. 2009, ApJ, 694, 396
- Bryant, J. J., Owers, M. S., Robotham, A. S. G., et al. 2015, MNRAS, 447, 2857
- Buat, V., Iglesias-Páramo, J., Seibert, M., et al. 2005 ApJ, 619, 51
- Bundy, K., Bershady, M. A., Law, D. R., et al. 2015, ApJ, 798, 7
- Burgarella, D., Buat, V., & Iglesias-Páramo, J. 2005, MNRAS, 360, 1413

Burkholder, V., Impey, C., & Sprayberry, D. 2001, *AJ*, 122, 2318

Cluver, M. E., Jarrett, T. H., Hopkins, A. M., et al. 2014, *ApJ*, 782, 90

Conroy, C. & Gunn, J. F. 2010, *ApJ*, 712, 833

Cortese, L., Boselli, A., Buat, V. et al. 2006, *ApJ*, 637, 242

Dalcanton, J. J. Spergel, D. N., Summers, F. J. 1997, *ApJ*, 482, 659

Das, M., O'Neil, K., Vogel, S. N., & McGaugh, S. 2006, *ApJ*, 651, 853

Dutton, A. A. & van den Bosch, F. C. 2012, *MNRAS*, 421, 608

Ellison, S. L., Patton, D. R., Simard, L., & McConnell, A. W. 2008, *ApJ*, 672, 107

Eminian, C., Kauffmann, G., Charlot, S., et al. 2008, *MNRAS*, 384, 930

Galaz, G., Dalcanton, J. J., Infante, L., & Treister, E. 2002, *AJ*, 124, 1360

Galaz, G., Herrera-Camus, R., Garcia-Lambas, D., & Padilla N. 2011, *ApJ*, 728, 74

Gallazzi, A., Charlot, S., Brinchmann, J., While, S. D. M., Tremonti, C. A. 2005, *MNRAS*, 362, 41

Ghosh, S., & Jog, C. J. 2014, *MNRAS*, 439, 929

Gil de Paz, A., Boissier, S., Madore, B. F., et al. 2007, *ApJS*, 173, 185

Hao, C., Kennicutt, R. C., Johnson, B. D. et al. 2011, *ApJ*, 741, 124

Haynes, M. P., Giovanelli, R., Martin, A., et al. 2011, *AJ*, 142, 170

Ho, I.-T., Kudritzki, R., Kewley, L. J., et al., 2015, *MNRAS*, 448, 2030

Hughes, T. M., Cortese, L., Boselli, A., Gavazzi, G., & Davis, J. I., 2013, *A&A*, 550, 115

Huang, S., Haynes, M. P., Giovanelli, R., & Brinchmann, J. 2012, *ApJ*, 756, 113

Impey, C. D., Sprayberry, D., Irwin, M. J., & Bothun, G. D. 1996, *ApJS*, 105, 209

Jimenez, R., Padoan, P., Matteucci, F., & Heavens, A. F. 1998, MNRAS, 123, 138

Kereš, D., Katz, N., Fardal, M., Davé, M., Weinberg, D. H. 2009, MNRAS, 395, 160

Kereš, D., Katz, N., Weinberg, D. H., & Davé, R. 2005, MNRAS, 363, 2

Kim, J. & Lee, J. 2013, MNRAS, 432, 1701

Kong, X., Charlot, S., Brinchmann, J., & Fall, S. M. 2004, MNRAS, 349, 769

Kudritzki, R.-P. Ho, I.-T., Schrubba, A., et al. 2015, MNRAS, 450, 342

Lara-López, M. A., Cepa, J., Bongiovanni, A., et al., 2010, A&A, 521, 35

Lee, H., Skillman, E. D., Cannon, J. M., et al. 2006, ApJ, 647, 970

Lee, H.-C., Worthey, G., Trager, S. C., & Faber, S. M. 2007, ApJ, 664, 215

Liang, Y. C., Zhong, G. H., Hammer, F., et al. 2010, MNRAS, 409, 213

Lilly, S. J., Carollo, C. M., Pipino, A., Renzini, A., Peng, Y. 2013, ApJ, 772, 119

MacArthur, L. M., Courteau, S., Bell, E., & Holtzman, J. A. 2004, ApJ, 152, 175

Mannucci, F., Cresi, G., Maiolino, R., Marconi, A., & Gnerucci, A. 2010, MNRAS, 408, 2115

Matthews, L. D., Gao, Y., Uson, J. M., & Combes, F. 2005, AJ, 129, 1849

Matthews, L. D., van Driel, W., & Monnier-Ragaigne, D. 2001, A&A, 365, 1

Mayer, L. & Wadsley, J. 2004, MNRAS, 347, 277

McDonald, M., Courteau, S., & Tully, R. B. 2009, MNRAS, 393, 628

Mihos, J. C., McGaugh, S. S., & de Blok, W. J. G. 1997, ApJ, 477, 79

Mo, H. J., Mao, S., & White, S. D. M. 1998, MNRAS, 319, 336

Mott, A., Spitoni, E., & Matteucci, F. 2013, MNRAS, 435, 2918

O'Neil, K., Bothun, G., van Driel, W., Monnier-Ragaigne, D. 2004, A&A, 428, 823

O'Neil, K., Oey, M. S., & Bothun, G. 2007, AJ, 134, 547

O'Neil, K., Schinnerer, E., & Hofner, P. 2003, ApJ, 588, 230

Pagel, B. E. J., & Patchett, B. E. 1975, MNRAS, 172, 13

Peeples, M. S., Shankar, F. 2011, MNRAS, 417, 2962

Pilyugin, L. S., Grebel, E. K., & Kinazev, A. Y. 2014, AJ, 147, 131

Pilkington, K., Gibson, B. K., Brook, C. B., et al. 2012, MNRAS, 425, 969

Rosenbaum, S. D., Krusch, E., Bomans, D. J., & Dettmar, R.-J. 2009, A&A, 504, 807

Salim, S., Lee, J. C., Chun, L., et al. 2014, ApJ, 797, 126

Salim, S., Rich, R. M., Charlot, S., et al. 2007, ApJS, 173, 267

Sánchez, S. F., Rosales-Ortega, F. F., Jungwiert, B., et al. 2013, A&A, 554, 58

Savaglio, S., Glazebrook, K., Le Borgne, D., et al. 2005, ApJ, 635, 260

Schlafly, E. F. & Finkbeiner, D. P. 2011, ApJ, 737, 103

Searle, L. & Sargent, W. L. W. 1972, ApJ, 173, 25

Spitoni, E., Calura, F., Matteucci, F., & Recchi, S. 2010, A&A, 514, 73

Tacconi, L. J., Genzel, R., Neri, R., et al. 2010, Nature, 463, 781

Tacconi, L. J., Neri, R., Genzel, R., et al. 2013, ApJ, 768,74

Toomre, A. 1964, ApJ, 139, 1217

Tremonti, C. A., Heckman, T. M., Kauffmann, G., et al. 2004, ApJ, 613, 898

Tully, R. B., Pierce, M. J., Huang, J., et al. 1998, AJ, 115, 2264

- Tully, R. B., Rizzi, I., Shaya, E. J., et al. 2009, AJ, 138, 323
- Verheijen, M. A. W., & Sancisi, R. 2001, A&A, 370, 765
- Weimann, S. M., Kauffmann, G., van den Bosch, F. C., et al. 2009, MNRAS, 394, 1213
- Wright, E., Eisenhardt, P. R. M., Mainzer, A. K. et al. 2010, AJ, 140, 1868
- Yabe, K., Ohta, K., Akiyama, M., et al. 2015, ApJ, 798, 45
- York, D., G., Adelman, J., Anderson, J. E., et al. 2000, AJ, 120, 1579
- Yuan, H. B., Liu, X. W., & Xiang, M. S. 2013, MNRAS, 430, 2188
- Zahid, H. J., Dima, G. I., Kewley, L. J., Erb, D. K., & Davé 2012, ApJ, 757, 54
- Zahid, H. J., Dima, G. I., Kudritzki, R., et al. 2014, ApJ, 791, 130

Chapter 4

Bimodal Surface Brightness Distribution of Galaxy Disks: Observational Evidence for Angular Momentum Transfer by Stellar Bars

4.1 Introduction

Theoretical and numerical works suggest that galaxy halos form wide ranges of initial mass and angular momenta (Warren et al. 1992; Catelan & Theuns 1996a,b; Cole & Lacy 1996; Steinmetz & Navarro 1999; Navarro & Steinmetz 2000). Baryons in dark halos cool and condense, eventually form rotational-supported disk galaxies. It is expected that galaxies we see today should also be distributed over a wide range of mass, and, at give mass, a wide range of surface density due to their different angular momentum content (Dalcanton et al. 1997; Mo et al. 1998). Thus, the observed distribution of galaxy surface brightnesses provides constraints on the initial conditions and evolutionary process of galaxies.

Freeman (1970) conducted one of the early observational investigations on the distribution of the surface brightnesses of galaxies and found that most galaxies have similar central surface brightnesses of their disks. This result was later found to be an artifact due to biased sample selection. Later, dedicated searches revealed a large population of galaxies with surface brightness much lower than the Freeman's value (Sprayberry et al.

1996; Impey et al. 1996; O’Neil & Bothun 2000), which is in better agreement with the theoretical expectation that galaxies of different surface brightness should exist.

An intriguing bimodal surface brightness distribution is found in the Ursa Major cluster (Tully & Verheijen 1997). The surface brightnesses of Ursa Major members distribute around two peaks with $\sim 2 \text{ mag arcsec}^{-2}$ separation and avoid intermediate surface brightnesses. Tully & Verheijen (1997) suspected that there are two dynamically stable states of disks galaxies. The center of galaxies with high surface brightnesses are dominated by baryons while low surface brightness galaxies are dark-matter-dominated for the entire galaxies. The galaxies in between may be transitional populations which are rearranging their baryons and evolving to the high surface brightness regime.

The Tully & Verheijen (1997) result is subject to a few uncertainties. First, the measurement of Tully & Verheijen (1997) depends on a subjective decision on the range where the disk is fit to the exponential profile (McDonald et al. 2009a). Moreover, the Ursa Major sample only contains 62 galaxies. The bimodality may be simply a result of unlucky statistics. There may also be an artifact due to incorrect extinction corrections applied to the measured surface brightness (Bell & de Blok 2000).

McDonald et al. (2009a) conducted an independent analysis of the Ursa Major cluster sample. They derived the surface brightness of disks from the 1-D bulge-disk composition method and found the bimodality still preserves. The bimodality also appears in a few later studies using sample sizes of a few hundred galaxies (McDonald et al. 2009b; Sorce et al. 2013, 2016), showing that the Tully & Verheijen (1997) result is not a statistical fluctuation. As to the issue of extinction correction, Sorce et al. (2013) showed that the bimodality also exists at the *Spitzer* $3.6\mu\text{m}$ band, a wavelength largely free from extinction. Therefore, the bimodal distribution is not an artifact related to extinction correction.

The existence of the surface brightness bimodal distribution has been presented in several independent studies, but there is still no satisfactory explanation for its origin. This double-peaked profile is not directly expected from hierarchical structure formation

models, assuming that angular momentum conserves and does not transport among galaxy components while the baryons are collapsing (Dalcanton et al. 1997).

However, it has been shown by analytical calculation and numerical simulation that disk stars can absorb or emit, thus exchange, energy and angular momentum (Lynden-Bell & Kalnajs 1972; Tremain & Weinberg 1984; Athanassoula 2002; Athanassoula 2013). The redistribution of angular momentum within galaxy disks lead to stellar migration and can alter the structure of the disk. Therefore, the overall distribution of the surface brightness of the disk does not necessarily follow the distribution predicted based on the mass and spin distributions of parent halos.

Theoretical works predict that the redistribution of angular momentum is most effective in galaxies with azimuthally asymmetric potential, such as spirals or stellar bars (Hohl 1971; Lynden-Bell & Kalnajs 1972; Athanassoula 2002; Athanassoula 2013). Secular evolution induced by stellar bars transports angular momentum to the outer part of the disk. As a result, the disk becomes more extended as it gains angular momentum. Meanwhile, a central mass concentration builds up because galaxy constituents lose angular momentum and fall into the galaxy center (Grosbøl et al. 2004; Athanassoula 2005).

Although this secular evolution of disk structure has been extensively tested and confirmed by numerical simulations (Hohl 1971; O’Neil & Dubinski 2003; Debattista et al. 2006; Minchev et al. 2011, 2012), it is difficult to confirm observationally simply because we cannot trace the evolution of a disk throughout its lifetime. As an alternative, examining the correlation between the internal structure of the galaxy and the size and the surface brightness of the disk may shed light on the angular momentum transport within galaxies, as well as the intriguing surface brightness distribution.

This paper consists of two parts. We will first show the bimodal distribution of the surface brightness from two galaxy samples with different selection criteria, and whose surface brightnesses are independently measured by two different methods. Second, we examine the correlation between the surface brightness and the internal structure of disk galaxies and provide a physical explanation for the origin of the surface brightness

bimodality. We introduce the data and our method in Section 2. The surface brightness distribution and the link to the internal structure are presented in Section 3. We discuss the implication in Section 4 and summarize the result in Section 5.

4.2 Data

We use two galaxy samples to show the bimodal distribution of the surface brightness (SB). The first sample is from the *Spitzer* Survey of Stellar Structure in Galaxies (S⁴G; Sheth et al. 2010). The S⁴G is a volume-, magnitude-, and size-limited ($|b| > 30^\circ$, $D < 40$ Mpc, $m_{Bcorr} < 15.5$, and $D_{25} > 1'$) survey of 2352 galaxies observed in the mid-infrared at 3.6 and 4.5 μm with the Infrared Array Camera (IRAC; Fazio et al. 2004) on the Spitzer Space Telescope (Werner et al. 2004). It covers a wide range of galaxy masses and morphological types thus provides a representative sample of nearby galaxies. The second sample is selected based on HI gas mass from the Arecibo Legacy Fast ALFA Survey (ALFALFA; Haynes et al. 2011). This sample is to supplement the lower surface brightness regime where the S⁴G is less complete.

The SB in this paper refers to μ_0 , the central SB of the disk. The SB profile of an exponential disk as a function of distance to the galaxy center is described as:

$$\mu(r) = \mu_0 \exp(-r/h), \quad (4.1)$$

where h is the scale length and μ_0 is the central SB of the disk.

We will also analyze the effect of internal structure on the surface brightness. We use the S⁴G multi-component structure decomposition (Salo et al. 2015, hereafter S15).

Table 4.1 Structural Classification

Name	Disk	Bar	Bulge	N
Pure disk	+	-	-	339
Barred-disk	+	+	-	336
Bulged-disk	+	-	+	580
Barred-bulged-disk	+	+	+	491
All				1746

4.2.1 The S4G sample

Sample selection and structural decomposition

The S4G collaboration has made a wealth of derived information publicly available. In this paper, we use the multi-component decomposition of the S4G Pipeline 4 (S15) to study the structure of galaxy disks.

S15 carried out the two-dimensional decomposition of the S4G $3.6\mu\text{m}$ images using the GALFIT software (Peng et al. 2002, 2010). Each galaxy is described as a combination of the following structural components: disk, bulge, bar, and nucleus, represented by different mathematical expressions. The decomposition is a human-guided process. We refer readers to S15 for the detailed process used to obtain the final best-fit model.

From the S4G survey, we select galaxies fulfilling the following criteria for our study. We first require the galaxy has the decomposition quality flags of 5 in the S15 catalog, where the values of disk scale length and surface brightness are reliable. We then select galaxies with at least one disk component with low or intermediate inclination. These galaxies have the model code **d**. We exclude near edge-on galaxies (apparent axis ratio $q \lesssim 0.2$, $i \gtrsim 80$ deg; S15) because a sub-component like a bar is difficult to be identified in these galaxies (Mosenkov et al. 2010). Last, we select galaxies with secured stellar mass measurement in the S4G catalog. The final sample contains 1746 galaxies.

We adopt the distance from Sheth et al. (2010) and stellar masses derived by S4G Pipeline 3 (Muñoz-Mateos et al. 2015).

Structural Classification

We classify our sample into four categories by their composite structure components, based on the best-fit model code of the S15 catalog. (1) Pure-disk galaxies are galaxies with model code **d**. These galaxies are best described as a single exponential disk. (2) Barred-galaxies are galaxies with model code **dbar**. These galaxies are best fit by an exponential disk plus a bar. (3) Bulged-galaxies are galaxies with at least one component other than disk but do not have a bar. (4) Bulge-barred-galaxies are galaxies have a disk, a bar, and at least one other component.

Here we define "bulge" in a loose way. Any excess component other than the disk and the bar is classified as "bulge". The excess component can be a "photometric bulge" (model code **b**), which is described by a Sérsic profile, an unresolved "nucleus" (**n**), another exponential disk (**d**), or a combination of the above.

Some galaxies are fit by two exponential disk components. In such cases, we adopt the SB and the scale length of the component with larger flux. Visually inspecting the 1D SB profiles and images of these galaxies assures that this simple selection is solid. For the majority of cases, the brighter disk is the dominant component, most representative the disk structure. The fainter exponential component may be the so-call pseudo-bulge, or correspond to the inner spiral structure. Only a few galaxies have two exponential disk components of similar strength, such that the choice is ambiguous. But they only consist of a negligible fraction of the whole sample thus do not affect our result.

In short, our structural classification is based on two criteria that lead to four categories: the existence of bar or not, and the existence of excess light other than the disk and the bar or not. Table 4.1 lists our classification and the number of galaxies in each category.

4.2.2 The WISE-ALFALFA sample

In Chapter 2, we described the selection of a magnitude-, size-, and distance-limit galaxy sample from the ALFALFA survey, and the measurement of their surface brightnesses and

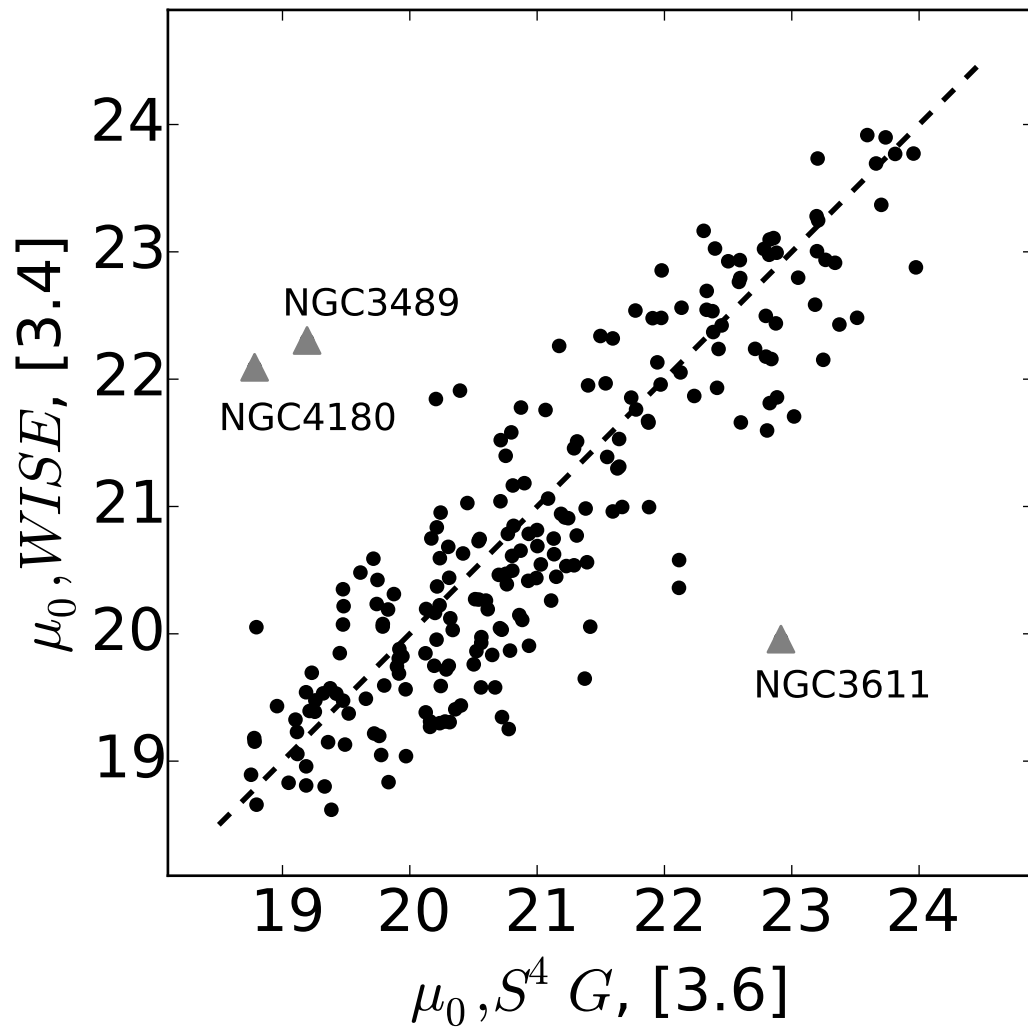


Figure 4.1 The comparison between the surface brightnesses measured by S15 and the procedure in this paper. The dashed line has a slope of 1.

stellar masses using WISE images. We use this sample in this Chapter to examine the surface brightness distribution of galaxies.

The surface brightness and the scale length of this WISE-ALFALFA sample is measured by modeling the exponential part of the SB profile. We show an example of the fitting in Figure 4.2. In this particular case, the galaxy contains both a bulge and a bar. These structures are not included in our disk fitting by setting an inner fitting range. This method is different from the S15, who simultaneously modeled the SB profile of the whole galaxy using multiple structural components.

We check whether these two methods yield consistent result by comparing the SB of 217 galaxies presenting in both the S⁴G and the WISE-ALFALFA sample. We plot in Figure 4.1 the SB measured by S15 in *Spitzer* 3.6 μ m and by our procedure in WISE 3.4 μ m. For a few galaxies, the SB measured by the two methods are significantly different (labeled as gray triangles in Figure 4.1). NGC 3611 is a galaxy with a big bulge. S15 measured a bulge fraction of 0.85 and the SB profile is dominated by the bulge for the most part of the galaxy. In this particular case, the range we fit for the disk profile is still bulge-dominated according to the decomposition of S15, so that we obtain a fit with higher SB and shorter scale length. The other two galaxies (NGC 3489, NGC 4180) are both classified as barred-bulged galaxies and both have up-bending SB profiles at their outskirts. In these two cases, we have manually adjusted the inner fitting range to avoid the prominent bar and bulge component in galaxy centers, and essentially fit the up-bending part of the SB profiles. The result is a broad and faint disk which consists of $\sim 15\%$ of total flux in either case. On the contrary, the S15 multi-component models disentangled the contribution from the bar and the disk and reproduced the overall SB profile well, but significantly underestimated the flux at the outskirts. The inconsistent result in these three cases is because the "disks" fit by the two methods are in fact different parts of the galaxies. The ambiguity in defining the "disk" may also affect the measurements of other galaxies but not as serious.

Comparing the measurements from the two methods, we find a small offset, $\langle \mu_{0,S4G} - \mu_{0,WISE} \rangle = 0.18$, with a scatter of ~ 0.6 mag. The scatter is similar to the value found by

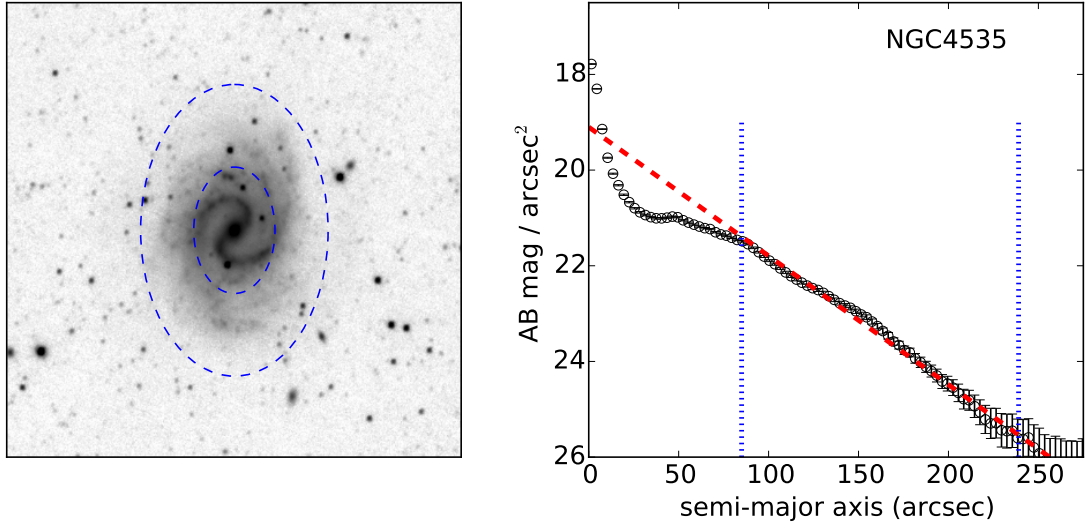


Figure 4.2 Example of the disk fitting for the WISE-ALFALFA sample. The left panel shows the image of NGC 4535. The right panel plots the surface brightness profile. The radial range for fitting is indicated by the two dashed ellipses in the left panel and two vertical dotted lines in the right panel. The best-fit is shown by the red dashed line. Our disk fitting is performed outside the effective radius, therefore, the bar and the bulge in the center of NGC 4535 is irrelevant.

previous studies comparing the SB measured with different methods (de Jong 1996; Sorce et al. 2016). We have also cross-checked the stellar masses measured by us from WISE and S15 from *Spitzer*. We find the stellar masses are statistically consistent between the two samples at ~ 0.1 dex level.

4.3 Result

4.3.1 The Distribution of Central Surface Brightness of Disks

Figure 4.3 shows the distributions of stellar masses and SBs of our samples. The WISE-ALFALFA sample exhibits a clear bimodal SB distribution, where a trough presents at $\mu_0 \simeq 21.5$ mag arcsec $^{-2}$ and two peaks at $\mu_0 \simeq 20.5$ mag arcsec $^{-2}$ and $\mu_0 \simeq 22.5$ mag arcsec $^{-2}$. This double-peaked distribution has been found in the Ursa Major cluster (Tully & Verheijen 1997) and the Virgo cluster (McDonald et al. 2009a). In addition, Sorce et al. (2013) also

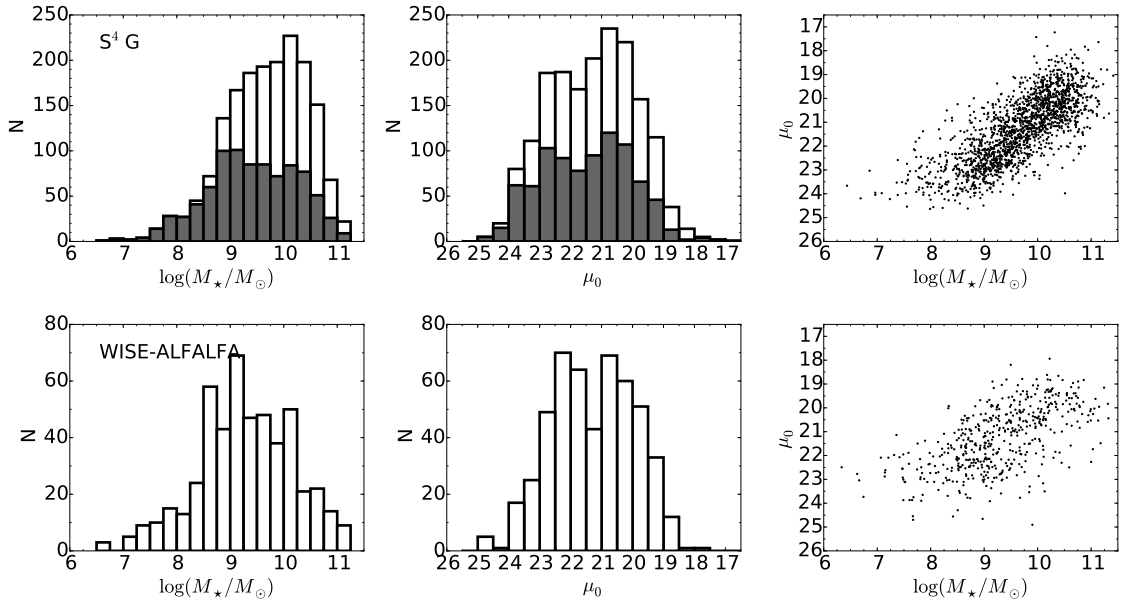


Figure 4.3 The stellar mass distribution, the surface brightness distribution and the surface brightness as a function of stellar mass. The gray histograms are the closest 50% of S⁴G galaxies ($D < 23.8$ Mpc). The surface brightness of the WISE-ALFALFA sample exhibits a clear bimodal distribution, with a trough at ~ 21.5 mag arcsec⁻². The trough of the whole S⁴G sample is shallower but at similar magnitude. The closest 50% of the S⁴G galaxies show a more prominent trough.

showed that the bimodality exhibits in a subset of S⁴G galaxies with consistent magnitudes of the trough and the peaks.

The full S⁴G sample shows only a tentative bimodality. In Figure 4.3 we also plot the distributions of the closest 50% of the S⁴G galaxies ($D < 23.8$ Mpc) as the gray histograms. This subset consists of fewer massive galaxies and has a clearer bimodal distribution. This subset is similar to the one examined by Sorce et al. (2013), who selected non-edge-on S⁴G galaxies with $D < 20$ Mpc. For a magnitude-limit sample like the S⁴G, galaxies at larger distances on average have higher stellar mass. Their SB distribution biases toward the high SB end and therefore washes out the bimodality. The bimodal distribution only shows up when the low-mass end is properly sampled.

The SB of the S⁴G sample in this paper and the SB presented by Sorce et al. (2013) are derived from two different methods. In Sorce et al. (2013), the SB is derived from fitting only the disk component of the 1D surface brightness profile, similar to the procedure we do for the WISE-ALFALFA sample. Sorce et al. (2013) fit the disk between the half-light radius and an isophotal radius at the galaxy outskirts. Structures at the galaxy center such as the bulge and the bar are excluded from the fitting process. On the other hand, the S⁴G SB presented in this paper is derived from the multi-component decomposition of 2D surface brightness profile. The bulge and the bar are expressed by different mathematical forms and fit together with the exponential disk component. Although different methods could lead to ~ 0.5 mag uncertainty in measuring the SB as pointed out by previous studies (de Jong 1996; Sorce et al. 2016) and our study in Figure 4.1, the bimodality persists regardless of the method used.

4.3.2 The structural dependence on the surface brightness

The SB is measured from stellar light. It is naturally to expect that higher mass galaxies will have higher SB. This positive correlation is clearly seen in Figure 4.3, but there is no bimodality in stellar mass. There must be other factors shaping the SB of galaxies disks, leading to the bimodal SB distribution.

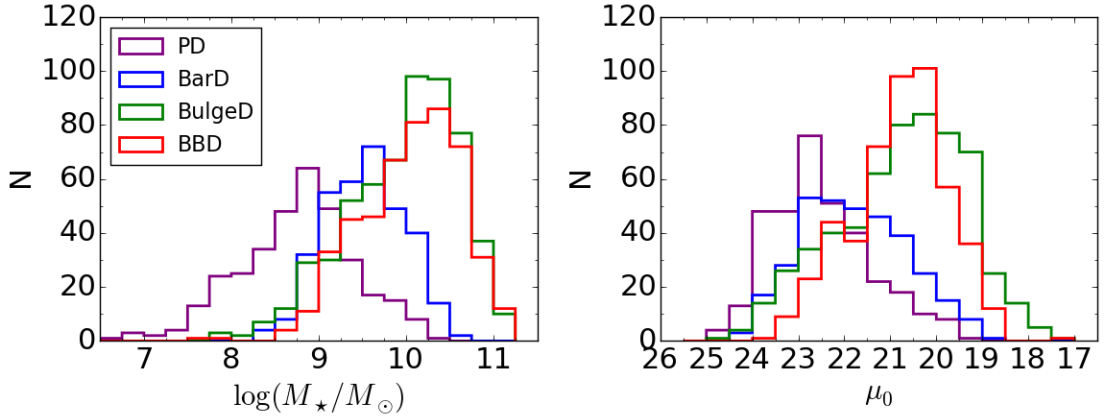


Figure 4.4 Stellar mass and μ_0 distribution, separated by galaxy structures. Pure-disk, barred-, bulged-, bar-bulged-galaxies are shown in purple, blue, green, and red histograms, respectively.

In our definition, the SB only relates to the structure of the disk component in a galaxy. Nevertheless, a disk-galaxy can consist of components other than a pure exponential disk. Figure 4.4 shows the stellar mass and SB distributions of the S⁴G sample of each structural type. First, we find that the structure of galaxies strongly correlates with stellar mass. At the low-mass end, many galaxies do not have component other than the exponential disk. On the other hand, high-mass galaxies mostly have bulges. Barred-galaxies without bulges distribute mainly at $9 \lesssim \log(M_*/M_\odot) \lesssim 10$, between the pure-disk galaxies and galaxies with bulges.

The SBs of different types of galaxies, in general, have the same trend as that of stellar mass. The pure-disk galaxy correlates with the lowest SB population. Galaxies with bulges have on average higher SB. Barred-galaxies without bulges reside in the middle. The pure-disk galaxies and the two types of bulged-galaxies peak at $\mu_0 \simeq 22.5$ and $\mu_0 \simeq 20.5$, respectively. These two peaks roughly correspond to the two peaks in the SB distribution of the whole sample. For barred-galaxies without bulges, the disk SB exhibits a broad distribution and skews toward the low-SB end, even though the overall stellar mass distribution has a clear peak. Next, we will examine the correlation between the stellar

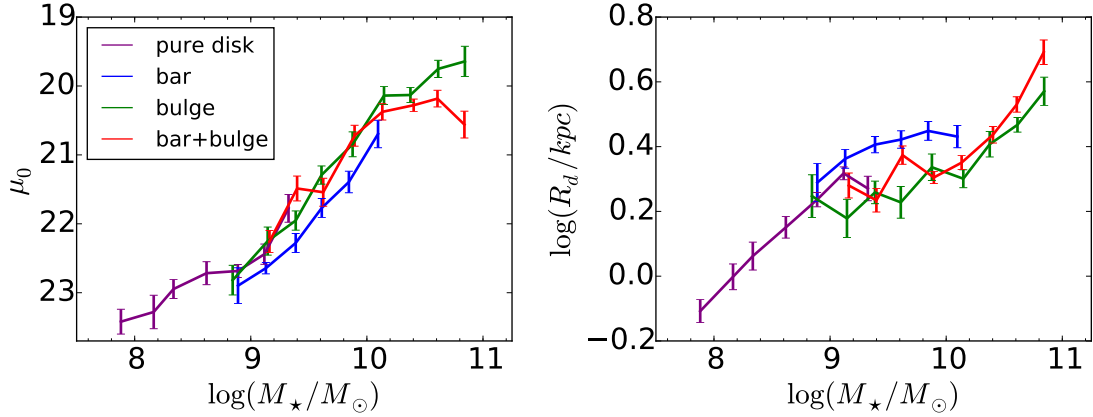


Figure 4.5 The median μ_0 and h as a function of stellar mass, distinguished by disk structure. Pure-disk, barred-, bulged-, bar-bulged-galaxies are shown in purple, blue, green, and red lines, respectively. Errors are derived from bootstrap resampling. For each subsample, we only plot the data if there are at least 20 galaxies in the 0.25 dex mass bin. The barred-galaxies on average have lower surface brightnesses and larger scale lengths than other types of galaxies.

mass and the SB of galaxies of each structural type. We have seen in Figure 4.3 that the SB and the stellar mass are correlated but with significant scatter at fixed stellar mass. Part of the scatter may be due to the internal structure of disk galaxies. Figure 4.5a shows the median μ_0 at fixed stellar mass for each type of disk. In general, galaxies of different structural types follow a similar μ_0 - M_* relation. However, at $9.5 \lesssim \log(M_*/M_\odot) \lesssim 10.0$, the SBs of barred-galaxies are lower than galaxies of other types by ~ 0.5 mag arcsec $^{-2}$.

Figure 4.5b shows the median scale length at fixed stellar mass for each type of disks. Disks in barred-galaxies have larger scale lengths than disks in other structural types. Figure 4.5a and b together demonstrate that barred-galaxies possess more extended stellar disks than other galaxies at fixed stellar mass.

We use the 217 galaxies present in both S⁴G and the WISE-ALFALFA sample to verify the robustness of the SB measured by S15 across different structural types of galaxies. We have seen in Section 4.2 that the two measurements are overall statistically consistent. We redo the analysis by separating galaxies with different structural types. For all four structural types, the average SB difference measured by the two methods, $\mu_{0,S4G} - \mu_{0,WISE}$,

are between 0.1 to 0.2 mag. The S15 measurements are robust against galaxies with different internal structures. The lower SB of barred-galaxies is unlikely an artifact from the multi-component decomposition method.

Figure 4.6 further illustrates the effect of bars. In each mass bin, we separate each of the barred-galaxy and bulged-barred-galaxy sample into two equal-size sub-samples by the physical lengths of bars, i.e., length in kpc. Example images of this classification are shown in Figure 4.7.

Figure 4.6 plots the SBs and scale lengths of each sub-sample as a function of stellar mass. For galaxies without a bulge (Figure 4.6a,c), long-barred galaxies on average have extended disks with low SBs and large scale lengths. On the contrary, disks in short-barred galaxies have comparable sized to those of pure-disk galaxies.

Figure 4.6g shows the ratio between the bar length and the disk scale length. Here we make sure that the long-barred galaxies are indeed "long" compared to the size of the disk. Therefore, the differences in SB and scale length between the short- and long-barred galaxies are not a result inherited from the disk size of each sub-sample.

Figure 4.6b and d plot the median SB and the median scale length of galaxies with bulges as a function of stellar mass. The same effect is as in galaxies without bulges, long-barred bulged-galaxies have on average lower SB and larger scale lengths than short-barred bulged-galaxies. For bulge-galaxies without bars, their SB appears to be closer to long-barred bulged-galaxies at low mass but approaches to short-barred bulged-galaxies at high mass.

In the next section, we will discuss the implication of these result, attributing it to be the consequence of bar-driven secular evolution.

4.4 Discussion

4.4.1 Bar formation transfers angular momentum

In Figure 4.6a and c, we find correlations between the length of the bar and the scale length and the SB of the galaxy disk. At fixed mass, galaxies with longer bars tend to have larger scale length and lower SB.

It is natural to first consider that whether low surface brightness, extended disks, are prone to bar formation. However, the weak self-gravity of these disks suggests that they are more stable against non-axisymmetric perturbations (Mihos et al. 1997). Numerical simulations also showed that bar formation is suppressed in low surface brightness galaxies mainly due to the diffused disk mass distribution (Mayer & Wadsley 2004; Ghosh & Jog 2014). It is unlikely that barred-galaxies are naturally more extended.

This leaves us the other possibility; the disk scale length increases along with bar formation. Theoretically, the bar can transfer the angular momentum from the inner parts to the outer parts (Lynden-Bell & Kalnajs 1972). During the process, the bar grows stronger and longer (Athanasoula 2003). The positive correlation between the bar length and bar strength has been found observationally (Block et al. 2004; Elmergreen et al. 2007; Díaz-García et al. 2015). Meanwhile, the angular momentum redistribution leads to considerable change of the radial mass profile, resulting in an increase of disk scale length. Several numerical simulations have demonstrated the growth of disk scale length along with bar-driven secular evolution (Hohl 1971; Debattista et al. 2006; Minchev et al. 2011, 2012).

The results in Figure 4.6 a and c are in good agreement with theoretical predictions. For galaxies with short bars, their disks have similar scale lengths compared to galaxies with no bars. At this stage, the bar is likely newly-formed and less evolved. The redistribution of angular momentum and material has not become significant enough to be detected. During the evolution, the bar becomes longer, and angular momenta are being transferred to the outer disk, leading to the larger scale length in long-barred galaxies (Figure 4.6c).

The barred-bulge galaxies show a similar evolutionary picture. Galaxies with long bars have lower SB than galaxies with short bars (Figure 4.6b and d). However, the behavior of bulged-galaxies without bars is intriguing. At high mass, ($M_{\star} \gtrsim 10^{10} M_{\odot}$), the SB of bulged-galaxies without bars are similar to that of short-barred bulged-galaxies. On the other hand, at low mass ($M_{\star} \lesssim 10^{9.5} M_{\odot}$), their SB are closer to that of long-barred galaxies.

To explain the behavior of bulged-galaxies, we should remind readers that the "bulge" in this paper is the photometric bulge, which refers to any excess light other than the disk and the bar component. The bulge component can be merger-built (classical bulge) or grow from secular evolution (pseudo bulge). The two types of bulged-galaxies would have different scale lengths due to their distinct evolutionary histories.

Here we discuss the two scenarios of a galaxy with a photometric bulge but without a bar. For a galaxy with a pseudo-bulge, it likely had experienced bar-driven secular evolution in the past. The bar destructs itself by building up the central mass concentration whose gravitational forces dilute the axis-asymmetric force (Athanasoula 2003). Therefore, although the bar was actively driving secular evolution in the past, no bar is observed today. Such a galaxy is at an even later stage than galaxies with long bars. On average, they would have even more extended disks. On the contrary, galaxies with merger-built, classical bulges may not have experienced secular evolution. In this case, we expect they would have higher SB. The difference in disk structures between galaxies holding two types of bulges has been suggested observationally. From ~ 1000 SDSS galaxies, Gadotti (2009) distinguished pseudo bulges from classical bulges based on the concentration of light profiles of bulges, such that pseudo bulges are less concentrated. Using this classification, Gadotti (2009) found that galaxies with pseudo bulges have on average more extended disks than galaxies with classical bulges at fixed mass.

Now we turn back to Figure 4.6b. It has been recognized that the prevalence of bulge and its type (pseudo or classical) depends on galaxy mass. Pseudo bulges are usually found in lower mass, while at high mass, classical bulges become the dominant population (Gadotti 2009; Fisher & Drory 2011). At $\log(M_{\star}/M_{\odot}) \simeq 9.5$, the bulged-galaxies have similar SB

to long-barred bulged-galaxies. This is consistent with the expectation that at this mass range, most bulges are pseudo-bulges. Therefore, bulged-galaxies at this mass range have larger disks. As the mass increases, the median SB of bulged-galaxies approaches that of short-barred bulged-galaxies. Again, this transition is in expectation if the bulges in high-mass galaxies are mostly classical bulges. Overall, the SB of galaxies with bulges fits in the picture that the bar-driven secular evolution induces outward migration of stars and lowers the SB.

Radial stellar migration has received observational support from individual galaxies. Some recent case studies found old stellar populations at the outskirts of galaxies (Radburn-Smith et al. 2012; Yoachim et al. 2012). Under the inside-out galaxy formation scenario, these findings are interpreted as observational support for stellar migration in disks; the old stellar population should have formed in the inner part of the galaxy but not at the outskirts. Their existence at the galaxy outskirts is evidence that they have been migrating outwards from their birthplaces. Nevertheless, from only a few cases, it is not clear whether this migration and the evolution of disk structure is prevalent, and what mechanisms induce the evolution. Our result is the first observational evidence to be able to demonstrate from a statistical sample that stellar migration is ubiquitous, and it is likely driven by bar formation which redistributes angular momentum and matter in galaxy disks. This mechanism can be further verified by coming spectroscopic integral field unit (IFU) galaxy surveys. With spectroscopy, it is possible to distinguish classical bulges from pseudo bulges by their kinematics, such that pseudo bulges have on average lower central velocity dispersions and higher ratios between rotational velocities and velocity dispersion (Fabricius et al. 2012; Méndez-Abreu et al. 2014).

4.4.2 The Surface Brightness Distribution

It has been almost 20 years since the bimodal distribution of SB was first reported. However, the significance and the cause of the bimodality has remained obscured. In this section, we discuss whether the bimodality exists and its possible origin.

The existence of the bimodality

The bimodal distribution of SB is first found in the Ursa Major loose association of galaxies by Tully & Verheijen (1997), then subsequently identified in both high-density region (the Virgo cluster; McDonald et al. 2009b) and in the field. Sorce et al. (2013) has shown that the bimodal distribution in the S⁴G galaxies is unlikely to be created from statistical fluctuation. In this paper, we further demonstrate the SB bimodal distribution from an independent sample. The bimodality appears to be prevalent in the local Universe.

Nevertheless, the same distribution is not reported by large imaging surveys such as SDSS. This can be simply due to a selection effect. Galaxies with low SB are highly selected against in most redshift surveys. Because of their low masses and low intrinsic luminosities, they quickly drop below the apparent magnitude cutoff of surveys as distance increases. Their diffuse light distribution also makes the detection more challenging.

The selection biased has been shown in Figure 4.3 with the S⁴G sample. At farther distances, only more massive galaxies are included because of the essential magnitude limit and the size limit in order to measure the light profile. So far, the bimodality is exclusively seen in distance-limit samples. The Ursa Major cluster and the Virgo cluster are nearby ($D \simeq 17$ Mpc) and all member galaxies are essentially at the same distance. Both samples examined in this paper have distance limits of $D \lesssim 40$ Mpc. Within the confined distance range, the bias toward high-mass galaxies is mitigated and the bimodal SB distribution is still preserved. On the contrary, if a galaxy sample is only magnitude-limited but not distance-limited, it will pick up only massive, high SB galaxies at a larger distance. As a result, the SB distribution is distorted and the bimodality will not be observed.

The origin of the bimodality

Motivated by the shapes of the rotation curves, Tully & Verheijen (1997) hypothesized that the bimodality represents for two dynamically stable configurations. Low SB galaxies have slow-rising rotation curves, while high SB galaxies have rotation curves that rise to their maximum circular velocities within two disk scale length. The low SB galaxies

are rotational-supported by the dark matter halos at all radii, while with the high SB galaxies, baryons have condensed toward the center and formed dynamically important disks. Galaxies avoid staying in a status where the dark matter and baryons have equal weights toward the center.

To test this hypothesis, we require rotation curves to model the radial distributions of baryons and dark matter of a proper galaxy sample. The sample should cover wide mass and SB ranges and contain a sufficient number of galaxies. Currently, there are only a limited number of HI interferometric observations for low SB galaxies (see the LITTLE THINGS survey, the VLT-ANGST survey, and the SHIELD survey; Hunter et al. 2012; Ott et al. 2012; Cannon et al. 2011). A recent work by Lelli et al. (2013) has attempted to quantify the correlation between the SBs and the gravitational potential wells at the centers of galaxies. From literature, Lelli et al. (2013) collected 47 high quality rotation curves that quantify gradients of circular velocities at galaxy centers. Beyond the qualitative description that lower SB galaxies have slow-rising rotation curve, they found a tight linear correlation between the log of the circular velocity gradient and the SB. This result implies a close link between the dark matter content, baryonic mass-to-light ratio, and SB in galaxy centers.

McDonald et al. (2009b) examined the correlation between the SB and other physical properties of galaxies including colors and structural parameters. They did not find the SB bimodality correlating with other physical parameters of galaxies. As for the environment, Sorce et al. (2016) found galaxies with intermediate SBs are slightly less abundant in filaments and sheets of the large-scale structure. Sorce et al. (2016) argued in line with Tully & Verheijen (1997) that galaxies with intermediate SBs are transitional populations so that they cannot form in regions without sufficient interactions like voids and cannot survive in regions with too many interactions like clusters.

In this paper, we find the bar-driven matter redistribution provides another plausible explanation. We argued in Section 4.1 that bar formation decreases the SB of a galaxy disk. For a galaxy which has a developing bar, the SB as a function of time will depend on both star-formation rate and the strength of the bar-driven matter redistribution. Since

the latter is poorly constrained by either simulation or observation, it is impossible to give a quantitative estimate. Qualitatively, the combined effect is that once the bar starts forming, the SB of the galaxy increases at a slower pace because the disk is gaining angular momentum and becoming more extended. The consequence is an observable over-abundance near the SB where bar starts to grow.

In Figure 4.4, we see the bar starts to grow mostly in galaxies with $\log(M_*/M_\odot) \gtrsim 9.0$. This stellar mass corresponds to $\mu_0 \simeq 22.5 \text{ mag arcsec}^{-2}$ (Figure 4.5). This SB is in broad agreement with the low SB peak of the distribution. For the high SB peak, it corresponds to the well-known "Freeman value". Disks above the Freeman value are rare because these disks are strongly self-gravitating therefore unstable (Dalcanton et al. 1997). Galaxy disks evolve from low to high SB ultimately halt at the SB around the Freeman value, thus creating the high SB peak.

4.5 Summary

In this paper, we examine the distribution of the central surface brightness of galaxy disks and the correlation between the surface brightness and the internal structure of galaxies. We have the following results.

1. We confirm the bimodal distribution. The bimodality presents in two independent samples of field galaxies whose SBs are derived by two different methods.
2. The bimodality is more significant when the galaxy sample is limited within a narrower distance range and achieves completion to more low mass galaxies.
3. We find galaxies with bars but without bulges have on average lower SB and larger scale length than galaxies of other structural types.
4. The bar length and the SB are anti-correlated. For barred-galaxies without bulges, galaxies with longer bars have lower SB and larger scale length. We find the same result on bulged galaxies.

From these results, we have the following conclusions.

1. The bar-driven secular evolution redistributes material within disk galaxies. As the bar evolves, galaxy disks become more extended and have lowered SB. Our result is the first observational evidence supporting the theory of bar-driven radial stellar migration from a statistical sample.
2. Magnitude-limit galaxy samples bias strongly against low SB galaxies thus distort the SB distribution. In such galaxy samples, the SB bimodality is washed out by over-sampling the high SB end of the distribution.
3. Galaxies with $\log(M_*/M_\odot) \gtrsim 9$ and $\mu_0 \lesssim 22.5$ mag arcsec⁻² start to form bars and their SBs increase slower because the redistribution of angular momentum and material within the galaxy. The low SB peak is thus created around $\mu_0 \simeq 22.5$ mag arcsec⁻², where the bar starts forming. The high SB peak corresponds to the Freeman value, where galaxy disks with denser SB are strongly self-gravitating thus hard to maintain rotational-supported.

Coming IFU surveys will provide spatially-resolve spectra of a large number of galaxies. The kinematics, stellar age and metallicity profiles derived from the spectra should provide profound insights into the effects of secular evolution on galaxy structure.

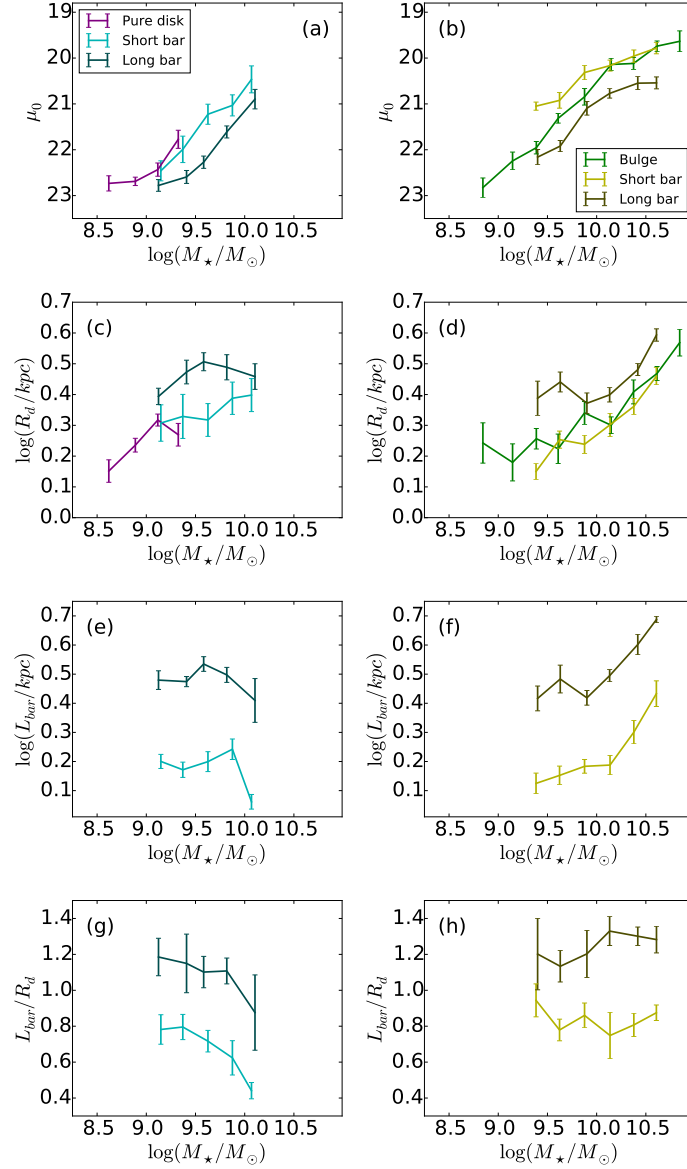


Figure 4.6 The effect of the bar on disk surface brightness and scale length. We show galaxies without (left column) and with (right column) bulges separately. In each mass bin, we separate galaxies into 3 subsamples by the physical length of the bar: no bar, short bar, long bar. Therefore, the bar length is compared with other galaxies of similar mass. *First row*: disk surface brightness. *Second row*: disk scale length. *Third row*: the bar length in kpc. *Four row*: the ratio between bar length and disk scale length. The median and the error are derived from bootstrap resampling. We only show data derived from at least 20 galaxies in each 0.25 dex mass bin for each subsample.

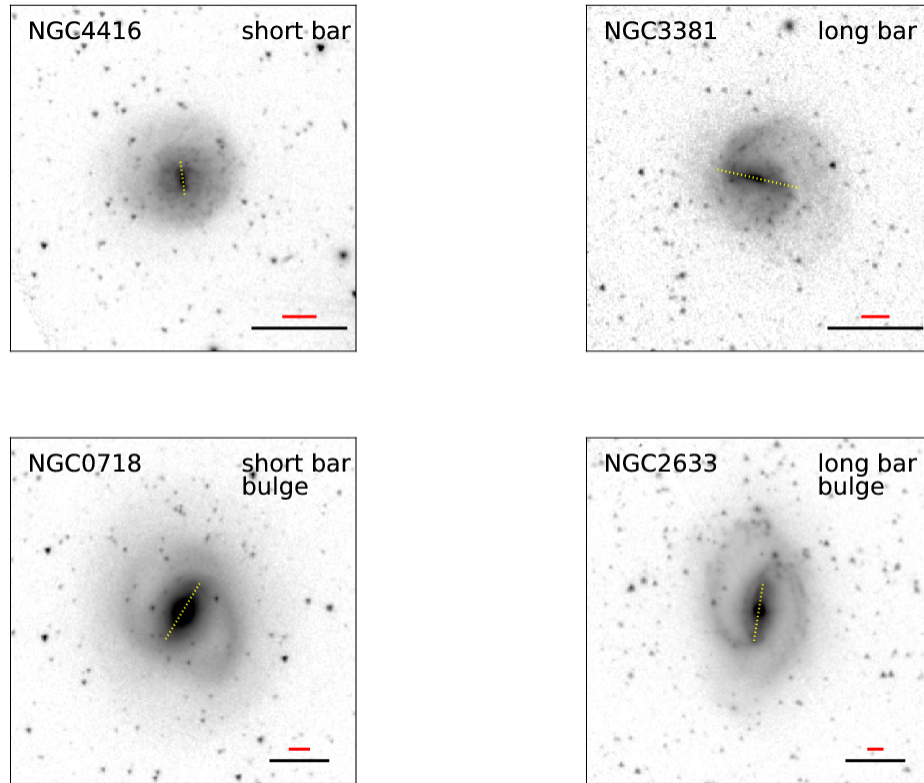


Figure 4.7 Cutout images of galaxies with different bar lengths. In the top row we show two galaxies without bulge of similar stellar mass, while in the bottom row the two galaxies with bulges. The left column shows galaxies categorized as having a "short bar", while the right column are examples for "long bar". The red and black lines represent 1 kpc and 1', respectively. The yellow dotted lines shows the lengths and the position angles of the bars from S15

References

- Athanassoula, E. 2002, *ApJ*, 569, 83
- Athanassoula, E. 2003, *MNRAS*, 341, 1179
- Athanassoula, E. 2005, *MNRAS*, 358, 1477
- Athanassoula, E. 2013, in “Secular Evolution of Galaxies”, J. Falcón-Barroso and J. Knapen (eds.), Cambridge University Press, Cambridge, 305
- Bell, E. F., de Blok, W. J. G. 2000, *MNRAS*, 311, 668
- Block, D. L., Buta, R., Knapen, J. H., et al. 2004, *AJ*, 128, 183
- Bothun, G., Impey, C., McGaugh, S. 1997, *PASP*, 109, 745
- Catelan, P., Theun, T. 1996a, *MNRAS*, 282, 436
- Catelan, P., Theun, T. 1996b, *MNRAS*, 282, 455
- Cannon, J. M., Giovanelli, R., Haynes, M. P. et al. 2011, *ApJ*, 739, 22
- Cluver, M. E., Jarrett, T. H., Hopkins, A. M., et al. 2014, *ApJ*, 782, 90
- Cole, S., Lacey, C. 1996, *MNRAS*, 281, 716
- Dalcanton, J. J., Spergel, D. N. m Summers, F. J. et al. 1997, *ApJ*, 482, 659
- Debattista, V. P., Mayer, L., Carollo, C. M., et al. 645, 209

de Jong, R. S., 1996, A&AS, 118, 557

D'iaz-García, S., Salo, H., Laurikainen, E., & Herrera-Endoqui, M. 2015, arXiv 1509.06743

Eliche-Moral, M. C., González-García, A. c., Alfonso, J., et al. 2013, A&A, 552, 67

Elmergreen, B. G., Elmergreen, D. M., Knapen, J. H., et al. 2007, ApJ, 670, 97

Erwin, P., Saglia, R. P., Fabricius, M., et al. 2015, MNRAS, 446, 4039

Fabricius, M. H., Saglia, R. P., Fisher, D. B., et al. 2012, ApJ, 754, 67

Fazio G. G., Hora, J. L., Allen, L. E., et al. 2004, ApJ, 154, 10

Freeman, K. C. 1970, ApJ, 160, 811

Fisher, D. B. & Drory, N. 2011, ApJ, 733, 47

Ghosh, S., Jog, C. J. 2014, MNRAS, 439, 929

Gadotti, D. A. 2009, MNRAS, 393, 1531

Grosbøl, P., Patsis, P. A., Pompei, E. 2004, A&A423, 849

Haynes, M. P., Giovanelli, R., Martin, A., et al. 2011, AJ, 142, 170

Hohl, F. 1971, ApJ, 168, 343

Hunter, D A., Ficut-Vicas, D., Ashley, T., et al. 2012, AJ, 144, 5

Impey, C. D., Sprayberry, D., Irwin, M. J., & Bothun, G. D. 1996, ApJS, 105, 209

Laurikainen, E., Salo, H., Buta, R., & Knapen, J. H. 2007, MNRAS, 381, 401

Lelli, F., Fraternali, F., Verheijen, M. 2013, MNRAS, 433, 30

Lynden-Bell, D. & Kalnajs, A. J. 1972, MNRAS, 157, 1

Macció, A. V.,

Mayer, L. & Wadsely, J. 2004, MNRAS, 347, 277

McDonald, M., Courteau, S., & Tully, R. B. 2009, MNRAS, 393, 628

McDonald, M., Courteau, S., & Tully, R. B. 2009, MNRAS, 394, 2022

Méndez-Abreu, J., Debattista, V. P., Corsini, E. M., Aguerri, J. A. L. 2014, A&A, 572, 25

Mihos, J. C., McGaugh, S. S., & de Blok, W. J. G. 1997, ApJ, 477, 79

Minchev, I., Famaey, B., Combes, F., et al. 2011, A&A, 527, 147

Minchev, I., Famaey, B., Quillen, A. C., et al. 2012, A&A, 548, 126

Mo, H. J., Mao, S., White, S. D. M. 1998, MNRAS, 295, 319

Mosenkov, A. V., Sotnikova, N. Y., & Reshetnikov, V. P. 2010, MNRAS, 401, 559

Muñoz-Mateos, J. C., Sheth, K., Gil de Paz, A., et al. 2013, ApJ, 771, 59

Muñoz-Mateos, J. C., Sheth, K., Regan, M., et al. 2015, ApJS, 219, 3

Naab, T. & Trujillo, I. 2006, MNRAS, 369, 625

Navarro, J. F., Steinmetz, M. 2000, ApJ, 538, 477

O’Neil, K., & Bothun, G., ApJ, 529, 811

O’Neill, J. K., Dubinski, J. 2003, MNRAS, 346, 251

Ott, J. S., Warren, A. M., Skillman, S. R., et al. 2012, AJ, 144, 123

Peng, C., Ho, L., Impey, C., & Rix, H. 2002, AJ, 124, 266

Peng, C., Ho, L., Impey, C., & Rix, H. 2010, AJ, 139, 2097

Radburn-Smith, D. J., Roškar, R., Debattista, V. P. et al. 2012, ApJ, 753, 138

Salo, H., Laurikainen, E., Laine, J., et al. 2015, ApJS, 219, 4

Shaw, L. D., Weller, J., Ostriker, J. P., & Bode, P. 2006, *ApJ*, 646, 815

Sheth, K., Regan, M., Hinz, J. L., et al. 2010, *PASP*, 122, 1397

Sorce, J. G., Coutois, H. M., Sheth, K., Tully, R. B. 2013, *MNRAS*, 433, 751

Sorce, J. G., Creasey, P., Libeskind, N. I. 2016, *MNRAS*, 455, 2644

Sprayberry, D., Impey, C. D., Irwin, M. J. 1996, *ApJ*, 463, 535

Steinmetz, M., Navarro, J. F. 1999, *ApJ*, 513, 555

Stewart, K. R., Bullock, J. S., Wechsler, R. H., Maller, A. H., & Zentner, A. R.

Tremaine, S., & Weinberg, M. D. 1984, *MNRAS*, 209, 729

Tully, R. B., Rizzi, I., Shaya, E. J., et al. 2009, *AJ*, 138, 323

Tully, R. B., Verheijen, M. A. W. 1997, *ApJ*, 484, 145

Warren, M. S., Quinn, P. J., Salmon, J. K., Zurek, W. H. 1992, *ApJ*, 399, 405

Werner, M. W., Roellig, T. L., Low, F. J., et al. 2004, *ApJS*, 154, 1

Wu, P.-F., Kudritzki, R., Tully, R. B., Neill, J. D., 2015, *ApJ*, 810, 151

Yoachim, P., Roškar, R., & Debattista, V. P. 2012, *ApJ*, 752, 97

Chapter 5

Summary and future outlook

5.1 Dissertation Summary

In the standard hierarchical structure formation model, dark matter halos form with a wide range of mass and angular momentum. As a result, galaxies forming in dark halos exhibit wide ranges of mass and surface brightness. Exploring the full range of galaxy characteristics in both mass and the surface brightness is essential to the full understanding of galaxy formation and evolution.

Compared to the mass of galaxies, studies on the effect of surface brightness are relatively incomplete and subject to various biases. The goals of this dissertation are to explore the effect of surface brightness of galaxy disks on galaxy evolution, especially toward the low surface brightness end of the distribution.

The astronomical society has benefited from a prodigious volume of public data covering a wide spectral range. With a large sample size, we are able to access the average properties of galaxies in the Universe, not strongly affected by variations among individuals. The approach of this research is to use archival data to establish a statistical view of the effect of surface brightness of galaxy disks on their evolution. By doing so, this study aims at shedding light on the effect of angular momentum on galaxy evolution. Below I highlight key results from this dissertation research.

5.1.1 The SB dependence on galaxy properties

The importance of SB on galaxy evolution has been recognized by early extragalactic studies. The majority of previous studies often defined samples of galaxies with lower SB and compare their physical properties with "normal", higher SB galaxies. However, this approach is fundamentally flawed in that SB and stellar mass are strongly correlated. Low SB galaxies are on average also low mass galaxies. It is not clear which one of mass or SB is the main driver for the different properties observed between the low and the high SB galaxies.

In Chapter 2, I present a sample of 501 disk galaxies selected from the ALFALFA survey. Their multi-wavelength photometry and physical properties (SB, stellar mass, gas mass, and SFR) were derived from public survey data (GALEX, SDSS, and WISE), yielding a homogeneous data set to investigate the effect of stellar mass and SB.

The data show that the observed SB dependence on galaxy properties are largely driven by the correlation between the SB and the stellar mass. After taking away the mass dependence, the SB appears to affect some, but not all, properties of galaxies. At fixed stellar mass, lower SB galaxies have bluer NIR colors and larger H I mass, which are in agreement with general consensus. However, at fixed stellar mass, the median optical color and SFR are nearly independent of the SB. This is inconsistent with many previous studies which claimed bluer optical colors and lower SFR for lower SB galaxies. We conclude that at fixed mass, low SB galaxies are metal-poor and inefficient in turning their gas into stars. The result presented in Chapter 2 demonstrates the necessity to decouple the effect of the mass from the effect of surface brightness.

5.1.2 The influence of surface brightness on the mass-metallicity relation

The correlation between the metallicity and stellar mass, the so-called mass-metallicity relation, is well known. Chapter 2 has shown that the NIR color is SB-dependent, which is interpreted as a result of SB-dependent stellar metallicity. The interpretation is consistent with the size dependence on the gas-phase metallicity, where larger galaxies have lower

gas-phase metallicity at fixed stellar mass (Ellison et al. 2009). However, there is still a lack of physical explanations on how the surface brightness affects the chemical abundance of galaxies.

In Chapter 3, I first show that the lower metallicity in low SB galaxies cannot be fully accounted for by their large gas reservoir. Therefore, the gas flows must be correlated with the SB in order to explain the SB dependence on metallicity. I combine chemical evolution models and the observed mass and metallicity profiles of 118 galaxies to constrain their inflow and outflow properties. I find that lower SB galaxies on average have stronger inflow rates relative to star-formation rates in order to account for the observed metallicity profile. The work in Chapter 3 demonstrates a new method to link the galaxy structure, metallicity, and gas flow.

5.1.3 The bimodal surface brightness distribution

Chapter 4 examines the SB distributions of two independent samples whose SB are derived from two different methods. A SB bimodality is present in both cases, regardless of sample selection and the methods used for measuring the SB. Therefore, we confirmed the existence of a bimodality in the SB distribution. The bimodality is more significant in samples with a proper distance limit. Magnitude-limit galaxy samples are strongly biased toward high SB galaxies and distort the SB distribution, such that the intrinsic bimodality is washed out.

We find the SB at fixed stellar mass depends on the structure of galaxies. Galaxies with bars are on average more extended and have lower SB than galaxies without bars. Furthermore, at fixed stellar mass, galaxies with longer bars have on average more extended disks than galaxies with shorter bars. This is the first observational support from a statistical sample for the theory that stellar bars can redistribute angular momentum in galaxies and make galaxy disks larger.

The intriguing SB bimodality can be explained as a result of stellar migration induced by this angular momentum redistribution during bar formation. The low SB peak corresponds to the mass and SB where bars start to develop. When a bar forms, the angular momentum

transfers from inner to outer disk, the disk becomes more extended and the SB increases slower as the galaxy grows in stellar mass. The high SB peak corresponds to the Freeman value. Galaxy disks with SB higher than this value are unstable.

5.2 Future Prospect

This dissertation research uses publicly available data to provide a statistical view of the effect of the SB on galaxy evolution. This type of work would not be possible for individual researchers who collect their own data. Part of observational astronomy is shifting into the big data era. The ongoing or planned larger survey projects will have high impacts on various fields of astronomy. In this section, I discuss possible future developments on the investigation of galaxy SB with current and coming large survey projects.

5.2.1 Complete the low surface brightness end of the distribution

With modern observing facilities, imaging a low SB galaxy is not a challenging task, under the premise that we know the position of the target. Objects of g' -band SB $\mu_{0,g} \sim 25$ mag arcsec⁻² are seen in images with several minutes exposure using a medium-size telescope (van Dokkum et al. 2015). The real challenging issue is that we do not know where they are, and where to point our telescopes. Moreover, even when deep images of arbitrary fields are obtained, searching for low SB objects in the image without knowing their positions in advance can still be difficult because their diffused emission is highly embedded in night sky background emission.

This dissertation research circumvents these problems by finding low SB galaxies by their H I 21 cm emission. Many low SB, low mass galaxies are expected to be gas-rich, therefore, easier to be detected in the H I 21 cm line emission. In Chapter 4, we demonstrate that this method effectively picks up galaxies with SB lower than optically-selected galaxy samples.

Chapter 4 uses the ALFALFA $\alpha.40$ data set, which contains the results of 40% of the ALFALFA survey released at the time of this dissertation research began. The newest

ALFALFA data release, the $\alpha.100$ "A grids" data set contains the full area of the survey (7,000 deg²) out to $v < 3,200\text{km s}^{-1}$. Using the same method in Chapter 4, the sample size will increase by 2.5 times.

This dissertation research uses the WISE survey as the primary source for measuring a surface brightness profile. The all-sky WISE survey ensures that every source detected by ALFALFA is covered. However, a drawback of the WISE satellite is its small aperture size, thus, poor angular resolution. The 6" angular resolution is ~ 3 times worse than the typical angular resolution of ground-based optical images. The SB profiles of galaxies with small angular extents are not well resolved. In Chapter 4, the size limit on the sample selection is inherited from this issue. The poor angular resolution limits our ability to probe the faint end of the SB distribution because low mass, low SB galaxies are intrinsically smaller in size.

Currently, the Pan-Starrs (Kaiser et al. 2010) survey has completed its 3π survey, which covers the whole northern hemisphere visible from the telescope site at optical wavelengths. Galaxies with small angular extend can be better resolved by Pan-Starrs images than WISE images, thus, better recover the faint end of the SB distribution. At optical wavelengths, the effects of internal extinction on measuring galaxy structures has to be considered, but the effect is likely insignificant for lower surface brightness galaxies.

In the long run, the Widefield ASKAP L-Band Legacy All-sky Blind Survey (WALLABY Koribalski 2012) and the Westerbork Northern Sky HI Survey (WNSHS) will image the entire sky in H I 21 cm emission. Their fine angular resolutions ($\sim 15'' - 30''$) precede that of current single-dish surveys (a few arcminutes) and will be able to identify fainter and smaller galaxies. With the synergy of other wide optical and NIR imaging survey, we will be able to recover a much more complete sample of the low SB galaxy population of the local Universe.

5.2.2 SB dependence on galaxy properties from Spectroscopy

We see from Chapter 2 that it is essential to break the degeneracy between the mass and the surface brightness in order to understand how the surface density affects the evolution of galaxies. We use broadband photometry as indicators for stellar age and metallicity based on stellar population synthesis models. However, the broadband photometry can only yield a qualitative view. On the contrary, spectroscopic data can derive more accurate stellar age and metallicity from the strength of characteristic spectral lines, or the more comprehensive full spectrum fitting technique.

One issue with current spectroscopic data is that most are spatially unresolved and contain information from only part of the target galaxy. For either a slit or fiber spectrograph, only light within the aperture will be collected, thus, provides information on only a local region. Comparing spectra from two galaxies of different sizes is non-trivial even with the same observation configuration. IFU spectra can help mitigate this problem by covering large areas of target galaxies. In addition, the spatially-resolved spectra allow investigate the effect of local surface density on galaxy properties (e.g., Sánchez-Menguiano et al. 2016; Cano-Díaz et al. 2016; Ruiz-Lara et al. 2016).

Extragalactic surveys with IFU are taking off in recent years. The number of galaxies covered by IFU observations will become closer to what we have now for integrated spectra. At the time this dissertation research started, only the Calar Alto Legacy Integral Field Area Survey (CALIFA; Sánchez et al. 2012) had started to release data. As of April 2016, the CALIFA survey has completed a survey of 667 galaxies. But the CALIFA survey sample is limited in narrow mass and surface brightness ranges. The ongoing SAMI and MANGA IFU surveys, on the other hand, will push the stellar mass limit down to $10^{8.2}M_{\odot}$ and 10^9M_{\odot} , respectively (Bryant et al. 2015; Bundy et al. 2015). The two surveys together will yield IFU spectra of more than 10,000 galaxies in a wide range of stellar mass and surface brightness in the next a few years. With these data, we will be able to probe stellar age profiles and chemical abundance profiles and how these properties are affected by the mass and the surface brightness of galaxies.

5.2.3 Constraining the gas flow properties of galaxies

The mass-loss loading factor, the ratio between outflow rate and star-formation rate, is of great interest. Galactic winds play a vital role in the evolution of galaxies. Several galaxy scaling relations are shaped by galactic winds, e.g., the galaxy luminosity function (Dekel & Silk 1986; Powell et al. 2011), the Tully-Fisher relation (Dutton & van den Bosch 2009; Dutton 2012), and the mass-metallicity relation (Spitoni et al. 2010; Zahid et al. 2012; Lilly et al. 2013). There have been many attempts to directly observe galactic winds in both the local universe and at high-redshifts (e.g., Lehnert & Heckman 1996; Heckman et al. 2000; Veilleux et al. 2005). Nevertheless, our knowledge to date are mostly based on galaxies with extreme SFR where the outflow is stronger and easier to measure (e.g., Martin 2005; Repke et al. 2005; Martin & Bouché 2009).

Instead of directly observing the outflowing gas, in Chapter 3, we combine analytical chemical evolution models and observed metallicity, stellar mass, and gas profiles of galaxies to constrain the strength of gas flows and investigate the effect of surface brightness. However, we are not able to put stringent constraint on the outflow strength in Chapter 3. Without direct measurement of gas profiles of individual galaxies, we have adopted empirical scaling relations between the gas profile and the size of the optical disk to infer the gas distribution. We find that the mass-loss loading factor η in the model is sensitive to the gas amount, therefore, there is large systemic uncertainty.

Follow-up observations obtaining the gas profile of galaxies will provide better constraint on their outflow strength. For the galaxy sample used in Chapter 3, their atomic and molecular gas content can be mapped by radio interferometers (e.g., WSRT, VLA) and single-dish mm/sub-mm antenna (e.g. JCMT, IRAM 30m) within one to a few hours of integration time. Moreover, some of the galaxies have been observed by neutral hydrogen or molecular surveys [i.e., Westerbork HI Survey of Irregular and Spiral Galaxies (WHISP; van der Hulst et al. 2001) and the JCMT Nearby Galaxies Legacy Survey (Wilson et al. 2012)], so the observational cost is further reduced. Using the method in Chapter 3, the study of the properties of gas flows can be done with a reasonable investment of observing

resources. Coming optical IFU surveys will measure metallicity profiles of galaxies of wider ranges of mass and SB. These galaxies can be followed-up by VLA and ALMA observations, which yield matched angular resolution of gas profiles, providing a probe of their inflow and outflow strengths.

References

- Allen, J. T., Croom, S. M., Konstantopoulos, I. S., et al. 2015, *MNRAS*, 446, 1567
- Bland-Hawthorn, J. 2014, in *IAU Symp. 309, "Galaxy in 3D across the Universe"*, B. L. Ziegler, F. Combes, H. Dannerbauer, M. Verdugo, Eds. (Cambridge: Cambridge Univ. Press)
- Bryant, J. J., Owers, M. S., Robotham, A. S. G., et al. 2015, *MNRAS*, 447, 2857
- Bundy, K., Bershady, M. A., Law, D. R. et al. 2015, *ApJ*, 798, 7
- Cano-Díaz, M., Sánchez, S. F., Zibetti, S., et al. 2016, *arXiv:1602.02770*
- Dekel, A., Silk, J. 1986, *ApJ*, 303, 39
- Dutton, A. A. 2012, *MNRAS*, 424, 3123
- Dutton, A. A., & van den Bosch, F. C. 2009, *MNRAS*, 396, 141
- Ellison, S. L., Patton, D. R., Simard, L., et al. 2009, *ApJ*, 672, 107
- Heckman, T. M., Lehnert, M. D., Strickland, D. K., & Armus, L. 2000, *ApJS*, 129, 493
- Kaiser, N., Burgett, W., Chambers, K., et al. 2010, *Proc. SPIE*, 7733, 0
- Kamphuis, P., Józsa, G. I. G., Oh, S.-H., et al. 2015, *MNRAS*, 452, 3139
- Kennicutt, R. C. Jr., Armus, L., Bendo, G., et al. 2003, *PASP*, 115, 928

Koribalski, B. S. 2012, PASA, 29, 359

Kudritzki, R.-P. Ho, I.-T., Schruba, A., et al. 2015, MNRAS, 450, 342

Lehnert, M. D., & Heckman, T. M. 1996, ApJ, 462, 651

Lilly, S. J., Carollo, C. M., Pipino, A., Renzini, A., Peng, Y. 2013, ApJ, 772, 119

Martin, C. L. 2005, ApJ, 621, 227

Martin, C. L., & Bouché, N. 2009, ApJ, 703, 1394

Powell, L. C., Slyz, A., Devriendt, J. 2011, MNRAS, 414, 3671

Rupke, D. S., Veilleux, S., & Sanders, D. B. 2005, ApJS, 160, 87

Ruiz-Lara, T., Pérez, I., Florido, E., et al. 2016, MNRAS, 456, 35

Sánchez, S. F., Kennicutt, R. C., Gil de Paz, A., et al. 2012, A&A, 538, 8

Sánchez-Menguiano, L., Sánchez, S. F., Pérez, I., et al. 2016, A&A, 587, 70

Spitoni, E., Calura, F., Matteucci, F., & Recchi, S. 2010, A&A, 514, 73

van der Hulst, J. M., van Albada, T. S., Sancisi, R. 2001, ASP Conf., 240, 451

van Dokkum, P. G., Pieter, G., Abraham, R., et al. 2015, ApJ, 798, 45

Veilleux, S., Cecil, G., & Bland-Hawthorn, J. 2005, ARA&A, 43, 769

Wilson, C. D., Warren, B. E., Israel, F. P., et al. 2012, MNRAS, 424, 3050

Zahid, H. J., Dima, G. I., Kewley, L. J., Erb, D. K., & Davé 2012, ApJ, 757, 54

Appendix A

Structural properties and photometry of the WISE galaxy sample

In this Appendix, I present the multi-wavelength photometry, surface brightness, scale length, stellar mass, H I mass and other basic properties of the WISE sample. These measurements are used throughout this dissertation.

Table A.1: Morphology, size, surface brightness and scale length of the WISE galaxy sample

PGC	Name	AGC	D (Mpc)	T	Tn	a ($'$)	b ($'$)	i ($^{\circ}$)	μ_0 ($\frac{mag}{arcsec^2}$)	$\mu_{0,i}$ ($\frac{mag}{arcsec^2}$)	$R_{d,kpc}$ (kpc)
(1)	(2)	(3)	(4)	(5)	(6)	(7)	(8)	(9)	(10)	(11)	(12)
218	NGC7814	8	13.68	Sab	2.0	5.60	2.02	72	19.47	20.57	3.38
255	UGC00017	17	20.32	Sm	9.1	0.96	0.47	62	23.15	23.92	2.50
647	NGC0014	75	5.73	IB	9.9	2.12	1.42	49	21.80	22.24	0.89
697	PGC000697	100062	11.85	Sc	4.9	0.59	0.42	46	21.13	21.50	0.28
878	PGC000878	119	25.80	S?	1.6	1.15	0.68	55	19.77	20.34	0.89
2216	PGC002216	100345	25.67	Sm	9.0	0.67	0.45	48	20.30	20.73	0.60
5974	NGC0628	1149	6.81	Sc	5.2	10.50	9.50	25	20.01	20.12	2.10
6150	UGC01171	1171	6.81	I	9.8	0.85	0.41	63	23.07	23.87	0.47
6174	UGC01176	1176	8.40	I	9.9	4.60	3.60	39	23.63	23.90	1.60
6364	UGC01211	1211	30.24	I	9.8	0.95	0.83	29	22.72	22.86	2.52
7841	UGC01551	1551	33.41	SBc	6.1	1.73	1.52	29	21.18	21.31	3.18
7849	NGC0803	1554	21.78	Sc	5.3	2.78	1.15	68	20.95	21.91	2.86
7871	UGC01561	1561	9.73	I	9.9	1.28	0.95	42	22.66	22.98	1.08
8535	UGC01711	1711	32.95	I	9.8	0.99	0.44	66	20.69	21.58	1.14
9403	PGC009403	120272	35.00	(...)	(...)	0.84	0.50	55	19.94	20.51	0.87
9447	UGC01958	1958	19.86	Sc	5.9	1.00	0.53	59	21.47	22.16	0.84
9705	UGC02017	2017	24.70	I	9.9	0.78	0.44	57	23.95	24.56	3.20
9788	NGC0972	2045	15.78	Sab	2.1	3.45	1.65	63	19.17	19.97	2.10
10051	NGC1012	2141	24.70	S0-a	0.3	2.99	1.12	71	19.67	20.73	2.65
10272	NGC1056	2183	30.90	Sa	1.0	2.28	1.35	55	21.31	21.88	4.05
11329	NGC1156	2455	4.47	IB	9.8	2.80	1.66	55	19.95	20.52	0.58

Table A.1 – continued

PGC (1)	Name (2)	AGC (3)	D (4)	T (5)	Tn (6)	a (7)	b (8)	inc (9)	μ_0 (10)	$\mu_{0,i}$ (11)	$R_{d,kpc}$ (13)
20981	PGC020981	170328	16.80	I	10.0	0.53	0.49	23	19.84	19.92	0.27
21120	UGC03876	3876	24.00	Scd	6.6	2.32	1.03	66	20.62	21.50	2.39
21303	PGC021303	3912	14.40	I	9.8	1.60	0.96	55	21.91	22.47	1.44
22277	UGC04115	4115	7.87	I	9.9	1.82	1.00	58	22.45	23.10	0.81
23214	IC2256	180156	35.16	Sc	5.9	1.05	0.54	60	19.39	20.10	1.04
23283	PGC023283	180181	31.17	S?	9.0	0.50	0.40	37	19.51	19.75	0.43
23559	PGC023559	4385	28.28	Sm	9.0	1.06	0.89	34	20.71	20.91	1.17
23646	IC2361	4394	29.31	SBab	2.0	1.78	0.66	71	19.52	20.59	1.48
23707	UGC04418	4418	35.16	SABc	6.5	1.09	0.61	57	21.54	22.17	1.67
23762	PGC023762	180293	30.61	Sm	9.0	1.21	1.01	34	19.96	20.16	1.18
24012	PGC024012	180350	31.27	Sb	2.5	1.11	0.56	61	19.91	20.65	1.01
24425	NGC2644	4533	28.28	Sc	4.6	2.27	0.99	66	19.61	20.50	1.96
24457	PGC024457	4540	29.68	Sd	8.0	1.42	1.12	39	22.10	22.36	2.46
24469	PGC024469	180447	30.90	Sbc	4.2	1.30	0.54	68	20.06	21.02	1.21
24666	PGC024666	180485	30.80	S?	5.0	0.62	0.50	37	20.03	20.27	0.53
24699	UGC04599	4599	29.87	S0	-2.0	1.71	1.31	41	23.21	23.50	4.34
25332	PGC025332	4732	30.05	S?	5.0	0.95	0.79	34	18.59	18.79	0.72
25376	NGC2731	4741	25.94	Sbc	4.2	1.39	0.93	49	19.10	19.53	1.03
25399	NGC2735	4744	34.53	SABb	3.0	2.54	1.14	65	17.97	18.83	1.32
25496	NGC2743	4760	41.33	Sd	7.9	1.10	0.75	48	19.30	19.72	1.81
25525	NGC2750	4769	41.33	SABc	5.3	2.03	1.46	45	19.75	20.11	3.68
25556	UGC04781	4781	25.59	Sc	5.9	1.41	0.60	67	23.37	24.30	3.98
25679	UGC04797	4797	19.51	Sm	8.8	1.60	1.43	27	22.97	23.10	2.55
25861	NGC2775	4820	20.16	Sab	1.7	3.75	2.88	41	19.54	19.83	4.05
25876	PGC025876	4823	22.21	Sab	2.0	0.98	0.72	43	19.62	19.95	0.67

Table A.1 – continued

PGC	Name	AGC	D	T	Tn	a	b	inc	μ_0	$\mu_{0,i}$	$R_{d,kpc}$
(1)	(2)	(3)	(4)	(5)	(6)	(7)	(8)	(9)	(10)	(11)	(13)
26218	UGC04902	4902	26.10	S0	-1.6	1.71	0.91	59	20.17	20.86	1.49
26453	PGC026453	190238	19.88	Sm	9.0	0.56	0.51	24	21.39	21.49	0.73
26570	PGC026570	191176	35.00	SBm	8.8	1.25	0.58	65	20.51	21.36	1.56
26781	NGC2882	5030	35.97	Sc	5.0	2.01	0.94	64	18.01	18.84	1.60
26932	NGC2894	5056	51.76	Sa	1.0	2.16	1.07	62	20.98	21.73	6.98
27074	NGC2906	5081	44.87	Sc	5.9	2.21	1.32	54	18.27	18.83	2.47
27228	PGC027228	191249	12.13	S?	4.6	0.90	0.65	44	20.70	21.05	0.38
27232	NGC2919	5102	41.69	SABb	3.7	2.28	0.87	70	18.23	19.27	2.15
27622	PGC027622	191287	19.88	Sm	9.0	0.74	0.51	47	19.53	19.93	0.41
27635	NGC2962	5167	31.05	S0-a	-1.1	4.32	2.75	51	19.77	20.26	3.34
27734	NGC2966	5181	33.60	Sbc	4.2	2.72	1.02	71	19.85	20.91	3.35
27910	IC0559	190472	8.77	Sm	9.0	1.09	0.90	35	21.47	21.67	0.46
28296	NGC3020	5271	21.68	Sc	5.9	2.23	1.07	63	21.52	22.32	3.00
28324	NGC3024	5275	18.30	Sc	5.0	1.99	0.70	72	19.87	21.00	1.14
28378	PGC028378	5288	6.35	SABd	8.1	1.20	0.89	43	21.38	21.71	0.39
28590	NGC3049	5325	19.32	SBb	2.5	2.22	1.66	42	19.33	19.65	1.26
28617	NGC3055	5328	27.42	SABc	5.3	2.77	2.11	41	18.90	19.20	1.61
28627	PGC028627	190600	19.32	Sab	2.0	1.02	0.60	55	21.28	21.86	0.86
28682	PGC028682	5335	26.40	S0-a	0.0	1.20	1.04	30	18.04	18.20	0.67
28913	UGC05373	5373	1.38	IB	9.9	11.81	10.18	31	23.57	23.73	0.64
29009	NGC3094	5390	44.70	SBa	1.1	1.34	0.98	44	21.04	21.38	4.00
29198	PGC029198	200879	19.04	S?	3.0	0.55	0.47	32	20.16	20.33	0.34
29408	PGC029408	5453	12.13	I	9.8	0.92	0.67	44	21.49	21.83	0.55
29413	UGC05454	5454	39.76	SABd	8.0	1.03	0.69	49	21.83	22.26	1.49
29428	UGC05456	5456	5.23	Sm	9.0	1.86	1.53	35	22.34	22.56	0.63

Table A.1 – continued

PGC (1)	Name (2)	AGC (3)	D (4)	T (5)	Tn (6)	a (7)	b (8)	inc (9)	μ_0 (10)	$\mu_{0,i}$ (11)	$R_{d,kpc}$ (13)
29435	IC0591	5458	32.70	Sc	6.0	0.93	0.60	51	19.40	19.88	1.16
29747	NGC3153	5505	35.97	Sc	5.9	2.19	1.01	64	19.85	20.69	2.51
29835	UGC05522	5522	41.88	Sc	6.4	2.19	1.18	59	21.28	21.95	2.98
30042	PGC030042	5551	20.25	I	9.8	0.66	0.53	37	22.54	22.77	0.85
30263	PGC030263	5588	26.40	Sc	6.0	0.97	0.87	27	18.69	18.81	0.64
30531	UGC05633	5633	28.60	SBd	8.0	2.19	1.45	50	22.83	23.28	4.36
30684	NGC3246	5661	35.50	Sd	7.9	2.12	1.05	62	20.75	21.51	3.12
30773	PGC030773	731452	18.95	Sab	2.3	0.65	0.61	20	21.34	21.40	0.54
31081	PGC031081	5716	19.69	Sm	8.8	0.71	0.70	11	22.52	22.54	0.83
31122	NGC3274	5721	7.37	Scd	6.6	1.85	1.08	56	20.07	20.65	0.44
31387	PGC031387	201524	21.47	S?	7.0	0.84	0.62	43	19.55	19.88	0.52
31442	NGC3299	5761	11.10	SABd	8.0	2.39	1.51	52	20.46	20.96	1.09
31528	NGC3306	5774	46.56	SBd	7.8	1.04	0.45	67	19.13	20.05	2.17
31610	PGC031610	200499	9.71	S0	-1.6	1.02	0.78	41	20.59	20.89	0.37
31877	PGC031877	200532	9.71	S0-a	0.0	1.11	0.53	64	21.54	22.35	0.44
31883	NGC3338	5826	23.66	Sc	5.1	5.39	3.02	57	20.12	20.75	4.26
31930	UGC05832	5832	16.33	Sbc	4.2	1.45	1.13	39	20.67	20.93	1.00
31937	PGC031937	200543	16.33	S?	10.0	0.64	0.54	34	22.45	22.64	0.60
31968	NGC3344	5840	9.82	Sbc	4.0	4.99	4.25	32	19.63	19.81	2.02
31982	NGC3346	5842	21.40	SBc	5.9	2.58	2.15	34	19.06	19.25	1.84
32007	NGC3351	5850	10.47	Sb	3.1	10.19	6.55	51	19.27	19.75	2.51
32192	NGC3368	5882	10.52	SABa	2.2	14.43	9.54	50	19.52	19.96	3.02
32226	NGC3377A	5889	8.24	SABm	8.9	1.99	1.66	34	22.83	23.03	1.20
32257	PGC032257	200581	39.85	S?	6.0	0.84	0.73	31	20.98	21.14	1.49
32306	NGC3389	5914	20.80	Sc	5.3	3.27	1.20	71	18.84	19.93	1.90

Table A.1 – continued

PGC (1)	Name (2)	AGC (3)	D (4)	T (5)	Tn (6)	a (7)	b (8)	inc (9)	μ_0 (10)	$\mu_{0,i}$ (11)	$R_{d,kpc}$ (13)
32345	PGC032345	200600	16.33	Sd	8.0	0.77	0.54	46	21.29	21.67	0.52
32346	PGC032346	200598	16.33	S?	4.0	0.69	0.41	55	21.39	21.97	0.49
32347	NGC3391	5920	47.40	Sab	1.9	0.87	0.56	51	20.19	20.66	1.88
32364	UGC05923	5923	20.81	S0-a	0.4	1.26	0.69	59	19.61	20.28	0.74
32368	UGC05921	5921	26.10	SBd	8.1	1.72	0.75	66	20.95	21.86	1.43
32496	UGC05948	5948	10.36	I	10.0	0.72	0.63	28	21.36	21.50	0.32
32529	NGC3423	5962	17.00	Sc	6.0	3.90	3.46	28	19.21	19.35	1.86
32533	NGC3414	5959	25.70	S0	-2.0	3.52	2.73	40	20.25	20.53	4.07
32549	NGC3418	5963	23.99	S0-a	0.2	1.63	1.10	49	19.93	20.36	1.36
32570	UGC05974	5974	23.66	Sc	5.9	1.60	0.67	68	21.39	22.34	1.65
32605	NGC3433	5981	33.70	Sc	5.3	2.51	2.40	17	19.99	20.04	2.93
32708	UGC06014	6014	9.71	SABd	8.0	1.09	0.66	54	22.43	22.98	0.70
32754	NGC3451	6023	28.18	SBCd	6.6	1.93	0.97	61	18.82	19.56	1.40
33140	NGC3485	6077	20.99	Sb	3.1	2.30	1.94	33	19.57	19.75	1.58
33160	NGC3489	6082	11.86	S0-a	-1.2	3.58	1.92	59	21.63	22.30	2.70
33371	NGC3504	6118	26.10	Sab	2.1	2.79	1.74	53	19.33	19.85	2.46
33432	NGC3512	6128	26.10	Sc	5.1	1.69	1.43	33	18.87	19.06	1.27
33447	PGC033447	210023	9.71	I	10.0	1.00	0.41	68	22.13	23.11	0.49
33463	UGC06138	6138	36.68	Sm	8.6	0.95	0.69	44	21.82	22.16	2.01
33642	UGC06169	6169	19.68	Sb	3.0	1.76	0.66	71	19.51	20.58	0.94
33652	PGC033652	212032	36.40	S?	3.0	0.68	0.46	49	20.63	21.07	0.87
33816	PGC033816	210082	16.33	S?	9.0	1.11	0.79	46	20.54	20.92	0.61
33866	NGC3547	6209	21.09	Sb	3.1	1.82	1.00	58	19.04	19.69	1.04
33905	PGC033905	210111	16.33	Sm	9.0	0.74	0.49	49	22.67	23.10	0.93
33981	PGC033981	213064	16.33	S?	3.0	0.55	0.46	34	19.82	20.02	0.27

Table A.1 – continued

PGC (1)	Name (2)	AGC (3)	D (4)	T (5)	Tn (6)	a (7)	b (8)	inc (9)	μ_0 (10)	$\mu_{0,i}$ (11)	$R_{d,kpc}$ (13)
34015	PGC034015	6233	24.27	S0-a	0.4	1.19	0.67	57	19.45	20.08	0.78
34107	IC0676	6245	26.90	S0-a	-1.3	2.11	1.42	49	20.08	20.52	2.13
34124	UGC06248	6248	16.33	IAB	9.9	0.68	0.56	35	22.67	22.89	0.70
34135	PGC034135	212097	16.33	Sbc	4.2	1.24	0.46	71	19.87	20.95	0.62
34151	PGC034151	212102	36.21	SABc	5.0	0.93	0.92	9	20.55	20.56	1.23
34257	NGC3593	6272	8.95	S0-a	-0.4	5.14	1.83	72	19.07	20.20	1.55
34298	NGC3596	6277	10.10	SABc	5.2	2.29	2.05	27	18.93	19.05	0.82
34438	PGC034438	210220	9.61	S?	10.0	0.83	0.70	32	22.56	22.73	0.52
34478	NGC3611	6305	26.90	Sa	1.0	2.23	1.46	50	19.50	19.96	1.88
34529	PGC034529	6317	33.23	I	9.9	1.04	0.42	68	21.98	22.96	1.90
34695	NGC3627	6346	9.04	SABb	3.1	9.24	3.74	69	18.41	19.39	2.76
34719	NGC3629	6352	32.36	SABc	5.9	1.95	1.46	42	20.12	20.44	2.24
34887	IC2763	6387	18.50	Sc	6.0	1.43	0.52	72	21.21	22.31	1.09
35044	UGC06421	6421	23.33	Sd	8.0	0.79	0.55	46	22.04	22.43	1.01
35151	PGC035151	6438	19.04	S?	2.0	1.05	0.74	46	19.94	20.33	0.61
35225	IC2828	210340	16.80	S?	9.0	0.98	0.70	45	20.58	20.95	0.58
35294	NGC3689	6467	46.99	SABc	5.3	1.48	0.97	50	18.43	18.89	2.51
35405	NGC3701	6493	38.37	Sbc	4.0	1.60	0.77	63	19.83	20.63	2.41
35440	NGC3705	6498	19.14	SABa	2.4	4.18	1.87	65	18.97	19.85	2.58
35739	PGC035739	210459	19.97	Sc	4.9	0.91	0.45	62	20.84	21.60	0.68
36043	NGC3773	6605	16.30	S0	-2.0	1.58	1.22	40	20.57	20.85	0.97
36174	IC0718	6626	29.21	I	9.8	1.67	1.21	44	20.19	20.54	1.27
36205	IC0719	6633	28.40	S0	-1.9	1.91	0.79	68	18.22	19.18	1.28
36243	NGC3810	6644	16.37	Sc	5.2	3.40	2.24	50	18.85	19.31	1.93
36295	PGC036295	6655	21.60	S0-a	-1.0	0.90	0.69	41	20.11	20.41	0.65

Table A.1 – continued

PGC (1)	Name (2)	AGC (3)	D (4)	T (5)	Tn (6)	a (7)	b (8)	inc (9)	μ_0 (10)	$\mu_{0,i}$ (11)	$R_{d,kpc}$ (13)
36344	UGC06669	6669	15.03	I	9.9	1.32	0.68	61	23.82	24.55	1.67
36571	UGC06717	6717	40.60	SBm	8.8	1.37	1.37	0	23.63	23.63	4.61
36644	NGC3876	6730	42.79	Sab	2.3	1.12	0.64	57	19.77	20.39	2.06
36896	UGC06782	6782	13.70	I	9.8	3.78	2.77	43	23.44	23.77	1.57
36914	NGC3900	6786	37.15	S0-a	-0.2	3.33	1.43	67	19.67	20.59	4.79
36976	PGC036976	210822	10.19	Sc	5.9	0.73	0.49	48	21.53	21.95	0.35
36979	NGC3912	6801	22.50	Sb	3.1	2.21	0.99	65	19.20	20.08	1.40
37162	PGC037162	210861	16.43	Sbc	4.3	0.77	0.47	53	22.02	22.54	0.65
37301	PGC037301	210891	36.40	(...)	(...)	0.52	0.41	38	20.51	20.76	0.58
37483	NGC3976	6906	36.81	SABb	3.2	3.62	1.81	62	19.56	20.31	3.74
37779	PGC037779	210968	23.43	Scd	7.4	0.92	0.65	46	20.95	21.33	0.89
37928	NGC4037	7002	15.59	Sb	2.9	3.30	2.82	31	21.13	21.30	2.12
37931	PGC037931	211006	23.80	Sc	4.6	0.76	0.63	35	19.74	19.95	0.55
37954	PGC037954	211013	22.21	SB?	5.0	0.94	0.61	50	20.06	20.52	0.65
38113	PGC038113	222046	16.33	S0-a	-1.5	1.05	0.71	48	18.47	18.89	0.41
38168	NGC4067	7048	44.87	Sb	3.1	1.56	1.10	46	18.75	19.13	1.91
38244	NGC4080	7068	14.00	SBm	9.5	1.75	0.95	59	19.31	19.97	0.67
38299	PGC038299	220074	24.27	Sc	6.2	0.58	0.43	42	20.59	20.91	0.48
38627	IC3017	220150	28.09	Sc	4.6	0.84	0.54	51	19.43	19.91	0.58
38637	UGC07138	7138	31.92	SABc	6.6	1.37	0.89	51	21.89	22.36	2.32
38667	UGC07143	7143	36.96	Sc	4.9	1.08	0.65	54	19.41	19.95	1.15
38684	IC3021	7149	32.50	Sm	9.0	1.03	0.78	42	22.24	22.55	2.00
38692	IC3023	7150	7.19	I	9.7	0.69	0.49	45	22.55	22.91	0.35
38726	PGC038726	220167	19.05	S0-a	-1.3	1.08	0.70	51	21.06	21.54	0.83
38728	PGC038728	220168	28.09	S?	5.0	0.49	0.46	19	20.82	20.89	0.52

Table A.1 – continued

PGC (1)	Name (2)	AGC (3)	D (4)	T (5)	Tn (6)	a (7)	b (8)	inc (9)	μ_0 (10)	$\mu_{0,i}$ (11)	$R_{d,kpc}$ (13)
38747	PGC038747	220171	15.59	S?	3.0	0.77	0.44	57	19.93	20.54	0.36
38749	NGC4152	7169	34.80	SABc	5.0	1.78	1.43	37	19.00	19.23	1.79
38803	IC3033	7181	15.14	Sd	7.7	1.17	0.60	61	21.76	22.48	0.91
38835	PGC038835	221647	35.84	Sc	6.2	0.64	0.42	50	21.22	21.69	0.89
38851	NGC4162	7193	43.85	Sbc	4.0	2.38	1.39	55	18.81	19.39	2.83
38885	NGC4165	7201	30.06	SABa	1.9	1.41	0.96	48	20.05	20.46	1.60
38888	PGC038888	7200	15.59	Sm	9.0	1.48	1.10	42	22.36	22.68	1.27
38916	IC0769	7209	34.04	Sbc	4.0	2.65	1.20	65	20.89	21.76	4.11
38945	IC3044	7216	16.80	SBc	6.0	1.88	0.77	68	21.46	22.43	1.47
38964	NGC4180	7219	31.50	Sab	2.0	2.00	1.03	60	21.38	22.09	3.09
39002	PGC039002	7223	34.99	Scd	7.0	0.89	0.77	30	22.60	22.76	2.15
39009	IC3049	7227	15.59	Sm	8.9	0.76	0.58	41	20.82	21.11	0.43
39018	PGC039018	220212	15.59	Sc	4.9	1.00	0.65	50	20.96	21.43	0.60
39025	NGC4189	7235	25.23	Sc	6.0	2.86	1.79	52	18.80	19.31	2.15
39034	NGC4191	7233	16.43	S0	-1.8	1.65	1.33	37	20.61	20.84	1.26
39040	NGC4193	7234	38.37	SABb	4.1	2.70	1.29	63	19.25	20.06	3.14
39052	PGC039052	220217	22.59	Sbc	4.2	1.40	0.54	70	19.86	20.89	0.90
39067	UGC07239	7239	15.40	IB	9.8	3.27	3.27	0	21.60	21.60	1.38
39142	IC3059	7254	15.59	IB	9.8	1.38	1.29	21	22.72	22.80	1.35
39181	IC3066	7262	15.59	Sbc	4.2	1.15	0.43	71	20.03	21.09	0.54
39206	NGC4207	7268	16.90	Sm	9.3	2.17	1.69	39	19.93	20.20	1.04
39224	NGC4212	7275	16.52	Sc	4.9	3.34	1.83	58	17.96	18.62	1.43
39230	PGC039230	220255	22.59	Sm	8.9	0.89	0.50	57	21.89	22.51	0.93
39256	IC3077	7285	8.49	Scd	6.8	1.31	1.00	41	22.53	22.83	0.97
39265	PGC039265	220264	22.59	I	10.0	0.84	0.52	53	21.05	21.59	0.90

Table A.1 – continued

PGC (1)	Name (2)	AGC (3)	D (4)	T (5)	Tn (6)	a (7)	b (8)	inc (9)	μ_0 (10)	$\mu_{0,i}$ (11)	$R_{d,kpc}$ (13)
39288	PGC039288	222297	22.59	S0-a	-1.2	0.76	0.55	44	21.12	21.48	0.71
39328	NGC4224	7292	51.29	Sa	1.0	3.40	1.43	67	19.50	20.44	6.28
39358	IC3096	220282	15.59	S0-a	-1.0	1.54	0.63	68	21.53	22.50	1.03
39362	PGC039362	7305	15.68	Sc	5.1	0.94	0.90	18	19.11	19.17	0.39
39392	PGC039392	220289	22.59	S?	5.0	0.53	0.41	40	20.78	21.07	0.44
39393	NGC4237	7315	20.14	SABb	4.0	2.69	1.53	57	18.82	19.43	1.70
39412	IC3102	7319	33.88	S0-a	-0.9	3.23	1.42	66	19.94	20.84	4.31
39431	IC3105	7326	16.80	I	9.8	1.61	0.58	72	21.81	22.92	1.13
39483	NGC4241	7333	15.14	Sc	5.5	2.11	1.89	27	21.84	21.96	1.57
39513	PGC039513	220321	15.59	S0-a	-1.3	0.76	0.62	36	22.26	22.48	0.70
39537	NGC4252	7343	15.40	Sb	3.1	1.53	0.72	64	20.13	20.95	0.64
39578	NGC4254	7345	13.87	Sc	5.2	5.23	4.88	21	19.30	19.37	2.52
39613	IC0776	7352	32.66	SBd	7.9	1.38	0.91	50	21.97	22.42	2.88
39619	PGC039619	7355	15.59	IAB	9.5	0.83	0.51	53	21.97	22.49	0.71
39641	PGC039641	220353	16.80	Sm	9.0	0.58	0.57	11	20.47	20.50	0.32
39646	PGC039646	220354	15.40	Sd	8.0	0.75	0.61	36	21.05	21.27	0.42
39655	PGC039655	220360	21.37	S0-a	-1.0	0.86	0.59	48	19.83	20.25	0.56
39658	IC3148	220358	22.59	S?	8.9	0.91	0.76	34	21.71	21.91	0.99
39718	NGC4270	7376	23.88	S0	-2.0	2.62	1.33	61	19.43	20.16	2.02
39728	PGC039728	7382	33.97	Sb	3.1	1.21	1.13	22	17.86	17.94	0.91
39738	NGC4273	7380	31.48	Sc	5.2	2.50	1.43	56	18.72	19.33	2.25
39765	NGC4276	7385	31.50	SABd	7.6	1.72	1.46	32	20.24	20.42	1.94
39813	PGC039813	220399	22.59	Sc	5.1	0.72	0.53	44	21.42	21.76	1.02
39860	NGC4287	220412	16.43	Sb	3.4	1.63	0.62	70	21.22	22.26	1.13
39878	PGC039878	220418	15.40	Sd	8.4	0.79	0.50	51	21.66	22.15	0.56

Table A.1 – continued

PGC (1)	Name (2)	AGC (3)	D (4)	T (5)	Tn (6)	a (7)	b (8)	inc (9)	μ_0 (10)	$\mu_{0,i}$ (11)	$R_{d,kpc}$ (13)
39925	NGC4294	7407	16.52	SBC	5.8	3.18	1.38	66	19.59	20.50	1.56
39968	NGC4299	7414	16.80	SABm	8.5	1.73	1.55	26	20.16	20.27	1.10
40001	NGC4303	7420	17.60	Sbc	4.0	5.93	5.15	30	18.81	18.96	3.01
40004	PGC040004	7423	23.40	SABm	9.0	1.27	0.56	66	22.68	23.57	2.02
40014	UGC07424	7424	15.31	I	9.8	1.04	0.94	25	22.06	22.16	0.91
40021	UGC07422	7422	16.43	SBb	2.5	1.54	0.66	67	18.64	19.56	0.62
40087	NGC4301	7439	15.49	Sc	6.4	1.34	1.14	32	20.60	20.77	0.82
40100	PGC040100	220456	16.80	I	10.0	0.60	0.49	36	21.81	22.04	0.45
40105	NGC4313	7445	13.49	Sab	2.1	4.10	1.82	66	19.49	20.37	1.75
40147	IC3229	7448	21.37	Sbc	4.0	1.30	0.62	63	20.90	21.71	1.01
40153	NGC4321	7450	13.93	SABb	4.1	13.20	12.04	24	19.72	19.82	3.87
40179	NGC4324	7451	26.18	S0-a	-0.9	3.13	1.39	66	18.27	19.15	1.96
40187	IC3239	220479	15.59	Sc	5.5	0.87	0.43	62	21.33	22.09	0.55
40201	NGC4330	7456	19.05	Sc	6.1	5.59	2.10	71	20.01	21.07	2.34
40229	PGC040229	220493	15.40	S?	9.0	0.57	0.41	46	20.71	21.09	0.32
40251	NGC4343	7465	23.40	Sb	3.0	2.71	1.77	50	19.38	19.84	1.77
40264	IC3258	7470	16.80	IB	9.7	3.32	2.35	46	22.48	22.85	1.97
40273	IC3259	7469	18.37	SABd	7.9	2.03	1.06	60	20.28	20.98	1.29
40303	NGC4353	220502	23.40	IB	9.9	1.53	0.98	51	18.95	19.44	0.89
40306	NGC4351	7476	16.80	SBab	2.5	2.15	1.37	52	21.29	21.78	2.03
40310	PGC040310	220506	22.59	SABm	8.6	0.96	0.72	42	21.86	22.17	1.17
40317	IC3267	7474	15.68	Sc	5.9	1.97	1.56	38	20.29	20.55	0.90
40321	IC3268	7477	26.90	I	10.0	1.07	0.94	29	21.67	21.81	2.05
40342	NGC4356	7482	16.75	Sc	5.8	3.09	1.44	64	19.74	20.57	1.60
40408	PGC040408	220524	22.59	Sm	8.7	1.07	0.57	59	20.99	21.67	0.96

Table A.1 – continued

PGC (1)	Name (2)	AGC (3)	D (4)	T (5)	Tn (6)	a (7)	b (8)	inc (9)	μ_0 (10)	$\mu_{0,i}$ (11)	$R_{d,kpc}$ (13)
40461	PGC040461	220537	22.59	S0-a	-1.3	0.77	0.57	44	19.27	19.60	0.44
40490	NGC4378	7497	31.50	Sa	1.0	3.98	3.63	24	19.96	20.06	3.82
40494	NGC4376	7498	16.80	I	9.9	1.98	0.96	63	20.39	21.18	1.18
40495	PGC040495	7505	5.06	Scd	7.4	1.19	0.42	72	21.43	22.56	0.26
40507	NGC4380	7503	15.21	Sab	2.3	4.37	2.92	49	19.40	19.83	1.84
40588	PGC040588	220555	7.37	S?	10.0	0.97	0.51	60	21.67	22.37	0.38
40597	NGC4390	7519	16.80	SABc	5.0	1.94	1.25	51	20.13	20.61	1.19
40600	NGC4393	7521	16.30	Scd	6.7	2.95	2.75	21	22.16	22.24	2.39
40643	NGC4405	7529	16.80	S0-a	-0.1	2.10	1.49	46	19.17	19.54	1.06
40670	PGC040670	220572	16.90	S?	8.5	1.19	0.52	66	22.20	23.11	1.09
40695	NGC4411A	7537	16.80	Sc	5.4	3.43	2.93	32	21.59	21.76	1.82
40705	NGC4413	7538	15.07	Sab	2.0	2.31	1.36	55	20.17	20.75	1.56
40715	NGC4412	7536	30.60	SBb	3.1	1.81	1.69	21	19.14	19.22	1.63
40743	NGC4416	7541	15.68	Sc	5.9	2.53	2.36	21	19.22	19.30	0.86
40745	NGC4411B	7546	16.80	SABc	6.3	2.50	2.39	17	22.29	22.34	2.99
40761	IC3356	7547	13.37	I	9.7	0.69	0.62	24	23.67	23.77	0.97
40807	UGC07557	7557	16.80	SABm	8.8	4.88	4.19	31	19.34	19.51	1.28
40809	NGC4424	7561	15.68	SBa	1.0	3.78	1.43	70	20.34	21.40	2.75
40811	IC3365	7563	18.97	IB	9.9	1.75	0.65	71	21.53	22.61	1.67
40825	PGC040825	220602	22.59	S?	9.0	0.73	0.54	43	21.65	21.99	0.71
40851	NGC4430	7566	16.00	Sb	3.4	2.55	2.09	36	19.64	19.86	1.41
40861	UGC07567	7567	23.40	I	9.8	1.30	0.66	61	20.87	21.61	1.15
40876	PGC040876	220616	15.31	S?	8.5	1.04	0.62	55	21.86	22.43	0.78
40914	NGC4438	7574	16.80	Sa	0.6	17.10	7.46	66	21.36	22.26	8.61
40933	UGC07579	7579	30.60	Sd	8.2	1.57	0.55	72	19.70	20.84	1.40

Table A.1 – continued

PGC (1)	Name (2)	AGC (3)	D (4)	T (5)	Tn (6)	a (7)	b (8)	inc (9)	μ_0 (10)	$\mu_{0,i}$ (11)	$R_{d,kpc}$ (13)
40993	UGC07590	7590	29.24	Sbc	4.1	1.13	0.70	53	20.11	20.62	1.13
41036	UGC07596	7596	4.29	I	9.8	1.53	0.79	61	22.27	22.99	0.38
41050	NGC4451	7600	25.94	Sab	2.4	1.92	1.23	51	19.55	20.03	1.52
41061	IC3392	7602	11.91	Sab	2.4	2.88	1.28	65	19.55	20.42	1.13
41152	IC3412	220661	15.31	S?	8.5	1.07	0.52	62	21.84	22.62	0.86
41166	IC3414	7621	12.02	Sd	7.8	1.66	1.05	52	20.31	20.81	0.68
41170	PGC041170	7626	30.90	Sab	2.3	1.72	0.78	65	19.47	20.33	1.36
41178	PGC041178	220667	15.59	I	9.8	0.95	0.51	59	21.88	22.55	0.77
41189	NGC4470	7627	13.87	Sa	1.4	1.71	1.18	47	18.63	19.04	0.60
41317	NGC4480	7647	43.45	SABc	5.1	2.43	1.15	64	18.57	19.38	2.62
41383	NGC4492	7656	16.80	Sa	1.0	3.79	3.30	30	21.69	21.84	3.51
41440	IC3446	220724	16.80	Sm	8.9	0.77	0.53	47	20.19	20.58	0.41
41466	IC3453	7666	16.80	IB	9.7	1.42	0.55	70	20.32	21.36	0.74
41471	NGC4496A	7668	14.72	SBd	7.6	5.84	4.86	34	20.61	20.82	1.99
41504	IC0797	7676	14.52	Sc	6.0	1.78	1.21	48	21.10	21.52	1.30
41517	NGC4501	7675	19.68	Sb	3.3	6.26	2.69	67	18.23	19.15	4.30
41536	IC3466	220739	15.59	S?	10.0	0.86	0.66	41	23.24	23.54	1.36
41567	IC3471	220745	15.59	Sc	5.7	1.08	0.68	52	21.17	21.68	0.66
41608	IC3476	7695	13.30	IB	9.6	1.97	1.22	53	20.94	21.46	1.33
41619	PGC041619	220755	15.31	S?	8.5	0.77	0.48	53	22.19	22.71	0.58
41670	IC3483	220768	16.80	SABb	3.1	1.27	0.84	50	20.06	20.52	0.60
41716	PGC041716	220780	15.49	SBm	8.6	0.98	0.64	50	21.48	21.94	0.71
41719	NGC4519	7709	31.48	Scd	6.9	2.37	2.01	32	19.97	20.15	2.70
41729	NGC4522	7711	14.45	SBc	6.0	3.77	1.40	71	20.09	21.16	1.72
41746	NGC4523	7713	16.80	Sm	9.1	3.79	2.76	44	22.35	22.69	2.96

Table A.1 – continued

PGC (1)	Name (2)	AGC (3)	D (4)	T (5)	Tn (6)	a (7)	b (8)	inc (9)	μ_0 (10)	$\mu_{0,i}$ (11)	$R_{d,kpc}$ (13)
41763	IC0800	7716	13.93	Sc	5.2	1.97	1.34	48	20.64	21.06	1.08
41811	NGC4532	7726	13.80	IB	9.7	3.24	1.62	62	19.44	20.19	1.20
41812	NGC4535	7727	16.14	Sc	5.0	8.09	6.11	42	19.10	19.41	3.16
41829	IC3517	7733	13.93	SABm	8.5	1.15	0.70	54	21.12	21.66	0.67
41830	IC3520	220799	15.59	Sc	5.0	0.67	0.42	52	21.88	22.39	0.80
41847	IC3521	7736	16.80	IB	9.9	1.98	1.24	52	20.43	20.94	1.26
41861	UGC07739	7739	13.80	I	9.8	1.16	0.88	41	21.88	22.18	0.93
41865	IC3522	7737	16.80	IB	9.9	1.23	0.52	67	21.55	22.48	0.88
41876	NGC4540	7742	16.80	SABc	6.2	2.10	1.59	41	20.18	20.48	1.75
41934	NGC4548	7753	17.14	Sb	3.1	6.67	5.41	36	19.35	19.58	3.32
41942	PGC041942	220819	15.40	S0-a	-1.0	0.72	0.59	35	21.40	21.61	0.59
42002	NGC4559	7766	7.31	Sc	6.0	9.40	4.11	66	19.83	20.73	1.90
42021	IC3562	220832	18.88	I	9.6	0.69	0.40	55	21.47	22.04	0.60
42064	NGC4567	7777	16.80	Sbc	4.0	3.68	2.52	48	19.55	19.97	2.14
42068	PGC042068	220837	7.00	Sb	2.8	1.41	0.83	55	22.67	23.25	0.86
42074	IC3576	7781	16.80	SBm	8.6	1.44	0.82	57	22.32	22.93	1.65
42081	IC3583	7784	8.51	IB	9.6	2.03	1.11	58	21.88	22.54	1.14
42089	NGC4569	7786	16.80	SABa	2.4	9.11	3.56	70	19.24	20.26	4.87
42100	NGC4571	7788	14.72	Sc	6.5	3.06	2.65	30	19.61	19.76	1.94
42108	IC3591	7790	16.80	I	9.8	1.39	0.76	58	21.83	22.48	1.35
42143	PGC042143	222314	6.72	S?	10.0	0.67	0.45	49	21.64	22.09	0.20
42160	PGC042160	220849	14.26	Sm	9.5	1.16	0.70	54	21.59	22.13	0.90
42169	UGC07795	7795	15.31	I	9.8	0.89	0.56	52	23.18	23.69	1.17
42174	NGC4580	7794	17.14	SABa	1.6	2.80	1.75	53	19.06	19.57	1.50
42223	NGC4584	7803	15.68	Sa	1.5	1.81	1.26	47	20.64	21.03	1.20

Table A.1 – continued

PGC (1)	Name (2)	AGC (3)	D (4)	T (5)	Tn (6)	a (7)	b (8)	inc (9)	μ_0 (10)	$\mu_{0,i}$ (11)	$R_{d,kpc}$ (13)
42307	IC3611	7817	15.59	S0-a	-1.0	1.73	0.85	62	21.38	22.15	1.25
42319	NGC4591	7821	31.50	Sb	3.3	1.87	1.01	59	19.55	20.22	1.76
42340	PGC042340	220883	15.40	Sd	8.0	1.07	0.59	58	20.93	21.58	0.66
42348	IC3617	7822	15.07	IB	9.9	1.51	0.66	66	21.02	21.91	0.94
42396	NGC4595	7826	12.76	SABb	3.8	1.97	1.32	49	19.45	19.88	0.79
42516	NGC4606	7839	15.68	SBa	0.6	2.51	1.25	62	20.02	20.79	1.82
42544	NGC4607	7843	12.47	SBbc	4.0	3.73	1.33	72	18.94	20.06	0.88
42688	NGC4630	7871	15.60	I	9.8	2.21	1.56	46	19.86	20.23	1.20
42699	NGC4633	7874	16.80	SABd	7.9	2.66	1.07	69	20.01	21.00	1.33
42707	NGC4634	7875	16.80	SBc	5.9	3.53	1.63	64	18.59	19.43	1.16
42710	PGC042710	220941	15.59	Sd	8.4	0.77	0.49	51	21.66	22.15	0.62
42741	NGC4639	7884	22.08	Sbc	3.5	2.47	1.77	45	19.13	19.49	1.78
42762	PGC042762	732245	28.00	(...)	(...)	0.65	0.57	28	22.32	22.46	1.11
42769	NGC4641	7889	15.68	S0	-2.0	1.41	1.12	38	22.19	22.44	1.96
42816	NGC4647	7896	16.29	SABc	5.2	3.43	2.53	43	19.29	19.62	2.21
42947	PGC042947	220987	15.40	Sd	8.4	0.64	0.55	32	21.18	21.36	0.43
42987	PGC042987	7930	14.30	S0-a	0.3	1.36	1.22	27	19.54	19.67	0.60
43001	IC3742	7932	21.28	SBc	5.0	1.78	0.79	65	20.52	21.39	1.51
43051	PGC043051	221000	9.15	S?	5.0	0.78	0.71	23	21.42	21.52	0.33
43056	PGC043056	221001	15.59	S?	8.5	0.74	0.57	41	22.54	22.83	0.86
43072	PGC043072	221004	6.91	S?	8.5	0.67	0.41	53	23.35	23.87	0.56
43106	UGC07943	7943	15.60	SBc	6.0	1.65	1.17	46	21.48	21.86	1.43
43186	NGC4689	7965	16.00	Sc	4.7	4.96	3.37	48	20.26	20.68	3.19
43189	NGC4688	7961	15.60	Sc	6.0	2.59	2.11	36	22.26	22.48	2.62
43205	PGC043205	222216	15.49	I	10.0	1.05	0.61	56	20.78	21.38	0.59

Table A.1 – continued

PGC	Name	AGC	D	T	Tn	a	b	inc	μ_0	$\mu_{0,i}$	$R_{d,kpc}$
(1)	(2)	(3)	(4)	(5)	(6)	(7)	(8)	(9)	(10)	(11)	(13)
43241	NGC4694	7969	16.80	S0	-2.0	3.47	1.37	69	21.36	22.37	3.51
43254	NGC4698	7970	27.29	Sab	1.7	6.26	3.20	61	20.75	21.48	7.35
43338	UGC07976	7976	23.10	SABd	8.0	0.88	0.47	59	22.06	22.73	1.14
43390	PGC043390	7983	8.77	I	9.9	0.62	0.48	40	22.73	23.01	0.44
43413	NGC4713	7985	15.63	Scd	6.8	2.53	1.68	49	18.87	19.31	1.11
43451	NGC4725	7989	12.59	SABa	2.2	11.18	8.53	41	19.74	20.03	4.03
43586	NGC4747	8005	14.30	SBcd	7.1	3.36	1.31	70	20.48	21.51	2.06
43595	PGC043595	223245	8.59	Sm	9.2	0.78	0.48	53	22.41	22.93	0.38
43775	NGC4765	8018	15.60	S0-a	0.0	1.48	1.01	48	20.04	20.45	0.78
43837	NGC4779	8022	35.20	SBc	4.6	1.93	1.75	25	19.76	19.87	2.31
43869	NGC4789A	8024	4.04	I	9.9	1.37	0.69	61	22.13	22.88	0.36
43907	PGC043907	8030	14.28	I	9.9	1.12	0.42	71	22.67	23.75	1.10
43950	NGC4791	221597	36.12	SBa	1.0	0.95	0.64	49	18.37	18.80	0.77
44008	UGC08042	8042	37.71	Sbc	4.1	1.08	0.64	55	21.36	21.93	2.00
44033	UGC08045	8045	39.48	IB	9.9	0.84	0.72	31	21.63	21.80	2.59
44086	NGC4808	8054	18.45	Sc	5.9	2.87	1.09	70	18.48	19.53	1.49
44089	UGC08053	8053	15.60	SABd	8.0	1.29	0.68	60	22.33	23.02	1.29
44125	UGC08056	8056	38.27	SBc	6.4	1.13	0.62	58	22.46	23.11	3.31
44215	PGC044215	222260	15.49	S?	10.0	1.02	0.60	55	20.59	21.16	0.52
44491	UGC08091	8091	2.18	I	9.8	0.93	0.50	59	22.37	23.04	0.15
44517	PGC044517	221245	28.84	IAB	10.0	1.02	0.70	48	21.79	22.20	1.40
44753	UGC08114	8114	29.77	Sb	2.8	0.85	0.64	42	22.04	22.35	1.20
45071	UGC08153	8153	23.10	Scd	6.6	1.61	1.58	10	22.75	22.76	2.19
45079	UGC08155	8155	42.79	Sab	2.2	1.60	1.33	34	22.30	22.50	5.57
45311	NGC4961	8185	40.55	SBc	5.6	1.52	1.10	44	20.00	20.35	2.04

Table A.1 – continued

PGC (1)	Name (2)	AGC (3)	D (4)	T (5)	Tn (6)	a (7)	b (8)	inc (9)	μ_0 (10)	$\mu_{0,i}$ (11)	$R_{d,kpc}$ (13)
45370	PGC045370	230077	15.49	I	9.7	0.92	0.53	56	22.10	22.70	0.88
45836	NGC5016	8279	40.20	SABb	4.4	1.57	1.14	44	19.35	19.69	2.38
45858	PGC045858	230161	9.33	SBcd	7.3	1.53	0.72	64	20.44	21.26	0.56
45875	PGC045875	8285	15.68	Sd	8.0	1.60	0.62	70	21.22	22.25	1.00
45931	UGC08298	8298	11.80	I	9.9	0.87	0.73	33	21.71	21.89	0.50
46159	UGC08333	8333	21.88	I	9.7	1.28	0.50	70	22.75	23.79	1.90
46241	PGC046241	8345	15.59	Sbc	4.5	1.11	0.84	41	20.23	20.53	0.58
46387	PGC046387	8363	35.84	IB	9.9	0.88	0.62	46	21.75	22.14	1.58
46556	PGC046556	8382	15.68	IB	9.9	0.98	0.55	57	21.79	22.43	0.91
46563	UGC08385	8385	15.12	Sm	9.0	1.85	0.96	60	21.44	22.16	1.30
47101	PGC047101	8450	15.21	I	9.9	0.85	0.59	47	21.79	22.19	0.66
47826	PGC047826	230436	13.93	I	10.0	1.04	0.67	51	22.06	22.54	0.79
48046	PGC048046	232025	13.91	S?	10.0	0.89	0.53	54	22.93	23.48	0.90
48122	UGC08614	8614	12.70	I	9.9	2.21	1.20	59	21.74	22.40	1.64
48130	NGC5248	8616	13.00	SABb	4.0	10.66	6.39	54	19.52	20.07	2.67
48212	UGC08629	8629	15.21	I	9.8	1.09	0.44	69	21.94	22.93	0.77
48280	PGC048280	8638	4.29	I	9.9	0.89	0.65	44	21.63	21.98	0.28
48959	NGC5300	8727	18.45	SABc	5.2	4.13	3.38	35	20.53	20.75	3.10
49353	NGC5338	8800	12.76	S0	-2.0	2.24	1.06	63	20.72	21.53	1.15
49513	NGC5360	8838	15.20	S0-a	0.1	2.06	0.90	66	22.11	23.01	1.95
49547	NGC5363	8847	15.20	S0-a	0.4	3.92	2.54	50	19.67	20.14	3.35
50194	UGC08995	8995	21.88	SABc	7.4	2.06	0.73	72	21.66	22.79	2.44
50597	PGC050597	241261	34.91	Sbc	4.4	0.90	0.56	53	21.20	21.72	1.22
50599	PGC050599	241411	33.79	S?	1.6	0.97	0.62	51	19.19	19.68	0.87
51233	NGC5566	9175	23.50	SBab	1.6	4.95	1.96	69	19.52	20.53	4.98

Table A.1 – continued

PGC (1)	Name (2)	AGC (3)	D (4)	T (5)	Tn (6)	a (7)	b (8)	inc (9)	μ_0 (10)	$\mu_{0,i}$ (11)	$R_{d,kpc}$ (13)
51241	NGC5569	9176	23.50	SABc	5.8	1.21	1.06	29	22.39	22.53	2.55
51332	NGC5587	9202	33.79	S0-a	-0.1	2.36	0.89	71	18.53	19.59	1.94
51351	UGC09206	9206	33.60	Sbc	3.8	1.31	0.76	56	20.32	20.91	1.62
51401	PGC051401	240313	32.48	Sbc	3.8	1.03	0.73	45	20.66	21.03	1.48
51422	NGC5600	9220	33.88	Sc	4.8	1.65	1.57	18	18.61	18.66	1.55
51449	PGC051449	9225	20.63	Sm	9.0	1.03	0.50	62	21.42	22.19	0.94
51604	PGC051604	9252	24.36	I	9.9	1.00	0.50	62	21.88	22.63	1.09
51664	UGC09273	9273	11.22	I	9.8	1.10	0.61	58	21.26	21.89	0.54
51685	IC1014	9275	21.28	SABd	8.1	2.22	1.22	58	21.32	21.97	2.62
51846	NGC5645	9328	15.14	SBcd	6.6	2.49	1.40	57	20.16	20.79	1.50
51912	PGC051912	240431	52.00	S?	3.0	0.90	0.48	59	20.47	21.15	1.50
51921	NGC5661	9346	48.53	Sb	3.2	1.75	0.79	65	19.60	20.47	2.46
51953	NGC5665	9352	18.20	SABc	5.0	2.38	1.49	52	19.24	19.74	1.30
51984	UGC09356	9356	32.67	Sc	4.6	1.50	0.83	58	19.63	20.27	1.45
51995	PGC051995	9360	29.50	Scd	6.5	1.20	0.95	38	18.81	19.06	0.99
52016	UGC09364	9364	31.45	SBd	7.8	1.63	0.89	58	21.21	21.87	1.83
52018	NGC5668	9363	23.50	Scd	6.9	3.79	3.18	33	20.85	21.04	3.12
52092	UGC09380	9380	23.50	I	9.9	2.54	1.63	51	22.45	22.94	1.58
52141	UGC09385	9385	19.80	I	9.7	0.84	0.76	26	22.93	23.05	1.06
52212	PGC052212	240523	26.97	Sc	5.0	0.78	0.62	38	22.13	22.39	1.14
52365	NGC5701	9436	19.80	S0-a	-0.4	5.54	5.18	21	19.83	19.91	2.88
52689	UGC09500	9500	29.00	Sm	8.8	1.34	0.50	71	23.58	24.65	4.16
52819	PGC052819	240700	27.81	S?	9.0	0.55	0.48	30	20.28	20.44	0.47
52887	NGC5762	9535	27.35	Sab	2.0	2.00	1.60	37	22.92	23.16	3.32
53512	PGC053512	241727	25.48	Sc	4.9	0.57	0.50	29	20.55	20.69	0.51

Table A.1 – continued

PGC	Name	AGC	D	T	Tn	a	b	inc	μ_0	$\mu_{0,i}$	$R_{d,kpc}$
(1)	(2)	(3)	(4)	(5)	(6)	(7)	(8)	(9)	(10)	(11)	(13)
54084	PGC054084	9739	22.59	SBd	7.9	1.03	0.44	67	21.18	22.11	0.92
54849	NGC5921	9824	14.00	Sbc	4.0	5.43	4.83	27	20.10	20.22	2.13
55308	PGC055308	252085	27.44	Sbc	4.2	0.76	0.72	19	22.00	22.06	1.17
55482	NGC5954	9904	25.50	SABc	6.0	1.67	0.92	58	18.66	19.32	1.20
55501	NGC5956	9908	26.30	Sc	5.9	1.46	1.40	17	19.43	19.48	1.22
55520	NGC5957	9915	26.30	Sb	3.0	3.17	2.44	40	20.08	20.36	2.54
55637	NGC5964	9935	27.80	SBcd	6.9	5.68	4.69	35	20.79	21.00	4.38
55660	PGC055660	9941	29.80	I	9.8	1.11	0.82	43	22.71	23.04	2.21
55665	NGC5970	9943	28.18	SBc	5.0	2.92	1.60	58	18.82	19.48	2.46
55710	UGC09951	9951	30.52	SABc	6.6	1.17	0.64	58	22.71	23.37	2.37
55965	UGC10009	10009	30.61	I	9.8	0.87	0.61	46	22.74	23.12	1.91
55967	IC4582	10021	37.30	SBbc	4.1	1.55	0.64	68	18.47	19.43	1.40
55975	UGC10014	10014	38.90	IAB	9.8	1.05	1.00	18	22.95	23.00	2.51
55989	UGC10023	10023	29.65	I	9.8	0.94	0.64	48	21.73	22.15	1.47
56110	PGC056110	251262	64.27	Sa	1.3	0.88	0.58	49	20.09	20.52	1.61
56111	UGC10041	10041	28.84	Sd	7.9	2.15	0.91	67	21.99	22.93	4.40
56142	PGC056142	252481	33.41	S?	5.0	0.58	0.46	39	21.36	21.63	0.91
56168	UGC10058	10058	37.30	SBm	8.7	0.91	0.69	41	22.79	23.09	1.72
56334	NGC6012	10083	28.65	SBab	1.7	2.40	2.15	26	21.46	21.58	3.96
57120	PGC057120	261969	21.84	Scd	7.0	0.86	0.41	64	20.93	21.74	0.65
57169	PGC057169	261313	26.79	Sm	9.0	0.99	0.65	50	22.25	22.70	1.68
57205	NGC6063	10210	40.36	Sc	5.9	1.48	0.83	57	18.95	19.58	2.04
57799	NGC6106	10328	24.32	Sc	5.3	2.36	1.20	61	19.45	20.19	1.98
67421	UGC11820	11820	16.99	SABm	8.7	0.69	0.63	24	22.34	22.44	0.71
67759	UGC11866	11866	25.11	SABc	7.0	0.88	0.71	37	21.35	21.58	1.05

Table A.1 – continued

PGC (1)	Name (2)	AGC (3)	D (4)	T (5)	Tn (6)	a (7)	b (8)	inc (9)	μ_0 (10)	$\mu_{0,i}$ (11)	$R_{d,kpc}$ (13)
68046	PGC068046	11908	25.85	Sm	9.4	0.96	0.73	41	21.97	22.27	1.51
68096	NGC7217	11914	14.93	Sab	2.5	4.57	3.89	32	19.78	19.95	3.35
68163	UGC11921	11921	24.45	IB	9.9	1.86	0.74	69	21.05	22.05	1.89
68870	NGC7280	12035	24.32	S0-a	-1.3	2.30	1.43	53	19.07	19.59	1.71
68878	PGC068878	320215	24.30	I	9.7	1.04	0.99	17	22.09	22.14	1.54
68922	NGC7286	12043	12.90	S0-a	0.2	1.74	0.77	66	19.53	20.42	0.64
68941	NGC7292	12048	12.90	I	9.9	2.33	1.79	40	20.27	20.55	1.01
69212	UGC12090	12090	26.69	I	9.8	1.04	0.50	63	20.95	21.75	1.10
69844	UGC12212	12212	24.30	Sm	8.8	1.12	0.80	45	22.74	23.10	2.27
70131	NGC7437	12270	26.50	SABc	6.7	1.84	1.79	13	20.53	20.56	1.94
70213	NGC7448	12294	28.18	Sc	5.0	2.59	1.32	61	18.08	18.81	1.78
70275	UGC12311	12311	13.72	Sbc	4.4	1.50	0.63	67	21.20	22.13	0.85
70291	NGC7463	12316	22.91	SABb	3.1	1.96	0.81	68	19.21	20.16	1.35
70295	PGC070295	12317	26.50	S0	-1.8	1.70	1.20	46	22.92	23.30	3.93
70404	UGC12340	12340	15.40	Sd	8.0	0.88	0.46	60	20.99	21.70	0.54
70633	IC1473	12404	12.41	S0	-2.0	1.87	1.08	56	20.35	20.95	0.83
71538	UGC12613	12613	1.21	I	9.8	6.50	3.51	59	22.77	23.44	0.42
71973	UGC12713	12713	11.39	Sa	0.5	1.06	0.70	49	21.13	21.58	0.56
72087	UGC12732	12732	15.10	SABm	8.7	1.91	1.82	18	22.53	22.59	2.10
73177	NGC7800	12885	23.05	I	9.8	3.21	2.24	46	21.27	21.66	2.38
84268	PGC084268	249303	26.69	Sc	4.8	0.60	0.42	47	21.01	21.40	0.57
85276	PGC085276	748716	27.35	(...)	(...)	0.77	0.47	53	20.01	20.53	0.62
86806	PGC086806	122226	7.99	Sc	4.8	0.95	0.58	53	22.21	22.74	0.47
87128	PGC087128	242165	13.63	I	9.7	1.04	0.66	51	21.40	21.89	0.62
87175	PGC087175	242016	27.44	I	10.0	1.09	0.52	63	23.89	24.70	2.91

Table A.1 – continued

PGC (1)	Name (2)	AGC (3)	D (4)	T (5)	Tn (6)	a (7)	b (8)	inc (9)	μ_0 (10)	$\mu_{0,i}$ (11)	$R_{d,kpc}$ (13)
138451	PGC138451	110482	7.20	I	10.0	0.70	0.48	47	22.21	22.61	0.28
1263558	PGC1263558	219197	24.17	(...)	(...)	0.69	0.53	41	21.62	21.92	0.74
1267592	PGC1267592	224304	37.24	(...)	(...)	0.73	0.51	47	23.20	23.59	1.99
1331483	PGC1331483	181770	29.12	S?	5.0	0.47	0.40	33	20.14	20.32	0.43
1346685	PGC1346685	227861	15.49	(...)	(...)	0.69	0.48	46	20.94	21.33	0.41
1360237	PGC1360237	714204	26.69	(...)	(...)	0.58	0.41	47	20.84	21.23	0.59
1371096	PGC1371096	202218	18.29	(...)	(...)	0.67	0.43	51	21.46	21.94	0.54
1424345	PGC1424345	201963	10.36	I	10.0	0.57	0.46	37	20.91	21.14	0.21
1448560	PGC1448560	215137	9.99	(...)	(...)	0.75	0.40	59	21.41	22.09	0.30
1462017	PGC1462017	748866	12.13	(...)	(...)	0.80	0.59	43	21.19	21.52	0.42
1468320	PGC1468320	112457	26.23	S?	3.0	0.68	0.59	31	21.02	21.18	0.67
1505120	PGC1505120	257943	31.92	(...)	(...)	0.57	0.46	37	22.07	22.31	0.87
1697033	PGC1697033	739497	20.25	(...)	(...)	0.65	0.60	22	20.34	20.43	0.44
1726175	PGC1726175	238890	6.35	(...)	(...)	0.63	0.44	46	21.69	22.07	0.18
1742964	PGC1742964	122863	34.63	(...)	(...)	0.69	0.55	37	20.99	21.22	0.97
1800124	PGC1800124	122212	12.41	Sc	4.8	0.81	0.44	58	21.22	21.87	0.40
2801023	PGC2801023	252522	26.41	Sm	9.0	0.82	0.71	31	22.63	22.79	0.97
3466489	PGC3466489	203709	7.28	(...)	(...)	0.80	0.50	52	21.99	22.49	0.27
3723606	PGC3723606	171559	31.45	(...)	(...)	0.71	0.60	32	20.28	20.46	0.71
3850707	PGC3850707	257929	27.35	(...)	(...)	0.57	0.47	35	20.69	20.90	0.55
4004996	PGC4004996	242618	25.85	(...)	(...)	0.65	0.48	42	22.39	22.70	0.99
4112990	PGC4112990	714055	21.19	(...)	(...)	0.90	0.64	46	23.50	23.87	1.34
4668301	PGC4668301	193813	28.28	(...)	(...)	0.66	0.52	39	21.91	22.17	0.85
5057570	PGC5057570	174656	29.59	(...)	(...)	0.65	0.40	53	19.55	20.07	0.44
5057575	PGC5057575	193816	22.20	(...)	(...)	0.91	0.54	55	24.33	24.90	2.34

Table A.1 – continued

PGC (1)	Name (2)	AGC (3)	D (4)	T (5)	Tn (6)	a (7)	b (8)	inc (9)	μ_0 (10)	$\mu_{0,i}$ (11)	$R_{d,kpc}$ (13)
5058796	PGC5058796	749463	18.57	(...)	(...)	0.99	0.41	68	22.68	23.65	1.04
5058884	PGC5058884	123038	19.04	(...)	(...)	0.47	0.42	25	19.57	19.68	0.24
5058897	PGC5058897	122424	19.04	(...)	(...)	0.60	0.41	48	22.74	23.16	0.93
5059667	PGC5059667	122880	22.68	(...)	(...)	0.62	0.51	36	22.60	22.83	0.97
5060003	PGC5060003	215287	16.33	(...)	(...)	1.14	0.46	69	21.30	22.29	0.72

NOTE: (1) PGC number. (2) Principal name. (3) ALFALFA galaxy number. (4) Distance, (5) Hubble morphological type, (6) Numerical morphological type. (7) Major axis measured at isophot $\mu_{[3,4]}^i = 25.5$ mag arcsec⁻². (8) Minor axis. (9) Inclination. (10) Central surface brightness of the disk WISE W1 3.4 μ m. (11) Central surface brightness of the disk, corrected for inclination. (12) Scale length in kpc.

Table A.2: Photometry, mass, and star-formation rate of the
WISE galaxy sample

PGC	Name	u'	g'	r'	i'	z'	W1	W2	W3	W4	NUV	FUV	M_\star	M_{HI}	SFR_{FUV}
(1)	(2)	(3)	(4)	(5)	(6)	(7)	(8)	(9)	(10)	(11)	(12)	(13)	(14)	(15)	(16)
218	NGC7814	12.62	10.87	10.02	9.54	9.24	9.53	10.16	10.76	(...)	15.84	17.75	10.64	8.99	7.0×10^0
255	UGC00017	15.94	14.86	14.44	14.29	14.31	15.14	15.88	(...)	(...)	16.75	16.97	9.01	8.81	8.1×10^{-2}
647	NGC0014	13.28	12.41	12.00	11.72	11.70	12.44	13.19	12.68	(...)	(...)	(...)	8.79	8.14	(...)
697	PGC000697	16.64	15.72	15.41	15.25	15.17	16.27	16.79	(...)	(...)	(...)	(...)	7.66	7.88	(...)
878	PGC000878	15.07	14.05	13.68	13.45	13.33	14.14	14.71	13.47	(...)	15.93	(...)	9.18	9.08	(...)
2216	PGC002216	15.71	15.02	14.81	14.72	14.68	15.60	16.44	(...)	(...)	16.18	16.37	9.14	9.00	2.1×10^{-1}
5974	NGC0628	10.48	9.42	8.95	8.73	8.60	9.11	9.65	8.10	7.74	11.38	11.83	10.12	9.79	2.3×10^0
6150	UGC01171	16.72	15.72	15.41	15.21	15.28	16.19	16.84	(...)	(...)	17.93	18.35	7.55	7.47	5.3×10^{-3}
6174	UGC01176	14.75	13.60	13.40	13.12	13.05	14.35	14.71	(...)	(...)	15.39	15.69	7.72	8.84	6.1×10^{-2}
6364	UGC01211	16.22	14.97	14.45	14.13	14.05	14.79	15.64	(...)	(...)	17.24	17.53	9.92	9.04	1.4×10^{-1}
7841	UGC01551	14.02	13.09	12.65	12.42	12.27	12.96	13.48	12.34	(...)	15.00	15.18	9.93	9.75	1.0×10^0
7849	NGC0803	13.64	12.55	12.07	11.76	11.62	12.15	12.72	11.68	(...)	14.79	15.13	9.87	9.61	7.8×10^{-1}
7871	UGC01561	14.95	13.82	13.36	13.11	12.90	14.04	14.70	(...)	(...)	16.24	16.59	8.60	7.89	4.3×10^{-2}
8535	UGC01711	16.78	15.62	15.16	14.93	14.80	15.65	16.15	(...)	(...)	17.80	18.05	8.75	8.80	9.0×10^{-2}
9403	PGC009403	16.11	15.14	14.74	14.54	14.44	15.22	15.90	(...)	(...)	17.23	17.65	9.37	8.79	2.6×10^{-1}
9447	UGC01958	(...)	(...)	(...)	(...)	(...)	15.74	16.46	(...)	(...)	16.84	17.07	8.70	8.77	7.4×10^{-2}
9705	UGC02017	(...)	(...)	(...)	(...)	(...)	16.44	17.04	(...)	(...)	17.81	18.70	8.32	9.33	2.6×10^{-1}
9788	NGC0972	(...)	(...)	(...)	(...)	(...)	10.10	10.53	(...)	7.64	14.91	(...)	10.09	8.99	(...)
10051	NGC1012	13.33	12.20	11.68	11.47	11.34	11.78	12.29	10.92	9.96	(...)	(...)	9.97	9.80	(...)
10272	NGC1056	13.69	12.52	11.82	11.39	11.25	11.41	11.92	10.31	9.72	(...)	(...)	10.31	9.80	(...)
11329	NGC1156	(...)	(...)	(...)	(...)	(...)	11.42	11.89	10.84	9.50	12.69	12.99	8.52	8.48	2.1×10^{-1}
20981	PGC020981	(...)	(...)	(...)	(...)	(...)	15.63	16.22	(...)	(...)	(...)	(...)	8.24	8.20	(...)

Table A.2 – continued

PGC (1)	Name (2)	u' (3)	g' (4)	r' (5)	i' (6)	z' (7)	W1 (8)	W2 (9)	W3 (10)	W4 (11)	FUV (12)	NUV (13)	M_{\star} (14)	M_{HI} (15)	SFR _{FUV} (16)
21120	UGC03876	14.18	13.13	12.68	12.42	12.29	13.04	13.74	(...)	(...)	(...)	(...)	9.76	9.41	(...)
21303	PGC021303	(...)	(...)	(...)	(...)	(...)	13.79	14.17	13.63	(...)	(...)	(...)	8.62	8.87	(...)
22277	UGC04115	15.06	14.33	14.08	13.81	13.86	14.52	14.86	(...)	(...)	15.45	15.65	7.41	8.53	3.8×10^{-2}
23214	IC2256	15.42	14.45	14.03	13.83	13.72	14.34	15.01	13.78	(...)	(...)	(...)	9.56	9.03	(...)
23283	PGC023283	16.23	15.39	15.13	14.99	14.82	15.77	16.30	(...)	(...)	(...)	(...)	8.96	8.89	(...)
23559	PGC023559	14.74	13.82	13.53	13.36	13.33	14.14	14.85	(...)	(...)	15.39	15.77	9.48	9.42	8.5×10^{-1}
23646	IC2361	15.49	14.21	13.62	13.32	13.20	13.49	14.09	12.81	(...)	(...)	(...)	9.70	8.53	(...)
23707	UGC04418	16.05	15.13	14.70	14.52	14.37	15.38	16.10	(...)	(...)	17.01	17.43	9.36	9.00	3.3×10^{-1}
23762	PGC023762	15.01	13.88	13.42	13.15	13.03	13.67	14.22	12.83	(...)	15.94	16.41	9.62	8.45	7.5×10^{-1}
24012	PGC024012	15.47	14.61	14.25	14.06	13.95	14.74	15.25	13.84	(...)	16.20	16.59	9.31	9.03	5.1×10^{-1}
24425	NGC2644	14.31	13.18	12.66	12.39	12.21	12.61	13.15	11.69	11.25	(...)	(...)	10.05	9.29	(...)
24457	PGC024457	14.78	13.95	13.64	13.46	13.38	14.16	14.83	(...)	(...)	15.50	15.76	9.56	9.37	6.2×10^{-1}
24469	PGC024469	15.45	14.41	13.91	13.68	13.51	14.38	14.82	13.47	(...)	16.77	17.16	9.06	8.76	2.9×10^{-1}
24666	PGC024666	16.84	15.76	15.34	15.11	14.97	15.81	16.32	(...)	(...)	17.74	18.09	8.84	8.66	1.1×10^{-1}
24699	UGC04599	14.99	13.57	13.05	12.71	12.62	13.32	14.11	(...)	(...)	16.01	16.28	10.03	10.10	4.0×10^{-1}
25332	PGC025332	14.97	14.04	13.64	13.43	13.31	13.94	14.54	12.97	(...)	15.84	16.26	9.61	9.15	7.0×10^{-1}
25376	NGC2731	14.41	13.44	12.95	12.71	12.57	12.77	13.17	11.09	10.20	15.53	16.09	9.42	8.57	1.0×10^0
25399	NGC2735	14.64	13.45	12.74	12.30	12.12	12.28	12.85	11.80	(...)	16.28	16.69	10.37	9.78	6.0×10^{-1}
25496	NGC2743	14.90	13.72	13.20	12.91	12.77	13.19	13.76	12.31	(...)	16.04	16.55	9.95	9.01	1.4×10^0
25525	NGC2750	13.21	12.34	11.92	11.66	11.61	11.91	12.53	10.55	9.54	14.36	14.72	10.59	9.95	4.6×10^0
25556	UGC04781	15.28	14.71	14.47	14.34	14.15	15.02	15.43	(...)	(...)	16.09	16.34	8.40	9.44	2.6×10^{-1}
25679	UGC04797	15.39	14.22	13.77	13.50	13.38	14.04	14.33	(...)	(...)	16.29	16.70	8.39	8.85	1.9×10^{-1}
25861	NGC2775	11.61	10.27	9.53	9.09	8.92	9.37	10.03	9.95	10.05	13.69	14.93	11.21	8.61	1.9×10^1
25876	PGC025876	14.70	13.85	13.58	13.43	13.32	14.03	14.55	13.05	(...)	15.39	15.77	9.14	9.12	5.2×10^{-1}
26218	UGC04902	14.78	13.54	13.06	12.78	12.66	13.28	13.82	12.43	11.12	16.13	16.77	9.43	8.27	7.0×10^{-1}

Table A.2 – continued

PGC (1)	Name (2)	u' (3)	g' (4)	r' (5)	i' (6)	z' (7)	W1 (8)	W2 (9)	W3 (10)	W4 (11)	FUV (12)	NUV (13)	M_{\star} (14)	M_{HI} (15)	SFR _{FUV} (16)
26453	PGC026453	15.73	14.91	14.52	14.23	14.27	15.06	15.58	(...)	(...)	16.56	17.02	8.74	8.71	1.7×10^{-1}
26570	PGC026570	15.71	14.78	14.47	14.27	14.21	14.80	15.56	(...)	(...)	16.25	16.51	9.80	9.09	4.2×10^{-1}
26781	NGC2882	14.38	13.14	12.55	12.22	12.04	12.44	13.02	11.54	11.24	15.83	16.55	10.14	9.06	2.2×10^0
26932	NGC2894	14.05	12.56	11.89	11.45	11.23	11.59	12.20	11.64	(...)	16.12	16.82	10.93	10.03	3.4×10^0
27074	NGC2906	14.00	12.62	11.95	11.58	11.33	11.61	12.20	11.11	11.01	15.37	16.05	10.76	9.36	4.8×10^0
27228	PGC027228	15.88	14.86	14.46	14.25	14.20	15.10	15.68	(...)	(...)	16.83	17.26	8.35	8.22	4.8×10^{-2}
27232	NGC2919	14.33	13.20	12.65	12.36	12.17	12.52	13.01	11.64	11.46	15.55	16.05	10.14	9.44	2.1×10^0
27622	PGC027622	15.60	14.83	14.57	14.46	14.37	15.21	15.82	(...)	(...)	16.17	16.39	8.73	8.48	1.4×10^{-1}
27635	NGC2962	14.05	12.20	11.43	11.06	10.78	11.21	11.95	12.89	(...)	16.68	17.27	10.94	9.03	5.2×10^{-1}
27734	NGC2966	14.31	12.93	12.29	11.95	11.77	11.90	12.35	10.47	9.29	15.68	16.21	10.14	9.35	1.4×10^0
27910	IC0559	15.04	14.03	13.66	13.47	13.38	14.44	15.07	(...)	(...)	16.18	16.61	8.29	8.06	4.5×10^{-2}
28296	NGC3020	13.22	12.55	12.32	12.22	12.23	12.85	13.36	11.98	10.81	13.71	13.92	9.31	9.63	1.5×10^0
28324	NGC3024	14.21	13.45	13.10	12.92	12.86	13.31	13.74	12.33	(...)	14.94	15.31	8.96	9.40	5.3×10^{-1}
28378	PGC028378	14.73	13.94	13.57	13.40	13.34	14.25	14.77	(...)	(...)	15.59	15.84	8.11	8.44	2.5×10^{-2}
28590	NGC3049	13.80	12.83	12.33	12.07	11.93	12.42	12.96	11.19	9.69	14.78	15.24	9.68	9.08	8.7×10^{-1}
28617	NGC3055	13.31	12.29	11.86	11.66	11.54	11.88	12.27	10.33	9.54	14.32	14.76	9.89	9.34	2.4×10^0
28627	PGC028627	15.73	14.78	14.38	14.18	14.17	15.11	15.58	(...)	(...)	16.66	17.03	8.71	8.56	1.2×10^{-1}
28682	PGC028682	14.51	13.58	13.00	12.76	12.52	12.59	12.98	10.66	10.05	15.81	16.16	9.40	9.16	4.6×10^{-1}
28913	UGC05373	11.86	11.45	11.14	10.92	10.88	11.92	12.14	(...)	(...)	13.46	13.78	6.64	7.54	1.0×10^{-2}
29009	NGC3094	14.07	12.87	12.28	11.98	11.81	10.88	10.04	(...)	8.02	15.40	16.04	7.79	9.77	4.2×10^0
29198	PGC029198	16.23	15.29	14.97	14.80	14.78	15.63	16.29	(...)	(...)	16.92	17.23	8.54	7.86	7.7×10^{-2}
29408	PGC029408	15.79	14.64	14.28	14.07	13.97	15.01	15.68	(...)	(...)	(...)	(...)	(...)	8.00	(...)
29413	UGC05454	16.19	15.25	15.08	14.94	14.85	15.77	16.30	(...)	(...)	(...)	(...)	(...)	8.83	(...)
29428	UGC05456	14.08	13.28	13.04	12.91	12.90	13.66	14.25	13.76	(...)	14.72	15.09	8.21	7.80	5.1×10^{-2}
29435	IC0591	14.71	13.83	13.42	13.25	13.17	13.62	14.08	12.34	(...)	(...)	(...)	9.40	8.72	(...)

Table A.2 – continued

PGC (1)	Name (2)	u' (3)	g' (4)	r' (5)	i' (6)	z' (7)	W1 (8)	W2 (9)	W3 (10)	W4 (11)	FUV (12)	NUV (13)	M_{\star} (14)	M_{HI} (15)	SFR _{FUV} (16)
29747	NGC3153	14.06	13.11	12.74	12.53	12.45	12.99	13.51	12.36	(...)	(...)	(...)	9.96	9.75	(...)
29835	UGC05522	13.98	13.39	13.13	12.99	12.98	13.82	14.38	(...)	(...)	14.76	14.99	9.59	10.21	2.3×10^0
30042	PGC030042	16.34	15.57	15.30	15.15	15.14	16.26	16.14	(...)	(...)	17.22	17.56	6.53	8.81	7.1×10^{-2}
30263	PGC030263	14.79	13.85	13.39	13.13	13.06	13.38	13.88	11.92	(...)	15.68	16.13	9.32	8.74	6.7×10^{-1}
30531	UGC05633	14.86	13.80	13.42	13.19	13.16	13.95	14.35	(...)	(...)	(...)	(...)	8.94	9.55	(...)
30684	NGC3246	14.17	13.15	12.83	12.61	12.53	13.18	13.68	12.88	(...)	14.97	15.40	9.74	9.85	2.2×10^0
30773	PGC030773	16.29	15.29	14.95	14.77	14.82	15.58	16.21	(...)	(...)	16.72	17.04	8.68	8.50	9.5×10^{-2}
31081	PGC031081	16.14	14.95	14.88	14.68	14.01	16.19	17.05	(...)	(...)	16.57	16.71	8.99	9.17	7.3×10^{-2}
31122	NGC3274	13.58	12.83	12.54	12.42	12.31	13.24	13.80	13.15	(...)	14.15	14.44	8.49	8.93	1.4×10^{-1}
31387	PGC031387	15.55	14.68	14.28	14.07	13.99	14.58	15.18	(...)	(...)	16.42	16.80	9.04	8.42	1.9×10^{-1}
31442	NGC3299	14.29	13.02	12.47	12.18	12.04	12.76	13.50	(...)	(...)	15.79	16.34	9.44	8.06	1.4×10^{-1}
31528	NGC3306	14.58	13.61	13.10	12.83	12.64	12.66	13.08	11.01	10.41	15.59	15.95	9.97	9.76	1.8×10^0
31610	PGC031610	15.19	14.23	13.84	13.61	13.55	14.19	14.72	(...)	(...)	(...)	(...)	8.56	8.42	(...)
31877	PGC031877	16.75	15.52	15.08	14.87	14.88	15.59	16.01	(...)	(...)	17.84	19.27	7.49	7.48	1.6×10^{-1}
31883	NGC3338	12.23	11.14	10.68	10.40	10.26	10.68	11.21	9.68	9.50	13.26	13.63	10.54	10.18	4.1×10^0
31930	UGC05832	14.29	13.41	13.05	12.88	12.80	13.51	14.10	13.00	(...)	15.01	15.39	9.18	8.71	4.0×10^{-1}
31937	PGC031937	16.64	15.79	15.47	15.30	15.07	16.27	16.93	(...)	(...)	17.33	17.50	8.29	8.44	2.7×10^{-2}
31968	NGC3344	10.87	10.05	9.54	9.27	9.04	9.66	10.22	8.92	8.51	12.13	12.50	10.14	9.60	2.0×10^0
31982	NGC3346	13.04	11.96	11.49	11.24	11.10	11.59	12.16	10.70	10.41	14.18	14.64	10.07	9.29	1.8×10^0
32007	NGC3351	11.32	10.00	9.33	8.98	8.76	9.14	9.82	8.67	7.31	12.73	13.31	10.75	9.13	2.3×10^0
32192	NGC3368	10.74	9.57	8.85	8.47	8.21	8.66	9.19	5.25	5.43	13.44	14.09	10.69	9.31	1.4×10^0
32226	NGC3377A	14.88	13.69	13.24	12.95	12.93	13.69	14.45	(...)	(...)	15.99	16.30	8.88	8.04	3.4×10^{-2}
32257	PGC032257	15.58	14.76	14.46	14.28	14.29	14.78	15.30	(...)	(...)	16.06	16.34	9.18	9.12	6.9×10^{-1}
32306	NGC3389	(...)	(...)	(...)	(...)	(...)	11.84	12.35	10.65	10.05	13.79	14.28	9.77	9.43	2.6×10^0
32345	PGC032345	16.67	15.74	15.37	15.14	14.92	15.69	16.36	(...)	(...)	(...)	(...)	8.55	8.08	(...)

Table A.2 – continued

PGC (1)	Name (2)	u' (3)	g' (4)	r' (5)	i' (6)	z' (7)	W1 (8)	W2 (9)	W3 (10)	W4 (11)	FUV (12)	NUV (13)	M_* (14)	M_{HI} (15)	SFR _{FUV} (16)
32346	PGC032346	16.07	15.37	15.23	15.23	15.05	16.06	16.61	(...)	(...)	16.43	16.63	8.11	8.60	6.7×10^{-2}
32347	NGC3391	14.59	13.78	13.51	13.33	13.33	13.92	14.39	13.02	(...)	15.16	15.62	9.85	9.72	3.5×10^0
32364	UGC05923	15.29	14.18	13.64	13.34	13.18	13.97	14.46	(...)	(...)	16.75	17.32	9.31	8.67	2.2×10^{-1}
32368	UGC05921	15.50	14.54	14.13	13.93	13.94	14.61	15.44	(...)	(...)	16.39	16.85	9.70	9.02	3.5×10^{-1}
32496	UGC05948	16.52	15.75	15.50	14.87	14.99	13.92	14.54	(...)	(...)	17.18	17.52	8.99	8.26	2.0×10^{-2}
32529	NGC3423	12.17	11.17	10.82	10.65	10.44	11.11	11.70	9.95	9.51	13.00	13.42	10.04	9.40	3.1×10^0
32533	NGC3414	12.95	11.33	10.58	10.17	9.93	10.40	11.03	12.10	(...)	15.94	17.42	10.89	8.33	7.2×10^0
32549	NGC3418	14.96	13.46	12.80	12.45	12.29	12.83	13.46	13.49	(...)	17.26	18.26	9.92	8.05	5.4×10^{-1}
32570	UGC05974	14.96	14.09	13.77	13.60	13.61	14.53	14.88	(...)	(...)	15.59	15.88	8.42	9.38	3.9×10^{-1}
32605	NGC3433	13.69	12.30	11.81	11.54	11.51	11.90	12.57	11.44	(...)	(...)	(...)	10.58	9.88	(...)
32708	UGC06014	15.87	14.90	14.55	14.35	14.29	15.04	15.48	(...)	(...)	16.70	17.04	7.78	7.98	2.7×10^{-2}
32754	NGC3451	13.99	13.09	12.63	12.41	12.28	12.72	13.25	11.46	10.94	15.00	15.48	9.72	9.19	1.6×10^0
33140	NGC3485	13.40	12.31	11.79	11.53	11.45	11.91	12.61	11.05	(...)	14.37	14.65	10.23	9.55	9.3×10^{-1}
33160	NGC3489	12.05	10.67	10.02	9.68	9.46	9.96	10.58	11.08	11.44	14.90	16.81	10.35	7.39	1.3×10^1
33371	NGC3504	12.56	11.42	10.85	10.54	10.36	10.54	10.91	8.74	7.59	13.72	14.33	10.37	8.89	6.1×10^0
33432	NGC3512	13.78	12.70	12.18	11.89	11.76	12.11	12.44	11.09	10.89	14.61	14.95	9.81	9.09	1.3×10^0
33447	PGC033447	16.56	15.60	15.27	15.09	15.00	16.42	17.10	(...)	(...)	17.33	17.60	7.84	7.76	1.2×10^{-2}
33463	UGC06138	15.79	14.77	14.39	14.05	14.13	14.90	15.22	(...)	(...)	16.27	16.52	8.95	9.63	4.6×10^{-1}
33642	UGC06169	15.29	14.18	13.63	13.33	13.13	13.59	14.23	13.00	(...)	16.46	16.93	9.40	9.14	1.9×10^{-1}
33652	PGC033652	16.49	15.52	15.10	14.89	14.75	15.48	15.96	(...)	(...)	17.51	(...)	9.01	8.97	(...)
33816	PGC033816	15.76	14.79	14.37	14.16	14.06	14.82	15.31	(...)	(...)	16.58	16.91	8.42	8.35	8.4×10^{-2}
33866	NGC3547	13.89	12.99	12.61	12.43	12.35	12.77	13.31	11.58	10.98	14.81	15.28	9.46	8.95	1.0×10^0
33905	PGC033905	16.23	15.38	15.04	14.82	14.97	15.75	16.56	(...)	(...)	16.76	16.93	8.89	8.40	4.5×10^{-2}
33981	PGC033981	15.81	15.01	14.76	14.61	14.53	15.56	15.97	(...)	(...)	16.31	16.59	8.23	8.48	9.3×10^{-2}
34015	PGC034015	15.36	14.30	13.75	13.47	13.30	13.79	14.41	13.27	(...)	16.48	16.97	9.48	8.56	3.0×10^{-1}

Table A.2 – continued

PGC (1)	Name (2)	u' (3)	g' (4)	r' (5)	i' (6)	z' (7)	W1 (8)	W2 (9)	W3 (10)	W4 (11)	FUV (12)	NUV (13)	M_\star (14)	M_{HI} (15)	SFR _{FUV} (16)
34107	IC0676	14.34	12.97	12.31	11.94	11.77	12.10	12.60	10.93	9.43	16.52	17.86	10.00	8.38	3.3×10^0
34124	UGC06248	16.82	15.57	15.13	14.89	14.79	16.28	17.17	(...)	(...)	17.56	17.96	8.89	8.32	4.0×10^{-2}
34135	PGC034135	15.71	14.76	14.36	14.15	14.06	14.75	15.23	(...)	(...)	16.88	17.39	8.66	8.26	1.0×10^{-1}
34151	PGC034151	15.36	14.44	14.12	13.97	13.89	14.58	15.10	(...)	(...)	15.82	16.05	9.37	9.38	6.3×10^{-1}
34257	NGC3593	12.78	11.22	10.43	10.03	9.81	9.93	10.43	(...)	8.31	15.33	16.69	9.82	8.34	1.2×10^0
34298	NGC3596	12.54	11.54	11.08	10.83	10.75	11.13	11.69	10.03	9.69	13.48	(...)	9.53	8.93	(...)
34438	PGC034438	(...)	15.44	14.91	14.73	14.69	15.64	16.26	(...)	(...)	18.24	19.16	8.00	7.24	2.9×10^{-2}
34478	NGC3611	13.58	12.40	11.86	11.57	11.46	11.75	12.23	10.35	9.68	15.13	15.98	10.10	9.45	3.3×10^0
34529	PGC034529	16.35	15.49	15.21	15.06	14.98	15.83	16.34	(...)	(...)	16.97	17.27	8.70	9.16	2.2×10^{-1}
34695	NGC3627	10.37	9.07	8.46	8.14	7.98	8.23	8.76	(...)	(...)	12.04	12.80	10.57	8.89	5.1×10^0
34719	NGC3629	13.67	12.78	12.48	12.29	12.26	12.89	13.47	12.25	(...)	14.31	15.21	9.90	9.67	1.2×10^1
34887	IC2763	15.84	14.77	14.38	14.16	14.08	14.70	15.39	(...)	(...)	16.91	17.53	8.74	8.42	1.7×10^{-1}
35044	UGC06421	16.06	15.16	14.89	14.70	14.71	15.56	16.14	(...)	(...)	16.75	17.02	8.70	9.20	1.2×10^{-1}
35151	PGC035151	15.00	14.11	13.70	13.52	13.46	14.14	14.61	13.72	(...)	16.04	16.52	9.07	8.64	2.7×10^{-1}
35225	IC2828	15.12	14.43	14.07	14.00	13.89	14.65	15.14	14.16	(...)	15.97	16.49	8.64	8.41	2.5×10^{-1}
35294	NGC3689	13.87	12.61	11.96	11.63	11.44	11.63	12.18	10.46	10.16	15.21	15.86	10.66	9.36	5.6×10^0
35405	NGC3701	14.34	13.23	12.81	12.62	12.43	13.02	13.57	11.91	(...)	15.05	15.34	9.93	9.90	1.6×10^0
35440	NGC3705	12.41	11.13	10.54	10.19	10.00	10.39	10.98	9.89	9.74	13.93	14.45	10.50	9.62	2.1×10^0
35739	PGC035739	15.78	14.99	14.75	14.64	14.60	15.51	16.08	(...)	(...)	16.29	16.65	8.55	8.77	1.8×10^{-1}
36043	NGC3773	14.03	13.26	12.81	12.61	12.51	13.14	13.69	12.26	(...)	14.69	14.93	9.19	8.33	3.7×10^{-1}
36174	IC0718	15.07	14.02	13.61	13.37	13.24	13.87	14.46	13.84	(...)	16.05	16.46	9.68	9.17	5.3×10^{-1}
36205	IC0719	14.62	13.28	12.58	12.19	11.94	12.19	12.79	11.97	(...)	16.26	16.91	10.18	8.95	7.7×10^{-1}
36243	NGC3810	11.88	10.87	10.38	10.13	9.98	10.27	10.75	(...)	8.34	12.98	13.58	10.15	9.49	4.5×10^0
36295	PGC036295	15.37	14.43	13.98	13.76	13.68	14.32	14.95	(...)	(...)	16.21	16.52	9.12	8.17	1.9×10^{-1}
36344	UGC06669	16.45	15.39	15.19	15.00	14.96	16.05	16.41	(...)	(...)	(...)	(...)	7.57	8.77	(...)

Table A.2 – continued

PGC (1)	Name (2)	u' (3)	g' (4)	r' (5)	i' (6)	z' (7)	W1 (8)	W2 (9)	W3 (10)	W4 (11)	FUV (12)	NUV (13)	M_* (14)	M_{HI} (15)	SFR _{FUV} (16)
36571	UGC06717	16.21	15.09	14.76	14.61	14.22	15.26	15.60	(...)	(...)	(...)	(...)	8.55	9.23	(...)
36644	NGC3876	14.29	13.39	13.07	12.86	12.76	13.35	13.87	12.42	(...)	(...)	(...)	9.85	9.29	(...)
36896	UGC06782	15.53	14.61	14.11	13.96	13.68	14.27	15.22	(...)	(...)	16.63	16.99	9.57	8.56	5.9×10^{-2}
36914	NGC3900	13.37	11.95	11.24	10.89	10.69	11.15	11.75	11.39	(...)	15.32	15.78	10.84	9.75	1.9×10^0
36976	PGC036976	15.49	14.84	14.74	14.81	14.65	15.44	15.90	(...)	11.82	(...)	(...)	7.39	7.60	(...)
36979	NGC3912	14.13	12.93	12.41	12.12	11.88	12.31	12.81	11.02	10.32	15.40	16.01	9.64	8.84	9.7×10^{-1}
37162	PGC037162	16.55	15.84	15.49	15.30	15.22	16.43	16.75	(...)	(...)	(...)	(...)	7.37	8.22	(...)
37301	PGC037301	16.88	16.07	15.84	15.74	15.64	16.32	17.04	(...)	(...)	17.20	17.26	8.80	8.31	1.2×10^{-1}
37483	NGC3976	13.25	12.02	11.43	11.06	10.77	11.15	11.78	10.45	10.21	14.61	14.99	10.85	10.18	2.9×10^0
37779	PGC037779	15.50	14.68	14.39	14.21	14.23	15.01	15.65	(...)	(...)	16.15	16.44	9.05	8.95	2.3×10^{-1}
37928	NGC4037	13.42	12.48	11.93	11.64	11.44	12.09	12.66	11.87	(...)	15.02	15.49	9.85	8.58	4.6×10^{-1}
37931	PGC037931	15.27	14.44	14.11	13.95	13.83	14.69	15.30	14.22	(...)	15.91	16.17	9.04	9.00	2.8×10^{-1}
37954	PGC037954	15.51	14.60	14.27	14.08	13.99	14.95	15.54	(...)	(...)	16.29	(...)	8.94	8.68	(...)
38113	PGC038113	15.03	14.05	13.55	13.31	13.18	13.63	14.17	12.46	(...)	16.05	16.64	9.06	8.15	2.6×10^{-1}
38168	NGC4067	14.27	13.06	12.46	12.14	11.96	12.40	13.02	11.96	(...)	15.53	15.94	10.53	9.36	2.0×10^0
38244	NGC4080	14.62	13.53	13.05	12.78	12.67	13.29	13.88	12.71	(...)	15.74	16.22	9.14	8.26	1.9×10^{-1}
38299	PGC038299	16.77	15.82	15.44	15.22	15.16	16.06	16.60	(...)	(...)	17.64	18.02	8.48	7.79	7.9×10^{-2}
38627	IC3017	16.62	15.47	14.97	14.73	14.55	14.93	15.49	13.96	(...)	17.57	18.20	9.06	8.75	2.1×10^{-1}
38637	UGC07138	15.41	14.45	14.06	13.87	13.68	14.70	15.33	(...)	(...)	16.18	16.40	9.41	9.17	3.5×10^{-1}
38667	UGC07143	15.01	14.20	13.86	13.72	13.62	14.15	14.55	13.16	(...)	15.71	16.08	9.38	9.66	1.0×10^0
38684	IC3021	16.53	15.19	14.70	14.45	14.39	15.15	15.77	(...)	(...)	17.69	18.01	9.12	8.45	1.2×10^{-1}
38692	IC3023	16.43	15.51	15.27	15.05	14.97	16.14	16.83	(...)	(...)	16.88	17.15	7.71	7.73	1.0×10^{-2}
38726	PGC038726	15.88	14.59	14.11	13.85	13.81	14.72	15.36	(...)	(...)	17.45	19.36	8.72	7.87	3.1×10^0
38728	PGC038728	17.24	16.08	15.64	15.38	15.25	16.09	16.83	(...)	(...)	18.24	18.87	8.80	8.22	1.1×10^{-1}
38747	PGC038747	16.17	15.30	14.85	14.57	14.53	15.24	15.84	(...)	(...)	17.41	17.88	8.58	8.47	5.2×10^{-2}

Table A.2 – continued

PGC (1)	Name (2)	u' (3)	g' (4)	r' (5)	i' (6)	z' (7)	W1 (8)	W2 (9)	W3 (10)	W4 (11)	FUV (12)	NUV (13)	M_{\star} (14)	M_{HI} (15)	SFR _{FUV} (16)
38749	NGC4152	13.24	12.27	11.90	11.70	11.60	11.98	12.46	10.38	9.57	14.03	15.14	10.09	9.88	3.0×10^1
38803	IC3033	15.81	14.81	14.45	14.27	14.22	15.01	15.62	(...)	(...)	16.62	17.03	8.46	8.39	8.3×10^{-2}
38835	PGC038835	17.18	16.08	15.64	15.40	15.27	16.31	16.91	(...)	(...)	18.47	19.13	8.82	8.56	1.6×10^{-1}
38851	NGC4162	13.45	12.42	11.90	11.62	11.42	11.75	12.30	10.73	10.43	14.55	15.02	10.61	9.79	5.5×10^0
38885	NGC4165	15.11	13.88	13.24	12.87	12.73	13.32	14.00	12.96	(...)	16.87	17.37	10.05	8.48	3.3×10^{-1}
38888	PGC038888	15.39	14.46	14.08	13.91	13.94	14.66	15.32	(...)	(...)	16.10	16.38	8.90	8.74	1.0×10^{-1}
38916	IC0769	14.21	12.97	12.51	12.24	12.12	12.71	13.27	12.24	(...)	15.17	15.69	10.01	9.61	2.1×10^0
38945	IC3044	14.89	13.88	13.51	13.32	13.09	14.16	14.91	(...)	(...)	15.85	16.30	8.96	8.79	2.4×10^{-1}
38964	NGC4180	14.20	12.83	12.12	11.71	11.45	11.58	12.07	10.63	10.12	16.13	17.08	10.20	8.87	2.3×10^0
39002	PGC039002	13.84	14.36	13.83	13.42	12.14	15.43	16.11	(...)	(...)	16.47	16.76	9.22	9.29	3.7×10^{-1}
39009	IC3049	17.93	16.41	15.57	15.15	14.89	15.04	15.62	(...)	(...)	19.27	19.81	8.55	8.17	1.1×10^{-2}
39018	PGC039018	15.55	14.75	14.44	14.24	14.22	15.12	15.52	(...)	(...)	16.39	(...)	8.04	8.55	(...)
39025	NGC4189	13.08	11.98	11.47	11.20	11.04	11.45	11.98	10.33	9.77	14.44	15.09	10.13	9.26	3.3×10^0
39034	NGC4191	14.76	13.11	12.38	12.01	11.77	12.29	12.92	13.51	(...)	17.18	17.90	9.86	8.80	1.3×10^{-1}
39040	NGC4193	13.98	12.69	12.04	11.67	11.49	11.83	12.44	11.39	10.95	15.44	16.06	10.53	9.46	2.8×10^0
39052	PGC039052	16.35	14.95	14.32	13.96	13.82	14.39	15.07	(...)	(...)	17.94	18.77	9.35	8.21	1.6×10^{-1}
39067	UGC07239	14.64	13.51	13.15	12.88	12.67	13.53	14.45	(...)	(...)	(...)	(...)	10.00	8.69	(...)
39142	IC3059	15.58	14.40	14.02	13.82	13.63	14.71	15.35	(...)	(...)	16.61	17.02	8.85	8.50	9.2×10^{-2}
39181	IC3066	16.59	15.27	14.77	14.51	14.35	15.20	15.85	(...)	(...)	17.78	18.34	8.66	8.04	4.6×10^{-2}
39206	NGC4207	14.37	13.03	12.30	11.95	11.72	11.81	12.30	10.71	10.46	16.45	17.20	9.58	8.65	3.0×10^{-1}
39224	NGC4212	12.60	11.39	10.82	10.51	10.32	10.68	11.20	(...)	9.11	13.99	14.64	10.08	8.95	2.1×10^0
39230	PGC039230	16.41	15.62	15.39	15.25	15.05	16.23	16.77	(...)	(...)	17.08	17.33	8.30	8.52	7.9×10^{-2}
39256	IC3077	15.36	14.08	13.52	13.18	13.08	13.82	14.73	(...)	(...)	17.76	19.60	8.68	7.01	3.9×10^{-1}
39265	PGC039265	15.69	14.67	14.34	14.19	14.13	15.04	15.51	(...)	(...)	16.36	16.75	8.83	8.77	2.2×10^{-1}
39288	PGC039288	16.69	15.44	14.88	14.61	14.46	15.41	16.19	(...)	(...)	18.35	19.29	8.93	7.63	1.5×10^{-1}

Table A.2 – continued

PGC (1)	Name (2)	u' (3)	g' (4)	r' (5)	i' (6)	z' (7)	W1 (8)	W2 (9)	W3 (10)	W4 (11)	FUV (12)	NUV (13)	M_{\star} (14)	M_{HI} (15)	SFR _{FUV} (16)
39328	NGC4224	13.82	12.19	11.39	10.96	10.68	11.10	11.76	11.95	(...)	17.09	18.36	11.22	9.30	5.9×10^0
39358	IC3096	16.03	14.74	14.17	13.89	13.68	14.50	15.18	(...)	(...)	17.70	(...)	8.86	7.63	(...)
39362	PGC039362	15.27	14.12	13.57	13.30	13.08	13.67	14.21	12.67	(...)	16.46	16.94	9.08	7.90	1.3×10^{-1}
39392	PGC039392	17.16	16.01	15.73	15.53	15.27	16.10	16.77	(...)	(...)	18.19	18.58	8.50	7.62	4.1×10^{-2}
39393	NGC4237	13.30	11.98	11.33	10.97	10.78	11.10	11.67	10.39	10.05	(...)	(...)	10.24	8.52	(...)
39412	IC3102	13.96	12.42	11.69	11.28	11.05	11.53	12.20	12.53	(...)	17.12	18.27	10.69	8.53	1.9×10^0
39431	IC3105	15.02	14.41	14.22	14.19	14.11	15.44	16.34	(...)	(...)	15.45	15.68	9.13	8.73	1.9×10^{-1}
39483	NGC4241	14.26	13.30	12.91	12.68	12.47	13.39	14.02	(...)	(...)	15.27	15.61	9.07	8.73	2.4×10^{-1}
39513	PGC039513	16.65	15.43	14.89	14.65	14.52	15.47	16.13	(...)	(...)	18.08	18.89	8.44	7.56	6.6×10^{-2}
39537	NGC4252	15.18	14.28	13.90	13.69	13.65	14.37	14.82	(...)	(...)	16.13	16.48	8.81	8.54	1.2×10^{-1}
39578	NGC4254	10.92	9.95	9.46	9.19	9.06	9.33	9.79	(...)	(...)	12.03	12.60	10.30	9.54	7.2×10^0
39613	IC0776	14.88	14.04	13.74	13.57	13.43	14.27	14.75	(...)	(...)	15.40	15.63	9.10	9.45	7.6×10^{-1}
39619	PGC039619	16.30	15.02	14.63	14.40	14.27	15.84	16.22	(...)	(...)	17.47	18.35	7.72	8.32	1.4×10^{-1}
39641	PGC039641	16.28	15.43	15.07	14.88	14.79	15.63	16.38	(...)	(...)	17.20	17.48	8.48	7.93	4.5×10^{-2}
39646	PGC039646	(...)	(...)	(...)	(...)	(...)	15.45	16.18	(...)	(...)	17.61	18.17	8.43	7.64	5.2×10^{-2}
39655	PGC039655	15.61	14.57	14.17	13.96	13.88	14.59	15.14	(...)	(...)	16.50	16.88	8.93	8.66	1.7×10^{-1}
39658	IC3148	16.17	15.17	14.75	14.48	14.42	15.25	15.96	(...)	(...)	17.35	17.75	9.13	8.32	9.2×10^{-2}
39718	NGC4270	14.12	12.48	11.78	11.38	11.19	11.60	12.30	13.66	(...)	17.40	19.34	10.47	8.44	5.4×10^0
39728	PGC039728	14.18	13.13	12.63	12.36	12.23	12.61	13.16	11.32	10.98	15.19	15.69	10.12	8.97	2.0×10^0
39738	NGC4273	12.95	11.96	11.52	11.29	11.16	11.34	11.76	9.49	8.79	14.01	14.52	10.11	9.60	5.1×10^0
39765	NGC4276	14.30	13.18	12.70	12.46	12.36	13.01	13.57	12.27	(...)	15.42	15.90	9.88	9.07	1.3×10^0
39813	PGC039813	16.07	15.03	14.57	14.31	14.12	14.98	15.64	(...)	(...)	17.13	17.49	8.82	8.43	1.0×10^{-1}
39860	NGC4287	15.94	14.61	14.00	13.62	13.39	13.82	14.44	13.18	(...)	17.76	18.43	9.03	7.96	6.6×10^{-2}
39878	PGC039878	16.50	15.63	15.17	14.93	14.75	15.92	16.58	(...)	(...)	18.01	18.59	8.38	7.56	3.8×10^{-2}
39925	NGC4294	13.01	12.18	11.81	11.62	11.60	12.14	12.70	11.29	10.45	13.83	14.23	9.57	9.28	1.3×10^0

Table A.2 – continued

PGC (1)	Name (2)	u' (3)	g' (4)	r' (5)	i' (6)	z' (7)	W1 (8)	W2 (9)	W3 (10)	W4 (11)	FUV (12)	NUV (13)	M_* (14)	M_{HI} (15)	SFR _{FUV} (16)
39968	NGC4299	13.19	12.47	12.18	12.08	12.06	12.68	13.24	11.68	10.48	13.82	14.06	9.32	9.10	8.7×10^{-1}
40001	NGC4303	10.80	9.80	9.31	9.03	8.84	9.20	9.62	(...)	7.32	11.83	12.19	10.56	9.79	8.1×10^0
40004	PGC040004	15.83	(...)	14.77	14.60	14.42	15.49	16.01	(...)	(...)	16.94	17.17	8.44	8.71	9.4×10^{-2}
40014	UGC07424	15.78	14.72	14.22	13.94	13.81	14.81	15.63	(...)	(...)	17.25	17.73	9.22	7.83	5.9×10^{-2}
40021	UGC07422	15.81	14.29	13.53	13.13	12.90	13.35	13.97	13.01	(...)	18.14	19.03	9.36	7.83	8.7×10^{-2}
40087	NGC4301	13.90	13.23	12.97	12.84	12.78	13.66	14.24	13.74	(...)	14.54	14.68	9.08	9.20	3.0×10^{-1}
40100	PGC040100	16.61	15.85	15.57	15.50	15.31	16.39	17.02	(...)	(...)	16.89	17.15	8.07	7.74	5.4×10^{-2}
40105	NGC4313	13.55	11.96	11.25	10.85	10.62	10.94	11.55	11.09	(...)	16.16	17.78	10.01	7.85	2.3×10^0
40147	IC3229	15.96	14.87	14.40	14.16	14.05	14.87	15.44	(...)	(...)	16.95	17.35	8.92	8.54	1.2×10^{-1}
40153	NGC4321	10.48	9.65	9.16	8.65	8.71	8.89	9.40	(...)	(...)	12.04	12.61	10.63	9.35	7.5×10^0
40179	NGC4324	13.52	11.98	11.29	10.85	10.64	11.07	11.76	11.96	(...)	15.56	16.44	10.67	9.17	2.2×10^0
40187	IC3239	16.68	15.76	15.37	15.19	14.96	15.90	16.77	(...)	(...)	17.59	18.01	8.93	8.11	3.7×10^{-2}
40201	NGC4330	13.84	12.71	12.11	11.84	11.64	11.99	12.51	11.48	(...)	15.28	15.72	9.69	8.77	5.0×10^{-1}
40229	PGC040229	16.96	15.99	15.57	15.38	15.37	16.22	16.83	(...)	(...)	17.88	18.28	8.15	7.63	2.7×10^{-2}
40251	NGC4343	14.10	12.66	11.90	11.47	11.21	11.42	12.00	11.20	11.04	16.40	17.23	10.25	8.85	7.3×10^{-1}
40264	IC3258	14.21	13.39	13.11	13.02	12.83	13.86	14.14	13.08	(...)	14.80	15.01	8.56	8.49	3.3×10^{-1}
40273	IC3259	14.96	13.76	13.18	12.87	12.66	13.29	13.90	13.08	(...)	16.46	16.91	9.47	8.24	1.6×10^{-1}
40303	NGC4353	14.92	13.71	13.15	12.83	12.66	13.32	13.98	13.11	(...)	16.42	16.93	9.58	8.27	3.2×10^{-1}
40306	NGC4351	13.73	12.67	12.23	12.00	11.95	12.53	13.05	12.04	(...)	14.94	15.53	9.39	8.57	7.7×10^{-1}
40310	PGC040310	15.83	14.78	14.43	14.23	14.34	15.11	15.93	(...)	(...)	16.58	16.95	9.46	8.64	1.8×10^{-1}
40317	IC3267	14.61	13.59	13.06	12.73	12.62	13.35	13.98	12.75	(...)	16.23	16.76	9.39	8.13	1.8×10^{-1}
40321	IC3268	14.19	13.32	12.95	12.74	12.73	13.42	14.01	12.96	(...)	14.98	15.33	9.43	9.08	1.0×10^0
40342	NGC4356	14.28	12.91	12.23	11.82	11.67	12.01	12.69	12.30	(...)	17.03	18.82	9.94	7.78	2.6×10^0
40408	PGC040408	15.85	14.82	14.42	14.23	14.18	14.92	15.45	(...)	(...)	16.62	16.95	8.90	9.03	1.5×10^{-1}
40461	PGC040461	16.63	15.18	14.52	14.15	13.97	14.70	15.30	(...)	(...)	18.55	19.05	9.24	8.20	4.0×10^{-2}

Table A.2 – continued

PGC (1)	Name (2)	u' (3)	g' (4)	r' (5)	i' (6)	z' (7)	W1 (8)	W2 (9)	W3 (10)	W4 (11)	FUV (12)	NUV (13)	M_{\star} (14)	M_{HI} (15)	SFR _{FUV} (16)
40490	NGC4378	13.40	11.78	11.03	10.62	10.55	10.82	11.47	10.71	(...)	15.32	15.76	10.89	9.44	1.3×10^0
40494	NGC4376	14.31	13.44	13.05	12.86	12.82	13.47	14.00	12.92	(...)	15.14	15.41	8.92	8.61	2.8×10^{-1}
40495	PGC040495	15.67	14.91	14.69	14.60	14.49	15.64	16.28	(...)	(...)	(...)	(...)	7.37	7.88	(...)
40507	NGC4380	13.19	11.88	11.18	10.80	10.54	11.00	11.64	11.07	(...)	15.05	15.66	10.17	8.15	6.1×10^{-1}
40588	PGC040588	16.32	15.18	14.65	14.39	14.17	15.14	15.71	(...)	(...)	17.91	18.55	7.86	7.07	1.1×10^{-2}
40597	NGC4390	13.95	12.95	12.56	12.34	12.29	12.90	13.45	12.17	(...)	14.90	15.26	9.33	8.68	4.5×10^{-1}
40600	NGC4393	13.52	12.60	12.26	12.14	12.16	12.87	13.55	(...)	(...)	14.02	(...)	9.67	9.35	(...)
40643	NGC4405	13.87	12.55	11.93	11.59	11.44	11.87	12.46	11.36	11.13	15.75	16.81	9.78	7.71	1.3×10^0
40670	PGC040670	16.10	15.34	14.92	14.70	14.58	15.68	16.37	(...)	(...)	17.37	17.71	8.52	8.14	4.4×10^{-2}
40695	NGC4411A	14.16	13.14	12.69	12.43	12.26	13.10	13.45	12.96	(...)	15.10	15.43	8.67	9.03	3.5×10^{-1}
40705	NGC4413	13.69	12.44	11.87	11.54	11.40	11.99	12.64	11.45	10.98	15.16	15.70	9.76	8.23	4.5×10^{-1}
40715	NGC4412	13.80	12.63	12.14	11.89	11.80	12.13	12.75	10.90	9.86	14.76	15.20	10.17	8.91	2.0×10^0
40743	NGC4416	12.92	12.66	12.09	11.74	11.56	12.40	13.02	11.37	(...)	14.95	15.40	9.62	8.51	4.8×10^{-1}
40745	NGC4411B	13.90	12.55	12.15	11.90	11.77	12.55	13.05	12.07	(...)	14.44	14.75	9.41	9.15	5.9×10^{-1}
40761	IC3356	15.76	14.98	14.72	14.62	14.59	16.33	17.23	(...)	(...)	16.59	16.71	8.59	8.93	3.3×10^{-2}
40807	UGC07557	12.76	12.74	12.18	12.09	11.73	12.71	13.76	11.81	(...)	14.65	14.85	10.62	9.24	3.7×10^{-1}
40809	NGC4424	13.13	11.83	11.27	10.94	10.89	11.36	11.88	10.96	10.08	15.19	16.21	9.94	8.43	1.6×10^0
40811	IC3365	14.87	14.03	13.78	13.61	13.51	14.50	15.30	(...)	(...)	15.36	15.60	9.37	8.72	2.7×10^{-1}
40825	PGC040825	16.93	15.85	15.44	15.16	15.11	15.97	16.55	(...)	(...)	17.98	18.49	8.51	7.83	6.9×10^{-2}
40851	NGC4430	13.61	12.28	11.75	11.46	11.36	11.82	12.32	11.01	(...)	14.71	15.16	9.56	8.60	6.2×10^{-1}
40861	UGC07567	16.03	14.83	14.33	14.08	13.90	14.86	15.51	(...)	(...)	17.06	17.45	9.01	8.63	1.3×10^{-1}
40876	PGC040876	16.23	15.23	14.72	14.44	14.30	15.44	16.13	(...)	(...)	18.37	19.27	8.64	7.54	6.2×10^{-2}
40914	NGC4438	12.06	10.45	9.73	9.31	9.08	9.44	10.05	(...)	(...)	13.97	14.75	10.90	8.73	3.1×10^0
40933	UGC07579	15.60	14.48	13.96	13.67	13.53	14.02	14.57	13.06	(...)	16.88	17.50	9.26	8.66	4.7×10^{-1}
40993	UGC07590	14.67	13.94	13.67	13.49	13.51	14.06	14.67	(...)	(...)	15.24	15.52	9.40	9.50	7.9×10^{-1}

Table A.2 – continued

PGC (1)	Name (2)	u' (3)	g' (4)	r' (5)	i' (6)	z' (7)	W1 (8)	W2 (9)	W3 (10)	W4 (11)	FUV (12)	NUV (13)	M_* (14)	M_{HI} (15)	SFR _{FUV} (16)
41036	UGC07596	16.04	14.52	14.06	13.82	13.75	14.69	15.32	(...)	(...)	17.27	18.19	7.71	6.47	1.4×10^{-2}
41050	NGC4451	14.14	12.90	12.33	12.00	11.89	12.35	12.90	11.34	11.01	15.54	16.27	9.91	8.65	1.5×10^0
41061	IC3392	13.97	12.51	11.87	11.50	11.30	11.75	12.33	11.44	11.23	16.26	17.78	9.56	7.60	1.3×10^0
41152	IC3412	16.09	15.22	14.80	14.62	14.51	15.32	15.91	(...)	(...)	16.90	17.23	8.42	7.47	5.3×10^{-2}
41166	IC3414	14.57	13.62	13.23	13.00	12.95	13.71	14.30	13.05	(...)	15.45	15.77	8.74	8.20	1.2×10^{-1}
41170	PGC041170	15.01	13.96	13.47	13.20	13.09	13.74	14.21	12.60	(...)	16.20	16.57	9.44	8.72	4.5×10^{-1}
41178	PGC041178	15.85	15.04	14.77	14.61	14.65	15.44	16.04	(...)	(...)	16.64	16.93	8.42	8.26	6.4×10^{-2}
41189	NGC4470	13.63	12.70	12.28	12.05	11.94	12.46	12.99	11.37	11.05	14.55	14.95	9.23	8.52	4.5×10^{-1}
41317	NGC4480	13.84	12.75	12.26	11.97	11.85	12.26	12.87	11.41	10.96	14.82	15.25	10.45	9.70	3.8×10^0
41383	NGC4492	13.53	11.98	11.27	10.85	10.68	11.14	11.76	11.88	(...)	15.90	16.70	10.23	7.61	5.5×10^{-1}
41440	IC3446	15.75	15.08	14.75	14.60	14.60	15.31	16.07	12.82	(...)	16.56	16.80	8.98	8.36	7.1×10^{-2}
41466	IC3453	15.19	14.36	14.07	13.94	13.92	14.72	15.27	(...)	(...)	15.77	16.09	8.51	8.24	1.8×10^{-1}
41471	NGC4496A	12.37	11.75	11.41	11.18	11.19	11.71	12.20	10.65	(...)	13.38	13.66	9.58	9.35	1.1×10^0
41504	IC0797	14.21	13.15	12.71	12.48	12.38	12.91	13.58	12.05	(...)	15.24	15.80	9.38	8.25	4.1×10^{-1}
41517	NGC4501	11.26	9.87	9.15	8.73	8.50	8.76	9.34	(...)	7.97	12.89	13.71	11.14	9.42	1.3×10^1
41536	IC3466	16.46	15.29	14.93	14.70	14.57	15.35	16.45	(...)	(...)	17.73	18.31	9.74	8.05	4.9×10^{-2}
41567	IC3471	16.14	15.07	14.65	14.36	14.31	15.09	15.68	(...)	(...)	17.30	17.84	8.56	7.99	6.6×10^{-2}
41608	IC3476	13.70	12.85	12.46	12.29	12.20	12.77	13.22	11.57	10.66	14.53	14.86	8.91	8.22	3.7×10^{-1}
41619	PGC041619	17.33	16.35	15.86	15.60	15.47	16.47	16.69	(...)	(...)	18.64	19.05	7.04	7.24	1.4×10^{-2}
41670	IC3483	15.48	14.42	13.82	13.47	13.32	14.10	15.10	(...)	(...)	17.27	18.01	9.03	7.53	1.4×10^{-1}
41716	PGC041716	16.41	15.34	14.82	14.56	14.33	15.08	15.66	(...)	(...)	17.68	17.89	8.51	7.94	1.9×10^{-2}
41719	NGC4519	13.00	12.05	11.72	11.55	11.37	12.06	12.54	10.45	9.56	13.70	13.98	9.96	10.04	3.8×10^0
41729	NGC4522	13.41	12.54	12.09	11.80	11.57	12.03	12.57	11.38	11.11	14.82	15.27	9.52	8.55	4.4×10^{-1}
41746	NGC4523	13.13	12.89	12.47	12.30	12.00	12.84	13.54	(...)	(...)	14.34	14.61	9.66	9.21	5.9×10^{-1}
41763	IC0800	14.20	13.30	12.81	12.54	12.44	13.08	13.46	12.53	(...)	15.62	16.01	8.91	7.74	1.7×10^{-1}

Table A.2 – continued

PGC (1)	Name (2)	u' (3)	g' (4)	r' (5)	i' (6)	z' (7)	W1 (8)	W2 (9)	W3 (10)	W4 (11)	FUV (12)	NUV (13)	M_{\star} (14)	M_{HI} (15)	SFR _{FUV} (16)
41811	NGC4532	12.59	11.84	11.52	11.38	11.34	11.74	12.23	10.41	9.10	13.29	13.71	9.40	9.27	1.5×10^0
41812	NGC4535	11.49	10.20	9.69	9.35	9.27	9.72	10.19	8.57	7.89	12.43	12.89	10.44	9.64	5.1×10^0
41829	IC3517	15.76	14.96	14.52	14.31	14.00	14.98	15.61	(...)	(...)	17.01	17.34	8.47	7.68	4.1×10^{-2}
41830	IC3520	16.54	15.37	14.93	14.70	14.68	15.48	15.97	(...)	(...)	17.30	17.78	8.14	7.57	5.8×10^{-2}
41847	IC3521	14.60	13.37	12.76	12.46	12.28	12.80	13.48	11.94	(...)	15.94	16.55	9.56	7.97	3.2×10^{-1}
41861	UGC07739	15.55	14.50	14.07	13.82	13.71	14.71	15.33	(...)	(...)	16.73	17.18	8.56	8.73	6.9×10^{-2}
41865	IC3522	15.73	14.99	14.70	14.55	14.41	15.69	16.43	(...)	(...)	16.43	16.62	8.63	8.90	6.9×10^{-2}
41876	NGC4540	13.27	12.00	11.52	11.14	10.89	11.65	12.26	11.02	10.77	14.94	15.71	9.94	8.49	1.2×10^0
41934	NGC4548	11.88	10.43	9.72	9.33	9.17	9.60	10.16	9.75	(...)	13.89	14.56	10.65	8.85	2.6×10^0
41942	PGC041942	16.31	15.19	14.69	14.41	14.37	15.19	15.87	(...)	(...)	17.75	18.31	8.54	7.62	4.5×10^{-2}
42002	NGC4559	11.12	10.12	9.77	9.48	9.41	9.99	10.43	9.18	8.71	11.84	12.17	9.54	9.54	1.3×10^0
42021	IC3562	16.81	15.81	15.49	15.35	15.18	16.29	16.81	(...)	(...)	17.67	18.31	7.95	8.31	9.0×10^{-2}
42064	NGC4567	12.42	11.33	10.77	10.46	10.29	10.75	11.44	9.90	9.67	14.19	14.94	10.24	9.20	2.4×10^0
42068	PGC042068	15.44	14.23	13.69	13.41	13.24	13.93	14.64	(...)	(...)	16.86	17.59	8.51	6.79	3.3×10^{-2}
42074	IC3576	14.65	13.81	13.52	13.38	13.44	14.40	15.08	(...)	(...)	15.21	15.45	8.97	9.03	2.4×10^{-1}
42081	IC3583	13.71	12.88	12.57	12.38	12.35	13.19	13.62	13.05	(...)	14.79	15.14	8.55	8.07	1.2×10^{-1}
42089	NGC4569	11.19	9.82	9.27	8.90	8.73	9.16	9.56	7.56	8.02	13.30	14.60	10.73	8.87	2.3×10^1
42100	NGC4571	12.72	11.41	10.84	10.47	10.34	10.84	11.42	10.54	10.51	14.28	14.82	10.05	8.73	9.8×10^{-1}
42108	IC3591	15.27	14.23	13.86	13.64	13.64	14.27	14.95	13.40	(...)	16.02	16.42	9.05	8.77	1.8×10^{-1}
42143	PGC042143	16.56	15.74	15.43	15.19	15.12	16.30	16.75	(...)	(...)	17.43	17.73	6.97	7.29	5.9×10^{-3}
42160	PGC042160	15.10	14.29	13.93	13.79	13.68	14.59	15.13	(...)	(...)	15.64	15.84	8.43	8.06	1.1×10^{-1}
42169	UGC07795	15.56	14.81	14.59	14.52	14.28	15.45	15.97	(...)	(...)	15.79	15.91	8.22	8.61	8.6×10^{-2}
42174	NGC4580	13.65	12.19	11.49	11.11	10.92	11.33	11.90	11.17	10.97	15.54	16.65	10.04	7.60	1.8×10^0
42223	NGC4584	14.77	13.31	12.75	12.43	12.32	12.85	13.55	11.38	(...)	16.74	18.00	9.51	7.49	7.4×10^{-1}
42307	IC3611	15.10	13.84	13.42	13.17	13.12	13.86	14.35	(...)	(...)	16.44	17.45	8.91	7.88	5.0×10^{-1}

Table A.2 – continued

PGC (1)	Name (2)	u' (3)	g' (4)	r' (5)	i' (6)	z' (7)	W1 (8)	W2 (9)	W3 (10)	W4 (11)	FUV (12)	NUV (13)	M_* (14)	M_{HI} (15)	SFR _{FUV} (16)
42319	NGC4591	14.55	13.42	12.81	12.47	12.30	12.72	13.37	12.26	(...)	15.90	16.34	10.10	8.92	7.6×10^{-1}
42340	PGC042340	16.14	15.00	14.49	14.24	14.11	15.00	15.47	(...)	(...)	17.18	17.61	8.28	8.08	5.6×10^{-2}
42348	IC3617	14.93	14.14	13.92	13.78	13.76	14.68	15.27	(...)	(...)	15.27	15.51	8.56	8.61	1.9×10^{-1}
42396	NGC4595	13.56	12.54	12.14	11.95	11.84	12.42	12.94	11.52	11.14	14.67	15.13	9.16	8.44	4.1×10^{-1}
42516	NGC4606	13.73	12.24	11.66	11.30	11.14	11.69	12.27	11.71	(...)	16.07	17.91	9.86	7.78	6.2×10^0
42544	NGC4607	14.65	13.23	12.54	12.10	11.92	11.86	12.22	10.62	10.25	16.85	17.80	9.18	8.08	1.9×10^{-1}
42688	NGC4630	13.69	12.61	12.06	11.78	11.65	12.12	12.66	10.96	10.15	14.86	15.32	9.51	8.63	5.2×10^{-1}
42699	NGC4633	14.32	13.37	12.90	12.65	12.50	13.30	13.85	12.62	(...)	15.38	15.82	9.29	8.84	3.6×10^{-1}
42707	NGC4634	13.81	12.64	12.11	11.76	11.59	11.56	12.08	10.38	10.07	15.53	16.24	9.70	8.70	6.3×10^{-1}
42710	PGC042710	16.18	15.37	15.05	14.79	14.79	15.68	16.02	(...)	(...)	16.67	17.04	7.70	8.00	7.6×10^{-2}
42741	NGC4639	13.20	11.84	11.26	10.93	10.77	11.22	11.80	11.06	(...)	14.14	14.55	10.29	9.34	1.7×10^0
42762	PGC042762	16.03	15.16	14.83	14.64	14.48	15.60	16.14	(...)	(...)	16.59	16.83	8.98	9.12	1.9×10^{-1}
42769	NGC4641	14.77	13.44	12.88	12.59	12.50	13.13	13.76	13.22	(...)	16.49	17.51	9.33	7.76	5.0×10^{-1}
42816	NGC4647	12.43	11.12	10.49	10.15	10.01	10.40	11.07	(...)	9.23	13.93	14.81	10.98	8.69	4.0×10^0
42947	PGC042947	16.86	15.64	15.21	14.95	14.92	15.76	16.40	(...)	(...)	18.20	18.86	8.39	7.54	4.0×10^{-2}
42987	PGC042987	13.26	12.71	12.37	12.22	12.07	12.82	13.31	11.85	10.40	13.95	14.15	9.00	8.67	5.1×10^{-1}
43001	IC3742	14.79	13.74	13.37	13.18	13.05	13.76	14.37	(...)	(...)	15.53	(...)	9.28	9.06	(...)
43051	PGC043051	15.92	14.93	14.53	14.28	14.22	15.00	15.57	(...)	(...)	16.76	17.12	8.22	7.07	2.4×10^{-2}
43056	PGC043056	15.64	14.44	14.01	14.05	13.79	15.80	16.66	(...)	(...)	17.50	17.95	8.94	7.93	4.4×10^{-2}
43072	PGC043072	16.33	15.46	15.05	14.79	14.87	15.85	16.38	(...)	(...)	17.33	17.75	7.39	7.01	9.4×10^{-3}
43106	UGC07943	13.93	13.34	13.01	12.78	12.73	13.50	14.09	(...)	(...)	(...)	(...)	9.15	8.81	(...)
43186	NGC4689	12.56	11.17	10.58	10.27	10.02	10.51	11.17	9.78	9.68	(...)	(...)	10.44	8.70	(...)
43189	NGC4688	13.27	12.47	12.20	12.12	12.02	12.66	13.36	12.10	(...)	13.94	14.19	9.60	9.26	7.0×10^{-1}
43205	PGC043205	15.86	14.95	14.60	14.41	14.34	15.25	16.04	(...)	(...)	16.70	17.07	8.98	7.78	7.4×10^{-2}
43241	NGC4694	13.13	11.69	11.15	10.84	10.73	11.36	11.94	11.53	11.23	15.07	16.54	9.98	8.58	6.9×10^0

Table A.2 – continued

PGC (1)	Name (2)	u' (3)	g' (4)	r' (5)	i' (6)	z' (7)	W1 (8)	W2 (9)	W3 (10)	W4 (11)	FUV (12)	NUV (13)	M_{\star} (14)	M_{HI} (15)	SFR _{FUV} (16)
43254	NGC4698	11.98	10.85	10.13	9.73	9.50	9.99	10.61	10.77	(...)	14.86	15.75	11.08	9.72	4.7×10^0
43338	UGC07976	15.63	14.89	14.63	14.51	14.51	15.23	15.44	(...)	(...)	16.02	16.23	7.74	8.97	2.0×10^{-1}
43390	PGC043390	16.57	15.67	15.44	15.33	15.41	16.21	16.72	(...)	(...)	17.11	17.45	7.39	8.21	1.5×10^{-2}
43413	NGC4713	12.58	11.82	11.52	11.38	11.30	11.88	12.41	10.47	9.90	13.23	13.57	9.51	9.44	1.7×10^0
43451	NGC4725	10.67	9.60	8.93	8.52	8.27	8.76	9.42	9.16	(...)	12.80	13.09	10.96	9.64	1.4×10^0
43586	NGC4747	13.81	12.49	11.98	11.73	11.60	12.06	12.67	11.59	11.24	15.14	15.55	9.65	9.14	2.9×10^{-1}
43595	PGC043595	16.57	15.75	15.46	15.31	15.48	16.38	16.91	(...)	(...)	17.22	17.40	7.38	7.74	8.5×10^{-3}
43775	NGC4765	13.74	12.92	12.61	12.47	12.38	13.05	13.58	11.89	10.81	14.35	14.70	9.04	9.05	6.2×10^{-1}
43837	NGC4779	13.77	12.68	12.18	11.91	11.75	12.21	12.69	11.17	10.39	14.71	15.19	10.11	9.41	3.2×10^0
43869	NGC4789A	14.70	13.95	13.70	13.65	13.45	14.81	15.28	(...)	(...)	14.91	14.97	7.04	8.42	1.2×10^{-2}
43907	PGC043907	16.70	15.71	15.33	15.07	14.97	16.04	16.43	(...)	(...)	17.95	18.25	7.58	8.03	1.6×10^{-2}
43950	NGC4791	15.98	14.52	13.89	13.55	13.39	13.93	14.61	13.97	(...)	17.45	17.94	9.88	8.55	2.8×10^{-1}
44008	UGC08042	15.62	14.82	14.40	14.09	14.10	14.62	15.48	(...)	(...)	16.87	17.25	9.58	8.72	3.9×10^{-1}
44033	UGC08045	15.50	14.18	13.72	13.44	13.42	13.93	14.37	(...)	(...)	16.64	17.09	9.56	8.86	6.3×10^{-1}
44086	NGC4808	12.96	12.01	11.57	11.33	11.15	11.39	11.85	9.86	9.39	13.99	14.50	9.71	9.75	1.8×10^0
44089	UGC08053	15.07	14.22	13.99	13.90	13.73	14.80	15.27	(...)	(...)	15.45	15.72	8.25	8.94	1.9×10^{-1}
44125	UGC08056	15.50	14.59	14.30	14.16	14.02	14.88	15.37	(...)	(...)	16.00	16.27	9.05	9.54	6.6×10^{-1}
44215	PGC044215	15.63	14.79	14.48	14.33	14.22	15.20	15.79	(...)	(...)	16.28	16.54	8.47	8.41	8.1×10^{-2}
44491	UGC08091	15.02	14.42	14.12	14.04	13.91	15.58	16.18	(...)	(...)	15.25	15.27	6.56	7.07	2.2×10^{-3}
44517	PGC044517	14.30	14.55	12.31	13.95	13.10	15.40	15.77	(...)	(...)	16.45	16.66	8.40	9.17	2.1×10^{-1}
44753	UGC08114	15.93	15.15	14.85	14.80	15.07	15.79	16.01	(...)	(...)	16.61	17.02	7.88	9.32	3.2×10^{-1}
45071	UGC08153	15.09	14.16	13.85	13.72	13.68	14.15	14.77	(...)	(...)	15.59	15.85	9.20	9.08	3.5×10^{-1}
45079	UGC08155	14.40	13.42	12.91	12.59	12.38	12.93	13.76	(...)	(...)	15.49	15.91	10.49	9.83	1.9×10^0
45311	NGC4961	14.24	13.37	12.98	12.78	12.74	13.16	13.64	11.82	(...)	15.02	15.35	9.81	9.75	2.1×10^0
45370	PGC045370	16.06	15.29	15.04	14.86	14.79	15.61	16.08	(...)	(...)	16.55	16.77	8.04	8.70	5.7×10^{-2}

Table A.2 – continued

PGC (1)	Name (2)	u' (3)	g' (4)	r' (5)	i' (6)	z' (7)	W1 (8)	W2 (9)	W3 (10)	W4 (11)	FUV (12)	NUV (13)	M_{\star} (14)	M_{HI} (15)	SFR _{FUV} (16)
45836	NGC5016	13.82	12.73	12.21	11.95	11.81	12.20	12.80	11.29	11.03	14.75	15.12	10.43	9.53	3.0×10^0
45858	PGC045858	15.00	13.88	13.38	13.09	13.02	13.61	14.15	12.97	(...)	16.06	16.43	8.61	7.98	4.8×10^{-2}
45875	PGC045875	15.44	14.44	14.02	13.80	13.77	14.68	15.26	(...)	(...)	16.73	17.30	8.89	8.78	1.2×10^{-1}
45931	UGC08298	15.66	14.66	14.35	14.17	14.12	15.13	15.61	(...)	(...)	16.14	16.41	7.88	8.70	5.4×10^{-2}
46159	UGC08333	16.16	15.23	14.89	14.73	14.80	15.61	16.25	(...)	(...)	16.96	17.25	8.64	9.10	9.2×10^{-2}
46241	PGC046241	14.61	13.84	13.53	13.38	13.29	14.06	14.64	(...)	(...)	15.18	15.48	8.89	9.04	2.5×10^{-1}
46387	PGC046387	15.90	14.99	14.72	14.58	14.66	15.48	16.03	(...)	(...)	16.42	16.59	9.00	9.53	3.0×10^{-1}
46556	PGC046556	15.67	14.71	14.38	14.22	14.08	15.10	15.64	(...)	(...)	16.33	(...)	8.41	8.58	(...)
46563	UGC08385	14.80	13.84	13.49	13.29	13.22	14.07	14.60	(...)	(...)	15.42	15.66	8.77	9.06	1.6×10^{-1}
47101	PGC047101	16.04	15.05	14.75	14.52	14.45	15.49	16.22	(...)	(...)	16.85	17.13	8.71	8.37	4.8×10^{-2}
47826	PGC047826	15.73	14.74	14.43	14.29	14.25	15.24	16.04	(...)	(...)	16.65	17.03	8.79	8.41	6.4×10^{-2}
48046	PGC048046	16.65	15.53	15.10	14.93	14.83	15.88	16.58	(...)	(...)	17.73	17.95	8.43	8.01	1.6×10^{-2}
48122	UGC08614	14.25	13.30	12.93	12.66	12.59	13.62	14.08	(...)	(...)	15.06	15.45	8.50	8.98	2.4×10^{-1}
48130	NGC5248	11.37	10.45	9.83	9.38	9.32	9.65	10.16	(...)	7.79	12.99	13.41	10.27	9.47	1.8×10^0
48212	UGC08629	16.37	15.56	15.24	15.10	14.98	16.12	16.73	(...)	(...)	17.13	17.43	8.19	8.60	4.0×10^{-2}
48280	PGC048280	15.01	14.18	13.83	13.69	13.59	14.72	15.21	(...)	(...)	15.66	15.88	7.22	7.27	9.8×10^{-3}
48959	NGC5300	13.12	11.99	11.53	11.22	11.15	11.63	12.28	11.07	10.88	14.29	14.46	10.05	9.13	5.6×10^{-1}
49353	NGC5338	14.59	13.31	12.73	12.41	12.36	12.98	13.50	13.13	(...)	16.72	17.81	9.03	7.50	3.2×10^{-1}
49513	NGC5360	15.14	13.87	13.27	12.94	12.78	13.44	14.07	13.55	(...)	16.99	17.61	9.24	7.52	1.1×10^{-1}
49547	NGC5363	11.81	10.27	9.55	9.12	8.91	9.34	10.00	10.58	(...)	15.12	16.55	10.88	8.01	5.0×10^0
50194	UGC08995	14.88	13.86	13.47	13.32	13.13	14.03	14.64	(...)	(...)	15.77	16.09	9.19	9.11	3.0×10^{-1}
50597	PGC050597	16.20	15.36	15.06	14.88	14.67	15.58	16.20	(...)	(...)	16.90	17.10	9.18	9.37	2.0×10^{-1}
50599	PGC050599	15.45	14.49	14.05	13.84	13.72	14.38	14.95	13.69	(...)	16.32	16.63	9.46	8.99	4.2×10^{-1}
51233	NGC5566	12.18	10.88	10.15	9.76	9.54	9.88	10.54	10.32	(...)	15.02	15.80	11.03	9.16	2.3×10^0
51241	NGC5569	14.63	13.59	13.17	12.93	12.80	13.62	14.27	(...)	(...)	15.58	15.87	9.39	9.07	3.9×10^{-1}

Table A.2 – continued

PGC (1)	Name (2)	u' (3)	g' (4)	r' (5)	i' (6)	z' (7)	W1 (8)	W2 (9)	W3 (10)	W4 (11)	FUV (12)	NUV (13)	M_* (14)	M_{HI} (15)	SFR _{FUV} (16)
51332	NGC5587	14.57	13.19	12.49	12.10	11.87	12.24	12.88	12.67	(...)	16.22	16.65	10.54	9.51	6.4×10^{-1}
51351	UGC09206	14.93	13.94	13.53	13.31	13.28	13.82	14.36	13.26	(...)	15.85	16.31	9.62	8.90	9.7×10^{-1}
51401	PGC051401	15.52	14.27	13.91	13.74	13.71	14.13	14.68	13.08	11.46	16.30	16.74	9.40	9.06	5.6×10^{-1}
51422	NGC5600	13.22	12.25	11.78	11.54	11.43	11.77	12.25	10.24	9.56	14.16	14.73	10.29	9.35	6.2×10^0
51449	PGC051449	16.23	15.18	14.83	14.65	14.68	15.57	16.16	(...)	(...)	(...)	(...)	8.60	8.86	(...)
51604	PGC051604	16.63	15.72	15.37	15.18	15.14	16.04	16.90	(...)	(...)	17.40	17.88	9.24	8.63	1.3×10^{-1}
51664	UGC09273	15.63	14.72	14.39	14.22	14.18	14.98	15.46	(...)	(...)	16.28	16.55	8.23	7.82	4.3×10^{-2}
51685	IC1014	13.88	12.92	12.54	12.32	12.23	12.86	13.42	12.63	(...)	14.76	15.11	9.67	9.56	8.0×10^{-1}
51846	NGC5645	13.23	12.26	11.85	11.64	11.54	12.17	12.82	11.64	10.95	14.17	14.63	9.70	9.06	9.1×10^{-1}
51912	PGC051912	16.09	15.12	14.77	14.55	14.45	15.35	15.88	(...)	(...)	17.07	17.49	9.41	9.56	6.7×10^{-1}
51921	NGC5661	14.59	13.75	13.33	13.12	13.04	13.39	13.91	12.18	11.52	15.31	15.62	10.01	10.07	2.2×10^0
51953	NGC5665	(...)	12.33	11.83	11.59	11.45	11.74	12.19	10.10	9.22	14.65	15.24	9.57	8.72	1.2×10^0
51984	UGC09356	14.70	13.72	13.33	13.10	12.97	13.60	14.20	12.99	(...)	15.32	15.74	9.74	9.69	1.3×10^0
51995	PGC051995	14.28	13.19	12.64	12.36	12.18	12.55	13.09	11.60	10.98	15.18	15.65	9.91	9.04	1.4×10^0
52016	UGC09364	15.43	14.52	14.12	13.89	13.70	14.43	14.96	(...)	(...)	16.24	16.54	9.50	9.28	3.9×10^{-1}
52018	NGC5668	12.58	11.71	11.36	11.19	11.17	11.73	12.38	10.73	10.21	13.28	13.56	10.21	9.71	3.1×10^0
52092	UGC09380	15.94	15.04	14.64	14.31	14.25	15.47	16.23	(...)	(...)	16.15	16.26	9.09	9.01	1.4×10^{-1}
52141	UGC09385	15.45	14.93	14.64	14.46	14.22	15.91	16.86	(...)	(...)	16.54	16.75	9.23	8.93	9.1×10^{-2}
52212	PGC052212	16.65	15.68	15.28	15.08	14.87	15.88	16.53	(...)	(...)	17.52	17.73	8.85	8.45	6.9×10^{-2}
52365	NGC5701	12.75	11.29	10.64	10.21	9.84	10.50	11.15	11.52	(...)	14.76	15.16	10.68	9.78	7.7×10^{-1}
52689	UGC09500	16.02	14.98	14.68	14.57	14.29	15.48	16.09	(...)	(...)	16.55	16.73	8.87	9.26	1.8×10^{-1}
52819	PGC052819	16.31	15.53	15.31	15.22	15.15	15.95	16.55	(...)	(...)	16.72	16.87	8.58	8.47	1.3×10^{-1}
52887	NGC5762	14.34	13.38	12.92	12.65	12.56	13.16	13.86	12.97	(...)	15.25	15.42	10.00	9.46	5.1×10^{-1}
53512	PGC053512	16.23	15.49	15.18	15.03	14.89	15.81	16.30	(...)	(...)	16.89	17.15	8.79	9.04	1.3×10^{-1}
54084	PGC054084	16.09	15.29	15.02	14.88	14.68	15.72	16.23	(...)	(...)	16.66	16.88	8.41	9.12	1.1×10^{-1}

Table A.2 – continued

PGC (1)	Name (2)	u' (3)	g' (4)	r' (5)	i' (6)	z' (7)	W1 (8)	W2 (9)	W3 (10)	W4 (11)	FUV (12)	NUV (13)	M_{\star} (14)	M_{HI} (15)	SFR _{FUV} (16)
54849	NGC5921	12.26	11.04	10.47	10.13	9.95	10.53	11.04	9.76	9.38	13.41	13.72	10.03	9.17	1.1×10^0
55308	PGC055308	16.42	15.38	15.11	14.98	14.78	15.58	15.99	(...)	(...)	(...)	(...)	8.39	8.81	(...)
55482	NGC5954	14.04	13.03	12.51	12.27	12.11	12.31	12.76	(...)	9.62	15.11	15.76	9.70	9.18	1.8×10^0
55501	NGC5956	14.01	12.91	12.35	12.03	11.87	12.31	12.92	11.94	(...)	15.21	15.47	10.18	9.24	6.3×10^{-1}
55520	NGC5957	13.56	12.26	11.71	11.39	11.16	11.74	12.33	11.56	(...)	14.61	14.93	10.36	9.72	1.3×10^0
55637	NGC5964	13.02	11.89	11.46	11.19	10.70	11.65	12.24	11.17	(...)	13.90	14.31	10.35	9.81	3.4×10^0
55660	PGC055660	15.64	14.80	14.37	14.15	14.25	15.31	15.62	(...)	(...)	(...)	(...)	8.21	9.37	(...)
55665	NGC5970	12.96	11.75	11.21	10.91	10.73	11.15	11.71	10.25	9.91	(...)	(...)	10.45	9.60	(...)
55710	UGC09951	15.79	15.09	14.76	14.58	14.40	15.51	16.13	(...)	(...)	16.71	16.96	9.03	9.08	2.1×10^{-1}
55965	UGC10009	17.11	16.06	15.57	15.26	15.11	15.86	15.89	(...)	(...)	18.28	17.95	7.42	8.70	1.1×10^{-2}
55967	IC4582	15.36	14.24	13.64	13.29	12.99	12.95	13.47	11.76	11.45	16.68	16.94	9.86	9.38	3.4×10^{-1}
55975	UGC10014	16.06	15.18	14.80	14.54	14.72	15.44	15.95	(...)	(...)	(...)	(...)	8.90	9.90	(...)
55989	UGC10023	15.69	14.88	14.55	14.36	14.37	15.30	15.84	(...)	(...)	16.36	16.61	8.77	9.15	2.7×10^{-1}
56110	PGC056110	16.18	15.12	14.69	14.37	14.43	15.04	15.62	(...)	(...)	17.00	17.32	9.82	9.78	8.3×10^{-1}
56111	UGC10041	14.32	13.34	12.97	12.71	12.76	13.48	13.96	(...)	(...)	(...)	(...)	9.32	9.82	(...)
56142	PGC056142	16.56	15.80	15.37	15.18	14.99	15.86	16.50	(...)	(...)	17.57	18.03	8.97	8.41	1.9×10^{-1}
56168	UGC10058	16.36	15.61	15.39	15.24	15.12	16.05	16.45	(...)	(...)	16.74	16.82	8.31	9.35	2.0×10^{-1}
56334	NGC6012	13.32	12.17	11.64	11.34	11.15	11.62	12.23	11.01	(...)	14.55	15.10	10.52	9.78	2.9×10^0
57120	PGC057120	16.28	15.51	15.19	15.04	14.88	15.99	16.53	(...)	(...)	17.03	17.30	8.34	8.98	8.3×10^{-2}
57169	PGC057169	15.70	14.73	14.37	14.17	14.04	14.81	15.40	(...)	(...)	16.34	16.67	9.24	8.70	2.8×10^{-1}
57205	NGC6063	14.57	13.41	12.90	12.61	12.45	12.93	13.52	12.28	(...)	15.67	16.11	10.12	9.51	1.5×10^0
57799	NGC6106	13.34	12.34	11.89	11.66	11.51	12.01	12.53	11.08	10.70	14.47	14.79	9.95	9.59	1.3×10^0
67421	UGC11820	15.04	14.14	14.01	13.81	14.10	15.76	16.20	(...)	(...)	16.36	16.41	7.98	9.37	5.4×10^{-2}
67759	UGC11866	15.42	14.55	14.28	14.12	13.96	14.90	15.23	(...)	(...)	15.91	16.17	8.91	9.56	3.0×10^{-1}
68046	PGC068046	15.56	14.63	14.27	14.06	14.00	14.91	15.48	(...)	(...)	(...)	(...)	9.03	9.14	(...)

Table A.2 – continued

PGC (1)	Name (2)	u' (3)	g' (4)	r' (5)	i' (6)	z' (7)	W1 (8)	W2 (9)	W3 (10)	W4 (11)	FUV (12)	NUV (13)	M_{\star} (14)	M_{HI} (15)	SFR _{FUV} (16)
68096	NGC7217	11.80	10.17	9.43	9.00	8.73	9.15	9.80	9.43	9.37	13.64	14.38	11.05	8.86	3.0×10^0
68163	UGC11921	15.02	14.01	13.65	13.46	13.45	14.15	15.01	(...)	(...)	(...)	(...)	10.01	9.23	(...)
68870	NGC7280	14.09	12.47	11.74	11.35	11.15	11.61	12.32	13.12	(...)	17.38	19.67	10.49	8.19	1.4×10^1
68878	PGC068878	15.66	14.79	14.39	14.11	14.11	14.59	15.17	(...)	(...)	16.73	17.15	8.98	8.73	2.0×10^{-1}
68922	NGC7286	14.46	13.40	12.95	12.73	12.60	13.38	14.04	13.63	(...)	15.45	15.86	9.01	8.72	1.8×10^{-1}
68941	NGC7292	13.34	12.50	12.18	12.02	11.89	12.64	13.21	12.23	11.35	13.98	14.28	9.18	8.96	5.1×10^{-1}
69212	UGC12090	15.68	14.83	14.55	14.43	14.32	15.35	16.00	(...)	(...)	16.37	16.67	9.07	8.98	2.5×10^{-1}
69844	UGC12212	15.24	14.44	14.17	13.99	14.02	15.13	15.39	(...)	(...)	15.92	16.26	7.97	9.34	3.5×10^{-1}
70131	NGC7437	14.11	13.09	12.64	12.39	12.22	12.94	13.51	12.57	(...)	(...)	(...)	9.63	9.06	(...)
70213	NGC7448	12.68	11.70	11.31	11.11	10.96	11.35	11.78	(...)	9.21	(...)	(...)	10.09	9.78	(...)
70275	UGC12311	15.48	14.44	14.01	13.79	13.63	14.59	15.25	(...)	(...)	16.66	17.26	8.95	8.43	1.1×10^{-1}
70291	NGC7463	13.84	12.66	12.33	12.13	11.97	12.62	13.16	11.41	10.64	(...)	(...)	9.56	9.22	(...)
70295	PGC070295	13.62	12.53	12.00	11.72	11.36	11.88	12.29	10.77	10.00	(...)	(...)	9.75	9.60	(...)
70404	UGC12340	16.16	15.24	14.96	14.73	14.47	15.53	16.07	(...)	(...)	16.71	16.96	8.23	8.77	5.2×10^{-2}
70633	IC1473	14.58	13.40	12.84	12.54	12.42	13.07	13.73	12.60	(...)	15.87	16.36	9.29	8.13	1.4×10^{-1}
71538	UGC12613	12.88	11.91	11.42	11.09	11.04	12.15	13.00	(...)	(...)	14.77	15.82	8.04	6.86	1.6×10^{-2}
71973	UGC12713	15.38	14.36	13.96	13.76	13.65	14.61	15.25	(...)	(...)	16.25	16.48	8.47	8.59	4.3×10^{-2}
72087	UGC12732	14.02	13.01	12.70	12.50	12.28	13.21	13.20	(...)	(...)	14.59	14.84	7.65	9.60	3.7×10^{-1}
73177	NGC7800	13.44	12.69	12.38	12.20	12.13	12.87	13.30	12.30	(...)	14.39	14.70	9.56	9.78	1.2×10^0
84268	PGC084268	16.68	15.91	15.60	15.48	15.24	16.16	16.51	(...)	(...)	17.46	17.64	8.64	8.34	6.6×10^{-2}
85276	PGC085276	16.01	15.11	14.69	14.51	14.37	15.33	15.97	(...)	(...)	16.90	17.31	8.90	8.26	2.1×10^{-1}
86806	PGC086806	(...)	(...)	(...)	(...)	(...)	15.36	15.96	(...)	(...)	(...)	(...)	7.89	7.65	(...)
87128	PGC087128	16.84	15.56	15.16	14.85	14.84	15.71	16.02	(...)	(...)	(...)	(...)	7.49	8.03	(...)
87175	PGC087175	16.48	15.78	15.51	15.39	15.20	16.41	16.63	(...)	(...)	17.32	17.44	7.57	9.09	6.8×10^{-2}
138451	PGC138451	16.97	15.99	15.62	15.42	15.35	16.25	16.74	(...)	(...)	17.99	18.31	7.05	7.21	4.2×10^{-3}

Table A.2 – continued

PGC	Name	u'	g'	r'	i'	z'	W1	W2	W3	W4	FUV	NUV	M_{\star}	M_{HI}	SFR _{FUV}
(1)	(2)	(3)	(4)	(5)	(6)	(7)	(8)	(9)	(10)	(11)	(12)	(13)	(14)	(15)	(16)
1263558	PGC1263558	16.51	15.73	15.30	15.11	14.97	15.86	16.65	(...)	(...)	17.18	17.42	9.14	8.23	8.1×10^{-2}
1267592	PGC1267592	16.70	15.78	15.43	15.23	15.36	16.41	17.17	(...)	(...)	17.38	17.69	9.21	9.27	1.9×10^{-1}
1331483	PGC1331483	16.66	15.84	15.51	15.41	15.40	16.20	16.57	(...)	(...)	17.32	17.63	8.70	8.81	1.3×10^{-1}
1346685	PGC1346685	16.53	15.40	14.94	14.73	14.64	15.57	16.15	(...)	(...)	18.24	19.18	8.60	7.56	7.9×10^{-2}
1360237	PGC1360237	16.63	15.89	15.60	15.44	15.36	16.26	16.98	(...)	(...)	17.29	(...)	8.89	8.67	(...)
1371096	PGC1371096	16.90	15.82	15.44	15.27	15.09	16.21	17.05	(...)	(...)	(...)	(...)	8.92	7.81	(...)
1424345	PGC1424345	18.86	17.73	16.73	16.25	15.79	16.01	16.25	(...)	(...)	22.48	22.64	7.26	7.71	9.0e-05
1448560	PGC1448560	17.21	16.16	15.75	15.55	15.36	16.20	16.55	(...)	(...)	17.98	18.15	7.11	7.72	5.6×10^{-3}
1462017	PGC1462017	(...)	(...)	(...)	(...)	(...)	15.22	15.96	(...)	(...)	16.98	16.97	8.57	7.78	1.3×10^{-2}
1468320	PGC1468320	16.52	15.46	15.01	14.78	14.71	15.71	16.36	(...)	(...)	17.55	17.91	8.91	8.29	9.4×10^{-2}
1505120	PGC1505120	17.41	(...)	16.05	15.94	15.48	16.27	17.09	(...)	(...)	(...)	(...)	8.66	8.94	(...)
1697033	PGC1697033	16.10	15.29	14.95	14.75	14.68	15.59	16.20	(...)	(...)	16.85	17.23	8.61	7.82	1.1×10^{-1}
1726175	PGC1726175	17.36	16.04	15.59	15.36	15.33	16.48	17.11	(...)	(...)	(...)	(...)	7.32	6.64	(...)
1742964	PGC1742964	16.08	15.26	14.91	14.75	14.64	15.50	15.81	(...)	(...)	16.80	(...)	9.07	8.41	(...)
1800124	PGC1800124	16.91	15.71	15.24	15.02	15.02	15.94	16.64	(...)	(...)	17.92	18.17	8.16	7.42	1.1×10^{-2}
2801023	PGC2801023	16.79	15.77	15.40	15.22	15.14	16.20	16.79	(...)	(...)	17.66	18.05	8.56	8.79	9.4×10^{-2}
3466489	PGC3466489	16.84	15.94	15.57	15.35	15.32	16.22	16.33	(...)	(...)	17.81	18.22	6.24	7.26	6.4×10^{-3}
3723606	PGC3723606	15.29	14.27	13.92	13.85	13.75	15.08	15.64	(...)	(...)	17.31	18.45	9.16	8.92	1.3×10^0
3850707	PGC3850707	16.94	15.91	15.44	15.20	15.20	15.85	16.34	(...)	(...)	(...)	(...)	8.63	8.69	(...)
4004996	PGC4004996	15.06	15.16	15.48	15.29	15.21	16.41	17.20	(...)	(...)	17.82	18.12	8.97	8.49	6.2×10^{-2}
4112990	PGC4112990	16.88	16.14	15.79	15.68	15.57	16.32	16.59	(...)	(...)	(...)	(...)	7.50	8.63	(...)
4668301	PGC4668301	17.60	16.27	15.84	15.60	15.55	16.49	17.13	(...)	(...)	18.69	19.29	8.63	8.21	7.1×10^{-2}
5057570	PGC5057570	(...)	(...)	(...)	(...)	(...)	15.91	16.60	(...)	(...)	16.79	18.56	9.13	8.48	9.5×10^0
5057575	PGC5057575	16.46	15.89	15.62	15.48	15.58	16.23	17.42	(...)	(...)	17.05	17.18	9.80	8.44	5.9×10^{-2}
5058796	PGC5058796	16.57	15.79	15.53	15.35	15.40	16.39	16.81	(...)	(...)	17.10	17.17	7.75	8.59	3.4×10^{-2}

Table A.2 – continued

PGC (1)	Name (2)	u' (3)	g' (4)	r' (5)	i' (6)	z' (7)	W1 (8)	W2 (9)	W3 (10)	W4 (11)	FUV (12)	NUV (13)	M_{\star} (14)	M_{HI} (15)	SFR _{FUV} (16)
5058884	PGC5058884	(...)	(...)	(...)	(...)	(...)	15.56	16.22	(...)	(...)	19.00	19.45	8.83	8.20	1.6×10^{-2}
5058897	PGC5058897	(...)	(...)	(...)	(...)	(...)	16.25	16.79	(...)	(...)	(...)	(...)	8.13	7.67	(...)
5059667	PGC5059667	17.29	16.26	15.75	15.49	15.20	16.35	17.39	(...)	(...)	19.13	20.50	9.51	7.88	2.2×10^{-1}
5060003	PGC5060003	16.87	15.82	15.29	14.99	14.87	15.98	16.75	(...)	(...)	18.30	18.85	8.70	7.80	3.0×10^{-2}

NOTE: Column (3)–(13) are magnitudes in AB magnitudes. Column (14) and (15) are stellar and H I mass in $\log(M/M_{\odot})$.

Column (16) is the SFR derived from FUV flux, in unit of $\log(M/M_{\odot}) \text{ yr}^{-1}$